IS-T-721

ELECTROMODULATION SPECTROSCOPY OF sc AND fcc PHASE TlCl AND TlBr

John Frederick McClelland

Ph.D. Thesis Submitted to Iowa State University

Ames Laboratory, ERDA
Iowa State University
Ames, Iowa 50011

Date Transmitted: June 1976

PREPARED FOR THE U.S. ENERGY RESEARCH AND DEVELOPMENT ADMINISTRATION UNDER CONTRACT NO. W-7405-eng-82

MASTER

DISTRIBUTION OF THIS DOCUMENT IS UNLIMITED

Available from: National Technical Information Service
U. S. Department of Commerce
P.O. Box 1553
Springfield, VA 22161

Price: Microfiche $2.25

Electromodulation spectroscopy of sc and fcc phase TlCl and TlBr

by

John Frederick McClelland

An Abstract of
A Dissertation Submitted to the
Graduate Faculty in Partial Fulfillment of
The Requirements for the Degree of
DOCTOR OF PHILOSOPHY

Approved:

David W. Lynch
In Charge of Major Work

For the Major Department

For the Graduate College

Iowa State University
Ames, Iowa
1976

TABLE OF CONTENTS

Electromodulation spectroscopy of sc and fcc phase TlCl and TlBr*

John Frederick McClelland

Under the supervision of David W. Lynch
From the Department of Physics
Iowa State University

Electromodulation measurements have been made on normal (sc) phase, CsCl structure, TlCl and TlBr and the spectra have been reduced to the electric field induced changes in the dielectric function which are shown to be in reasonably good agreement with the calculations of Blossey. A sample preparation technique was developed which, allowed the measurements to be made near liquid helium temperature with a low level of static strain in the sample and with no observed dynamic strain due to the electric field modulation. Photoconductivity effects were controlled to the extent that the electromodulation spectrum could be measured over the exciton and interband region with substantially lower distortion than has been reported in electroreflectance measurements where structure is nearly absent for the n=1 exciton state. Electromodulation features were observed which are tentatively assigned to intrinsic exciton state splitting and to an exciton-phonon bound state.

Absorption and EA measurements were made on abnormal (fcc) phase, NaCl structure, TlCl and TlBr which located the n=2 TlBr exciton state

---

*USERDA Report IS-T-721. This work was performed under Contract W-7405-eng-82 with the Energy Research and Development Administration.

energy and showed unusual EA lineshapes for two features in each compound that have no established assignment. Sample preparation sensitivity was observed for these features in the absorption spectra. The TlBr exciton binding energy, band gap, and static dielectric constant were obtained from the EA measurement.

CHAPTER I. INTRODUCTION

Background

Studies of processes involving the interaction of light with matter historically have contributed a great deal of stimulus to experimental and theoretical physics. The interaction of light with matter in the early 1900's provided the experimental basis for understanding the quantum nature of light. Approximately 50 years later, activity began on the study of the optical properties of solids, which has led to a considerably more detailed understanding of solids than had been obtained from previous efforts in this field. Much of the experimental work has centered around the measurement of optical spectra of crystals, providing information on electronic transition energies and strengths. Complementary developments in theory have allowed the comparison of spectra with calculated one-electron energy band structures, from which spectra can be calculated, with strengths determined by electric dipole matrix elements. When wavefunctions could be obtained, matrix element calculations have determined actual transition strengths. More often, the allowed or forbidden nature of transitions has been investigated by symmetry arguments.

The Resolution Problem

Difficulties have existed in determining accurate transition energies from experimental spectra for fitting to band structure because of the usual broad and overlapping nature of solid state spectra, due to lifetime, thermal and strain broadening effects, and the close spacing of states. Better resolved spectra, however, can be observed due to both intrinsic and extrinsic origins. For the case of semiconductors and insulators, intrinsically narrow lines are observed for transitions involving bound exciton states[1-5] which are discussed in more detail in the next chapter. For these transitions, an electron is excited by a photon from the valence band to an exciton state below the conduction band. The final state is a bound state arising from the Coulomb potential between the hole in the valence band and the excited electron. The bound states of the coulomb potential are less crowded, resulting in substantially more resolved features.

More highly resolved features can be obtained extrinsically by measuring a modulation spectrum[6,7] which is a differential of the usual spectrum with respect to an external perturbation such as an electric field. The spectra of this study are enhanced by both bound exciton states and electric field modulation. The latter is discussed in Appendix A.

TlBr and TlCl

TlBr and TlCl, the two insulators selected for electromodulation (EM) measurements, were chosen initially with interest in clarifying aspects of both band structures and exciton states. Very early in this project the principal questions were answered by structure assignments to improved band calculations[8,9] and by magneto-optical measurements[10] which resolved the exciton states in remarkable detail. Also during this time, detailed theoretical calculations[11a,b] were published for the electroabsorption (EA) of excitons and this prompted the continuation of the project because of the fundamental interest in excitons which, do not fit into the one electron theory of solids.

Later in the course of the experiment interest developed in an abnormal face centered cubic (fcc) crystal phase of TlBr and TlCl, which normally crystallize in a simple cubic (sc) phase.

Results of the experiments on the sc phase have not allowed a quantitative test of the theory, for reasons discussed later, but useful information has been obtained on various properties including photoconductivity, electroreflectivity, phonon sidebands, and the doublet structure of the exciton. The fcc data have enabled the exciton binding energy, band gap, and static dielectric constant to be calculated for TlBr. An unusual EA structure has been observed in TlBr and TlCl for features previously assigned to splitting of the exciton ground state or to excited exciton states.

CHAPTER II. EXCITON ENERGY STATES

The ground state of an insulator consists of a set of fully occupied electronic energy levels separated by an energy gap from unoccupied higher energy levels. Electronic excitation occurs when absorption of a photon causes an electron in the occupied levels to be transferred to one of the higher levels or when photons, not energetic enough for interband excitations, excite states which are not included in the one electron picture of the crystal. This latter excitation is called an exciton.[1-3] An exciton comprises a problem involving the excited electron, the previously occupied level, which is called a hole, and the polarized crystal. The solution of this problem requires simplifying assumptions and, depending on which are appropriate, excitons are usually described as Frenkel[1] or Wannier[2] like. Frenkel excitons occur when the excitation is localized at or near a particular atom or molecule in materials where atoms do not interact strongly.

Wannier Excitons

Wannier excitons, which are appropriate for describing electronic excitations in the thallium halides, are not localized on atoms or molecules. In the band picture for these materials, when excitons are created by photon absorption, an electron makes a transition from an energy state in the valence band to a bound state with an energy below a conduction band. The electron is bound to the hole left in the valence band by a Coulomb potential. The hole may be thought of as having a positive charge and the bound electron-hole system as analogous to a hydrogen atom immersed in a dielectric medium. These excited final states have hydrogenic radii which extend over a distance of a number of lattice constants. The potential binding the electron and hole ideally has the coulomb form, modified by the static dielectric constant of the crystal. Usually this is only approximately achieved and in materials with more localized excitations the optical dielectric constant becomes more appropriate, due to the higher frequency motion of the electron and hole. In the thallium halides studied, a good fit to hydrogenic energy levels[10] is obtained with the 1/r Coulomb potential, divided by a dielectric constant equal to approximately half the static value or about three times the optical value. In very localized materials a potential with a different radial dependence[12] must be used, resulting in a difficult Hamiltonian to solve.

Electric Field Effects on Exciton States[11a,b]

The theoretical description for this experiment involves the absorption of light due to transitions to both bound and continuum Wannier exciton states and the effect of an electric field on these transitions. The measurements are analogous to the Stark effect for the hydrogen atom but two differences prevent the development of the theory in the framework of perturbation theory used in the case of the Stark effect. Firstly, the electric fields which can be applied to the exciton system can easily exceed the ionization field of the exciton while in the Stark effect the field is a fraction of the ionization field. Secondly, the exciton spectra for zero field are substantially broadened by thermal and other mechanisms causing electric field effects to be very small. In order to detect experimentally the small electric field-induced changes, a difference spectrum is measured, which consists of the change in the transmission due to the electric field. Hence the theory calculates both a zero and nonzero applied electric field spectrum for ε_2, the imaginary part of the dielectric function, which is proportional to the absorption coefficient, α. Since small differences in rather large quantities are being determined considerable demands are placed on both experiment and theory if results are to be compared quantitatively.

The beginning point for the theory is the one-electron energy band picture[13] of the crystal with a direct band gap at $\vec{k} = 0$, nondegenerate bands and isotropic effective electron and hole band masses. An excitonic theory[11a,b] will be outlined in contrast to the early one electron theory of Franz[14] and Keldysh[15] and early electromodulation calculations made in the weak binding limit.[16,17] The theory is oversimplified for the thallium halides due to photoconductivity, band degeneracy, phonon coupling and anisotropy but, nevertheless, is useful.

As discussed earlier, the one electron ground state consists of a full valence band and empty conduction band. A photo-excited state breaks the periodic lattice translational symmetry due to the coulomb interaction between the electron and hole and hence must be approximated as a linear combination of the one electron band electron and hole Bloch functions given by[18]

$$\Psi_{n,\vec{k}}(\vec{r}_e,\vec{r}_h) = \sum_{\substack{c,\vec{k}_e \\ v,\vec{k}_h}} A^{c,v}_{n,\vec{k}}(\vec{k}_e,\vec{k}_h)\ \Psi_{c,\vec{k}_e}(\vec{r}_e)\ \Psi_{v,\vec{k}_h}(\vec{r}_h)\ , \qquad (1)$$

where n and $\vec{k}(= \vec{k}_e + \vec{k}_h)$ denote the exciton state and $\Psi_{c,\vec{k}_e}$ and $\Psi_{v,\vec{k}_h}$

are Bloch functions of the electron and valence bands, respectively. The coordinate vectors, $\vec{r}$, and wave vectors, $\vec{k}$, are subscripted to designate association with electrons (e) or holes (h).

Neglecting a small exchange term[18] the energy difference, E, between the excited and ground states can be determined from the following set of equations.[18]

$$[E_c(\vec{k}_e) - E_v(\vec{k}_h) - E]\, A^{cv}_{n\vec{k}}(\vec{k}_e,\vec{k}_h)$$

$$+ \sum_{\substack{c',\vec{k}'_e \\ v',\vec{k}'_h}} < c\vec{k}_e;\ v\vec{k}_h | V(\vec{r}_e - \vec{r}_h) | c'\vec{k}'_e;\ v\vec{k}'_h > A^{c',v'}_{n,\vec{k}}(\vec{k}'_e,\vec{k}'_h) = 0 \ , \tag{2}$$

where $E_c(\vec{k}_e)$ and $E_v(\vec{k}_h)$ are the conduction and valence band energies and the potential is given by[11a,b]

$$V(\vec{r}_e - \vec{r}_h) = -e^2/\varepsilon_o r - e\vec{\mathcal{E}}\cdot\vec{r} \ ,$$

where ε_o is the static dielectric constant of the crystal, $\vec{r} = \vec{r}_e - \vec{r}_h$, and $\vec{\mathcal{E}}$ is the applied electric field.

If $V(\vec{r})$ varies slowly on the scale of a unit cell, the effective mass equation[19] can be derived from Eq. (2) to be[18]

$$[E_c(-i\nabla_e) - E_v(-i\nabla_h) + V(\vec{r}) - E]\, \Phi^{c,v}_{n,\vec{k}}(\vec{r}_e,\vec{r}_h) = 0 \ , \tag{3}$$

where

$$\Phi^{c,v}_{n,\vec{k}}(\vec{r}_e,\vec{r}_h) = \sum_{\vec{k}_c,\vec{k}_n} e^{i\vec{k}_e\cdot\vec{r}_e + i\vec{k}_h\cdot\vec{r}_h}\, A^{c,v}_{n,\vec{k}}(\vec{k}_e,\vec{k}_h) \ , \tag{4}$$

which is the Fourier transform of $A^{c,v}_{n,\vec{k}}(\vec{k}_e,\vec{k}_h)$. Assuming that the conduction and valence band energies near $\vec{k} = 0$ can be written as $E_c = E_g + (\hbar^2k^2/2m_e^*)$ and $E_v = -\hbar^2k^2/2m_h^*$, Eq. (4) becomes[18]

$$[-\frac{\hbar^2}{2m_e^*}\nabla_e^2 - \frac{\hbar^2}{2m_h^*}\nabla_h^2 + V(\vec{r})]\ \Phi_{n,\vec{k}}(\vec{r}_e,\vec{r}_h) = E_n\ \Phi_{n,\vec{k}}(\vec{r}_e,\vec{r}_h)\ , \qquad (5)$$

where E_g, m_e^*, and m_h^* are the band gap and electron and hole band masses, respectively, and

$$E_n = E - E_g\ . \qquad (6)$$

After a center of mass transformation followed by substitution of the wavefunction,

$$\Phi^{c,v}_{n,\vec{k}} = e^{i\vec{k}\cdot\vec{R}}\ \phi_n(\vec{r}) \qquad (7)$$

in Eq. (5), the hydrogenic exciton Hamiltonian emerges as[18]

$$[-\frac{\hbar^2}{2\mu}\nabla_r^2 - V(\vec{r})]\ \phi_n(\vec{r}) = \varepsilon_n\ \phi_n(\vec{r})\ , \qquad (8)$$

where

$$\varepsilon_n = E_n - \frac{\hbar^2k^2}{2M} \qquad (8)$$

and the center of mass transformation is defined by $M = m_e^* + m_h^*$, $\mu = m_e^*m_h^*/(m_e^* + m_h^*)$, $\vec{r} = \vec{r}_e - \vec{r}_h$, and $\vec{R} = (m_e^*\vec{r}_e + m_h^*\vec{r}_h)/M$.

For $\vec{\mathcal{E}} = 0$, the bound state energies for Eq. (8) are given by

$$\varepsilon_n = -R/n^2, \qquad n = 1,2,\cdots \qquad (10)$$

as in the hydrogen atom with the exciton binding energy or effective

Rydberg given by

$$R = \frac{\mu e^4}{2\hbar^2 \varepsilon_o^2} = \frac{\mu}{m\varepsilon_o^2} \cdot 13.6 \text{ eV} , \tag{11}$$

where e and m are the electronic charge and mass. The exciton Bohr radius is expressed as

$$a_o = \frac{\hbar^2 \varepsilon_o}{\mu e^2} = \frac{m\varepsilon_o}{\mu} \cdot 5.29 \times 10^{-9} \text{ cm} , \tag{12}$$

and the ionization field, $\mathcal{E}_I$, is defined as[11a,b]

$$\mathcal{E}_I = R/ea_o \ . \tag{13}$$

Light absorption by excitons can be calculated by time-dependent perturbation theory.[20] The imaginary part of the dielectric function, ε_2, which is proportional to the absorption coefficient, can be written for allowed transitions as[11a,b]

$$\varepsilon_2(h\nu) = 4/3 \ \varepsilon_o |\vec{\mu}_{cv}/ea_o|^2 \ \phi^2(0) , \tag{14}$$

where $h\nu$ is the photon energy and $\vec{\mu}_{cv}$ is the interband dipole moment given by[11a,b]

$$\vec{\mu}_{cv} = \frac{e}{im\nu} \int_{\substack{\text{unit}\\ \text{cell}}} d\vec{r} \ v^*_{c,\vec{k}} \ \nabla v_{v,\vec{k}} , \tag{15}$$

and $\phi^2(0)$ is expressed as[11a,b]

$$\phi^2(0) = 4\pi^2 \ a_o^3 \ \sum_n |\phi_n(0)|^2 \delta\left[\frac{(E_g + e_n - h\nu)}{R} \right] . \tag{16}$$

Equation (12) is for unpolarized light subject to the condition that the periodic part of the Bloch functions, $v(\vec{r},\vec{k})$ varies slowly with $\vec{k}$. It can be seen from Eq. (14) that the absorption is proportional to the ratio squared of the interband to exciton dipole moments, multiplied by the term $\phi^2(0)$, which contains the sharp bound state and continuum exciton spectra. When an electric field is applied to the crystal, the shifting, splitting, and broadening of bound states is reflected in $\phi^2(0)$, as well as field-induced oscillations of ε_2 in the exciton continuum region.

Since the transitions are direct, $\vec{k} = \vec{k}_e + \vec{k}_h = 0$, and Eq. (7) becomes

$$[- \frac{\hbar^2}{2\mu} \nabla_r^2 - \frac{e^2}{\varepsilon_o r} - e\mathcal{E} z] \phi_n(\vec{r}) = E_n \phi_n(\vec{r}) . \tag{17}$$

Equation (17) was solved by Elliott[20] for $\mathcal{E} = 0$ and Blossey[11a,b] obtained solutions when $\mathcal{E} \neq 0$ through the use of parabolic coordinates and numerical integration of the resulting differential equations. Blossey calculated the shift of the exciton ground state as a function of electric field and his result is shown in Figure 1. The plot shows that the perturbation calculation begins to break down at $\mathcal{E}/\mathcal{E}_I = 0.4$, which would correspond to a field difficult to reach in the case of the hydrogen atom but easily obtained for excitons. He also calculated the electromodulated imaginary part of the dielectric function, $\Delta\varepsilon_2$, for an M_o critical point[21,22] and, using the Kramers-Kronig relationships,[23] obtained the real component $\Delta\varepsilon_1$ for a range of electric field and broadening parameters. His results for $\Delta\varepsilon_2$ appear in Figure 2. The

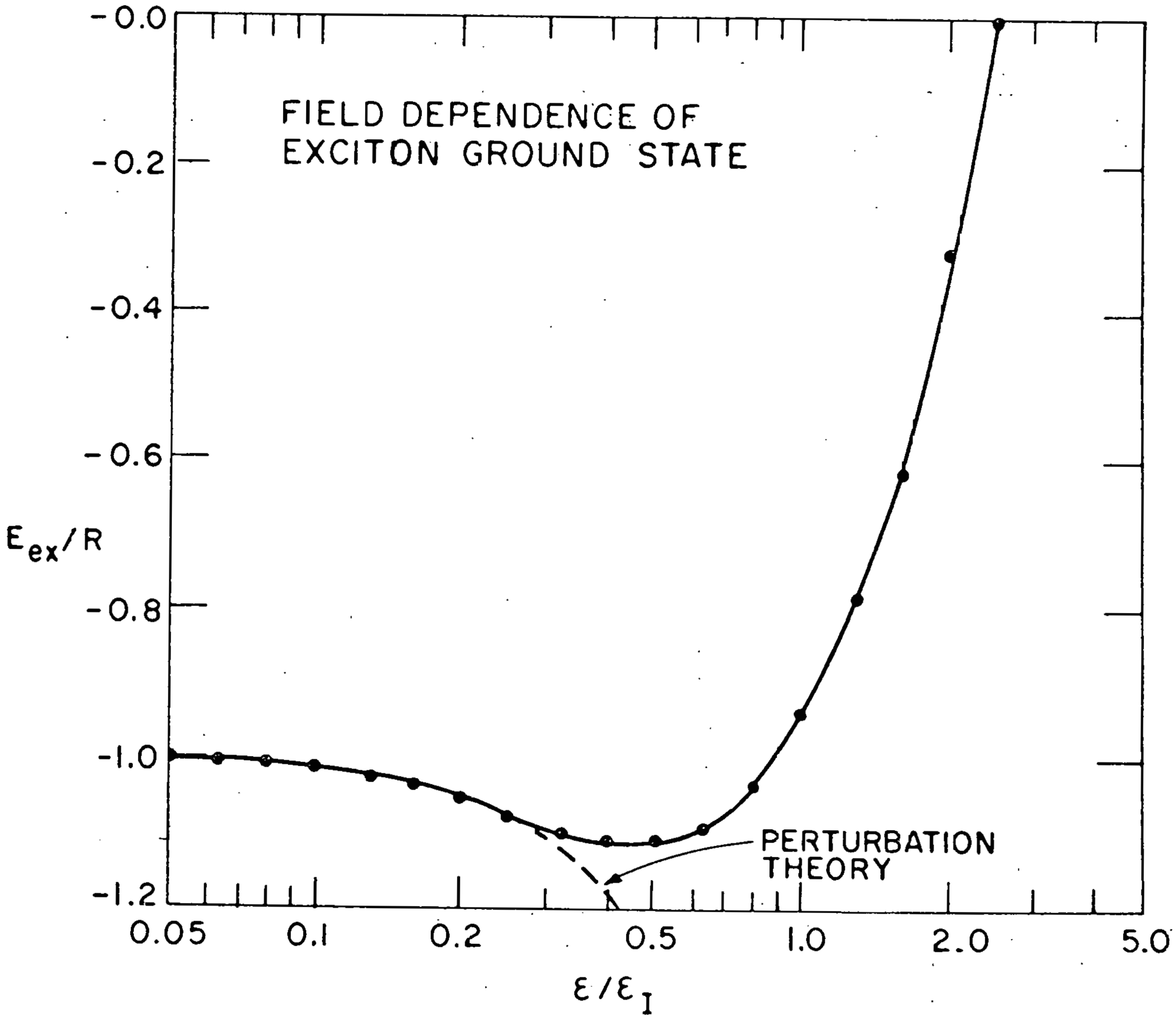

Figure 1. Field dependence of the exciton ground state predicted by perturbation and nonperturbation calculations

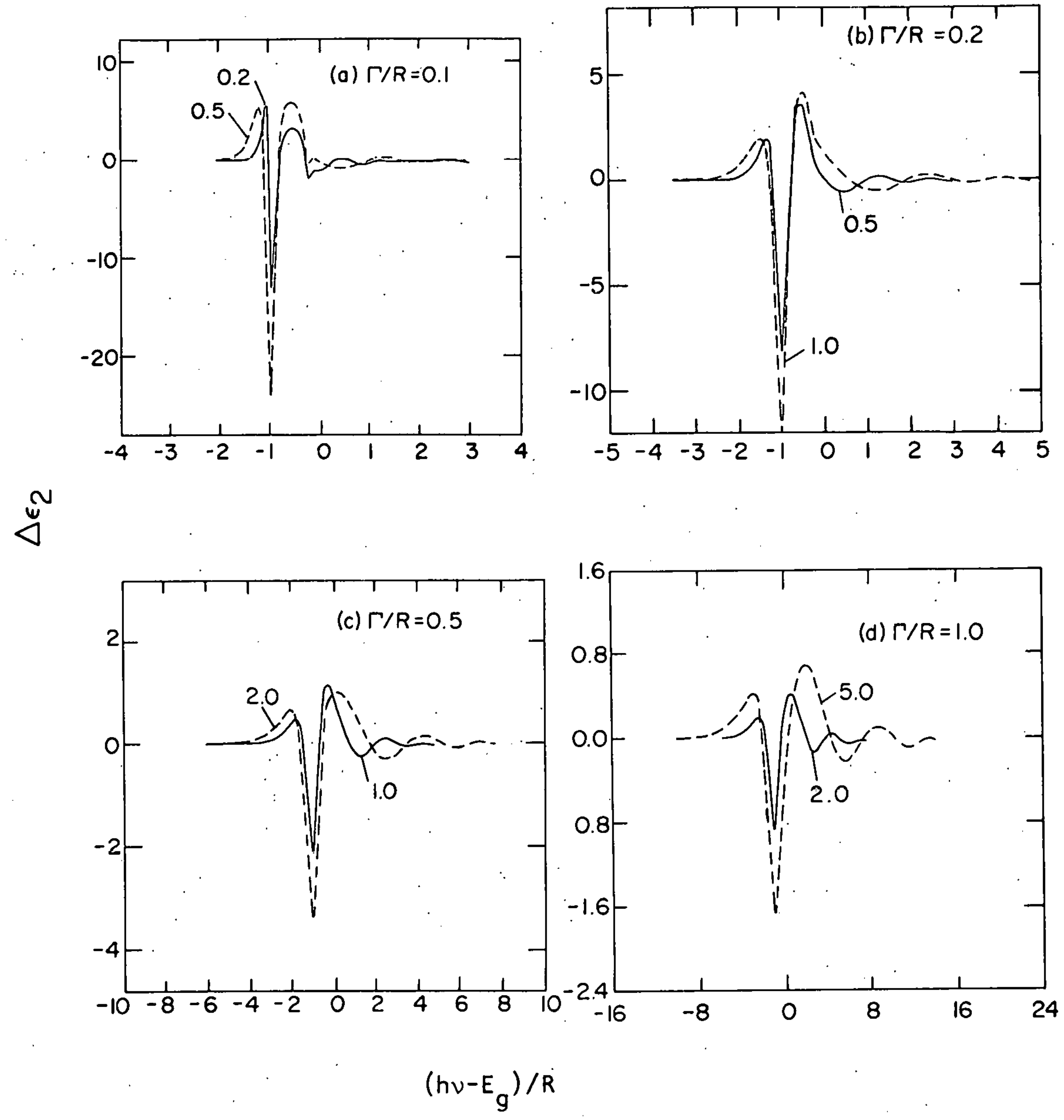

Figure 2. Electric field induced changes in the imaginary part of the dielectric function versus $(h\nu-Eg)/R$ for broadening parameter values from 0.1 to 1.0 R and applied field values from 0.2 to 5.0 $\mathcal{E}_I$

values of the electric modulation field, $\mathcal{E}$, and broadening parameter, $\Gamma \cong kT$, used in the calculations are given for the spectra in Figure 2 as fractions of $\mathcal{E}_I$ and R, respectively, with $\mathcal{E}$ ranging from 0.2 - 5.0 $\mathcal{E}_I$ and Γ from 0.1 to 1.0 R. The large negative peak at $h\nu/R = -1$ is due to the field broadening and shifting of the $n = 1$ state. Structure can be seen for the $n = 2$ state for $\Gamma/R = 0.1$ (a negative peak) and $\Gamma/R = 0.2$ (a negative shoulder), but not for larger broadening. Above $h\nu/R = 0$ the continuum oscillations caused by the electric field are seen.

CHAPTER III. THALLIUM CHLORIDE AND BROMIDE

TlCl and TlBr are insulators, as mentioned earlier, which normally crystallize in a sc phase with a CsCl structure[24] but which may form in amorphous phases[25,26] on low temperature substrates or in a fcc phase NaCl structure,[24,27] usually by epitaxial growth on cleaved alkali halide substrates. The sc phase is an ionic structure with lattice constant[24] values of 2.84 Å (TlCl) and 3.97 Å (TlBr) while the fcc phase has a less dense configuration with lattice constant[24] values of 6.30 Å (TlCl) and 6.56 Å (TlBr).

Relativistic KKR band structure calculations,[8] as well as other band calculations,[9,28-30] indicate that the sc phase band gap is indirect (the valence and conduction band edges are not at the same point of $\vec{k}$-space) with the direct gap at X while for the fcc phase[27,30] the band gap is direct at L. The band structures for the compounds are shown in Figures 3-6 for both phases. The sc band structures are from Ref. 8 and the fcc from Ref. 27. For sc and fcc phases, adjacent to the direct gap, there is a doubly-degenerate mixed s-p valence band and a p type cationic conduction band, which is also doubly degenerate. The sc upper valence band consists of halogen p states with an admixture of thallium 6s states at X. The upper valence band also receives a small (∿10%) contribution from 5d thallium levels 10 eV below the band. The lowest conduction band is made up of thallium p states. Although the sc phase is strongly ionic, the band structures of this phase and the fcc phase appear to be closer to the lead chalogenides than to ionic crystals such as the alkali halides. This has been attributed to the two cationic s valence electrons outside the filled rare gas shell.[8,30]

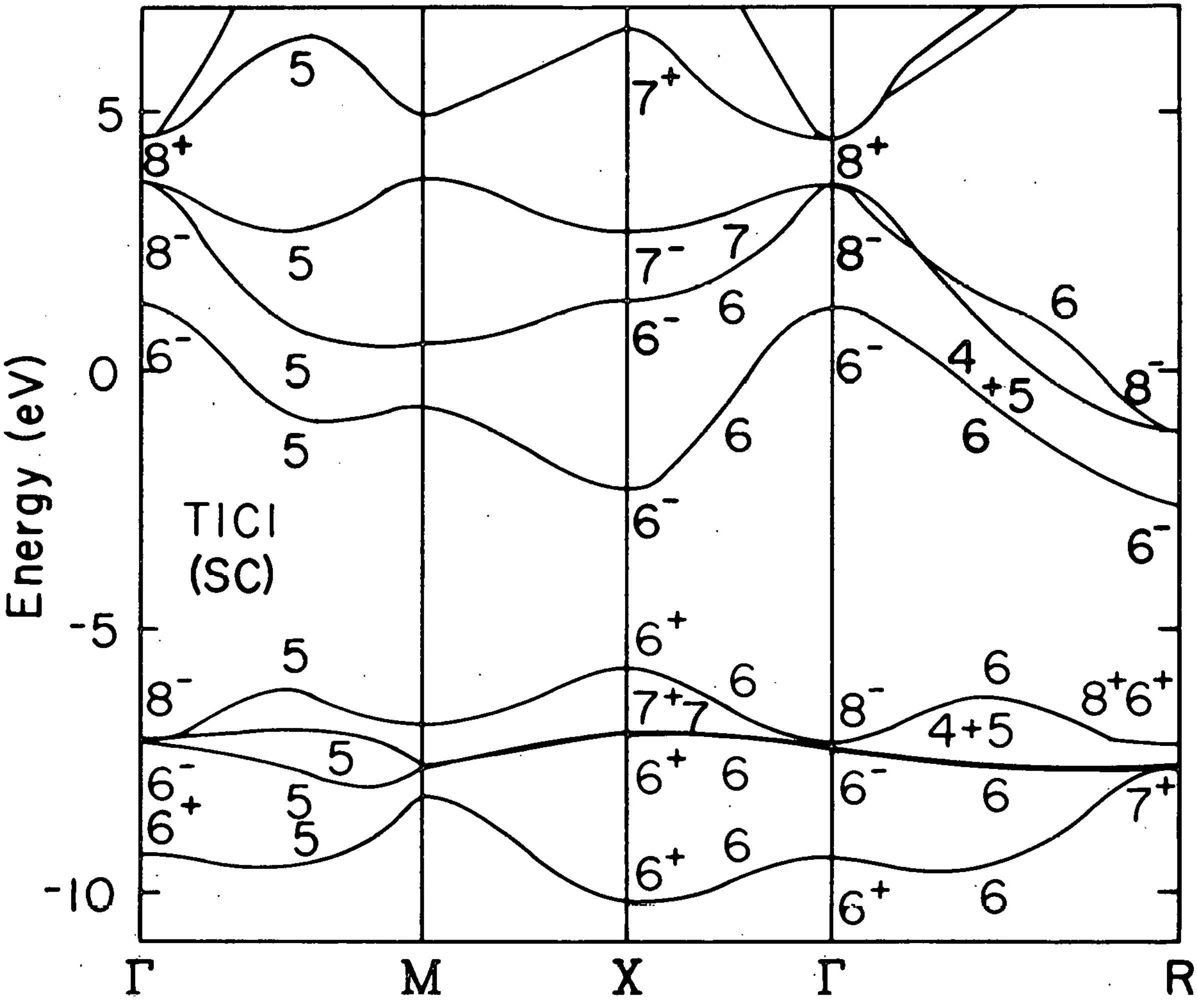

Figure 3. Band structure of sc TlCl

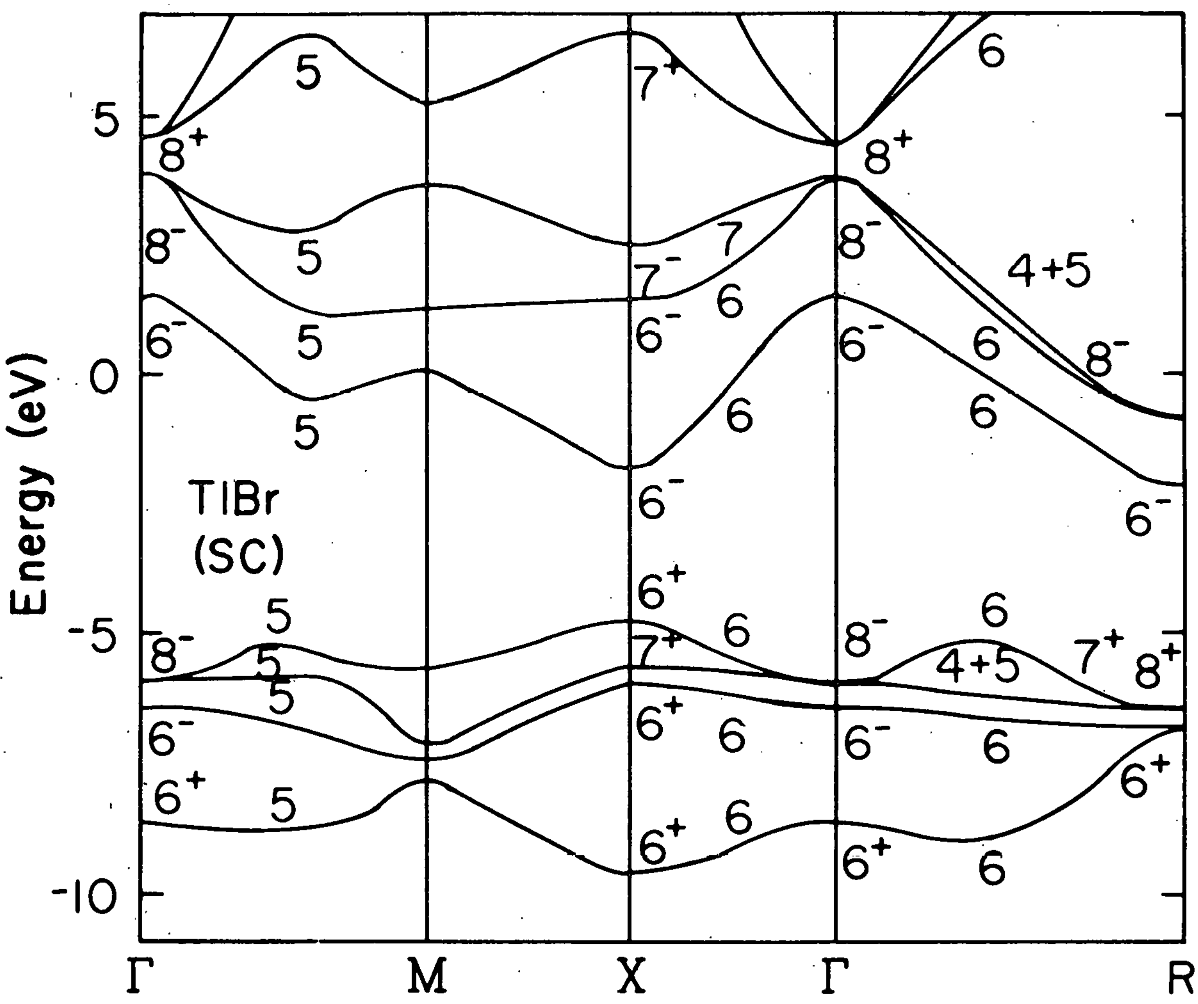

Figure 4. Band structure of sc TlBr

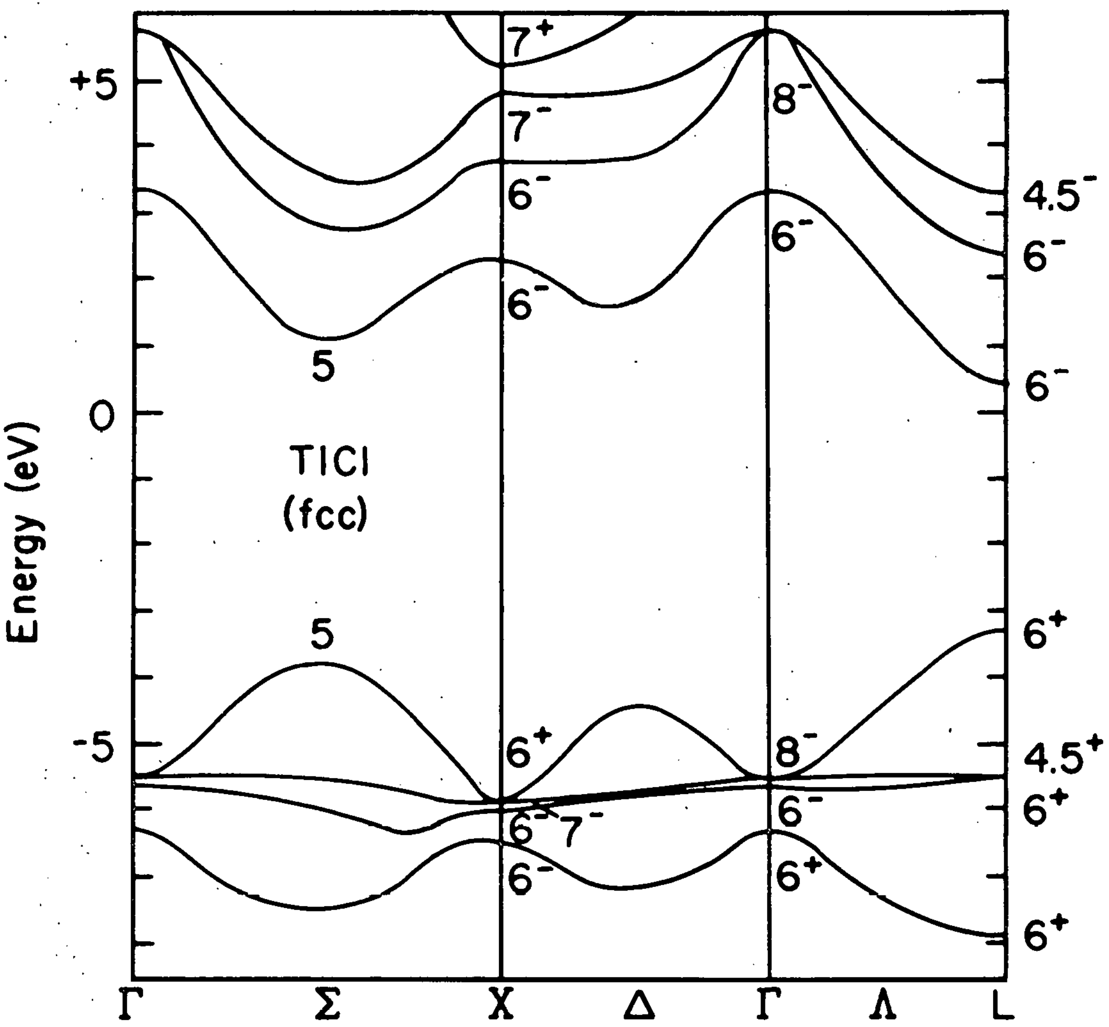

Figure 5. Band structure of fcc TlCl

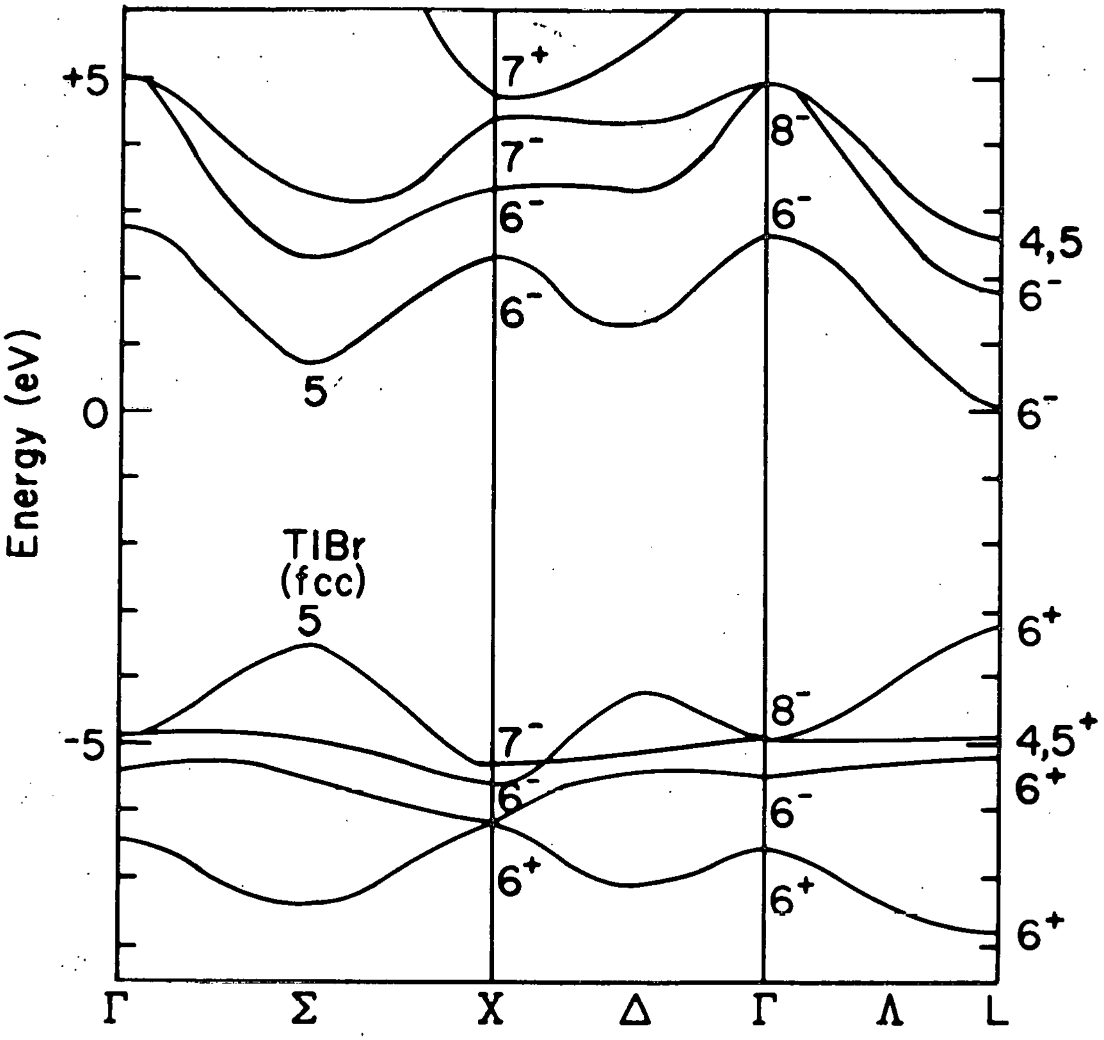

Figure 6. Band structure of fcc TlBr

The band structures in Figures 3-6 are in good agreement with the optical spectra for the thallium compounds. Band assignments for these salts typically fit the experimental transition energies with an accuracy better than 0.3 eV and often considerably better.

Simple Cubic (SC) Phase

A number of studies of the more stable sc phase thallium halides have provided information that has been very useful either directly or for perspective in this investigation. The emphasis of the following is directed in this sense and is not indicative of all areas of research activity concerning the thallium halides.

Early thin film absorption measurements[31,32] on TlCl and TlBr suffered from strain effects due to the mismatch of the sample and substrate thermal expansions when samples were cooled to reduce the thermal broadening of the spectra. In the late 1960's a method of sample preparation was developed[33] which minimizes the low temperature strain problem through a substrate made by supporting a very thin transparent organic membrane on a frame cut from a crystal of the material to be evaporated. When films evaporated on such substrates are cooled, strain is minimized because the thin film and frame have identical expansion coefficients and the film thickness exceeds that of the membrane.

This substrate and film system yields absorption spectra which reveal features[10,33,34] not observed in earlier absorption or reflectivity measurements[35] and their intrinsic nature has been supported by reflectivity[36] measurements on single crystals. The more highly resolved spectra have absorption coefficient magnitudes consistent with the direct transitions predicted by the band structures and sharp exciton and phonon features.

The n = 1 exciton peaks in TlCl and TlBr are split in absorption measurements.[10,33,34] The splitting was initially attributed to strain but later an intrinsic origin was suggested[37] based on the lifting of degenerate exciton states. The exciton wavefunctions are composed of the electron wavefunctions from the bottom of the conduction band and the hole wavefunctions from the top of the valence band. The wavefunction of a given state comes from the bands at the same X point. There are six equivalent X-points in the Brillouin zone, adding to the total exciton degeneracy.

The splitting has been calculated[37,38] using the electron-hole coulomb interaction between excitons in different valleys and the electron-hole exchange interaction within one valley and between valleys. The wavefunctions for the perturbed Hamiltonian were constructed from linear combinations of exciton wavefunctions of three different X points or valleys. Two of the resulting wavefunctions have terms from different valleys while one is constructed from wavefunctions of the same valley. The above explanation is often termed inter- and intravalley scattering of excitons. Recently it has been shown that the splitting can be explained with only the exchange perturbation and wavefunctions constructed from just one valley.[39] The splitting phenomena have been investigated experimentally by static stress-[37] and piezo-[40] reflection, and more recently, by magnetoabsorption[39,41] measurements. At photon energies above the first exciton state absorption, features due to phonon creation (phonon sidebands) and overlapping higher exciton states appear.[10,33,34] The first phonon sideband structure has been explained as due to the creation of an exciton-phonon bound state, while higher energy phonon sidebands are due to the creation of free phonons.[42-44]

Electroabsorption measurements[45] have been made on TlBr using samples with substantial strain and thermal broadening, which prevented the resolution of detailed structure, but allowed the field dependence of the n = 1 state to be observed. Electroreflectance measurements[46] recently published appear to be dominated by photoconductivity effects.

Magnetoabsorption measurements[10] have resolved higher exciton states which determined the exciton binding energies. These measurements have also provided evidence of an exciton polaron (polarization of the crystal by the electric field of the exciton) effect.[47] Other polaron aspects, which have been investigated theoretically within the intermediate coupling regime,[48] include anisotropic polaron masses,[49] exciton binding energies,[50-53] and excited states.[54] Cyclotron resonance measurements[55-57] indicate that the masses are not highly anisotropic.

Two-photon absorption measurements[58-60] have given particularly well-resolved spectra of longitudinal optical (LO) phonon absorption and emission processes at the band edge. The LO phonon can couple strongly to the electric field of an electron or hole. These measurements have explained the temperature dependence of the band gap which increases with temperature in agreement with other CsCl structure crystals. The hydrostatic pressure dependence of the band gap[29,61,62] has also been studied and a negative coefficient has been determined. Other important information associated with the lattice includes experimental investigations which have provided thermal expansion coefficients,[63] lattice[24] and dielectric[64,65] constants, and LO phonon energies.[64,66]

In concluding this chapter experiments on samples of very high purity will be outlined briefly. This level of sample purity is unique to the Japanese workers and has been especially important in luminescence and photoconductivity measurements. The luminescence experiments[67-71b] have provided evidence of transitions at the indirect edge with pure and mixed crystals and these results have been supported by absorption data[72-75] on the same samples. The photoconductivity work has supplied information on the temperature dependence of carrier trapping and mobilities in surface and bulk regions. Evidence of carrier effects on applied electric fields has been obtained from electroreflectance[46] and electromodulated luminescence[75] measurements involving surface and bulk regions.

Table I summarizes some of the properties of sc TlCl and TlBr from the literature which will be useful in discussing the experimental results.

Table 1. Properties of sc TlCl and TlBr

	TlCl	TlBr
R (meV)	11.7[a]	9.8[a]
a_o(Å)	40-70 Å[b]	40-80 Å[b]
$\mathcal{E}_I$(V/cm)	$1.7\text{-}3.0 \times 10^4$[b]	$1.2\text{-}2.5 \times 10^4$[b]
$\hbar\omega_{LO}^{k=0}$ (meV)	21.5[c]	14.3[d]
ε_o	37.6[c]	35.1[c]
ε_∞	5.1[e]	5.41[e]

[a] Ref. 10.

[b] Estimates.

[c] Ref. 64.

[d] Ref. 66.

[e] Ref. 65.

CHAPTER IV. SAMPLES

Simple Cubic Samples

Developing samples which would allow electric field effects to be measured on well resolved intrinsic sc exciton states was the most difficult aspect of this investigation. Early samples were in the form of TlCl thin films evaporated on quartz substrates. The spectra of these samples were distorted by static strain at low temperature, preventing the observation of intrinsic exciton structure.

To improve resolution, samples were prepared, as described earlier, by evaporating films on very thin transparent organic membranes supported by frames cut from crystals of the material being evaporated.[10,33,34] This method had been highly successful for absorption and magnetoabsorption measurements[10,33,34] but proved difficult to adapt to electromodulation measurements due to the tendency of the film and membrane to couple and oscillate with the modulating electric field. The coupling is due to electric field inhomogeneities in the sample region, to small wrinkles which often occur in the film when it is cooled to low temperature, and possibly to photocarriers in the film. In the first two instances the coupling mechanism is analogous to the force which draws a dielectric into a high field region.

When the sample couples to the field, the transmitted light is modulated due to the strain shifting and broadening of absorption features. This AC signal is superimposed on the electromodulation signal, with a phase shift due to mechanical damping, at the modulation frequency. It cannot be separated from the electromodulation signal and prevents the undistorted detection of that signal. The spurious signal could not be substantially reduced by modulating at higher frequencies within the limitations of the electronics. The strain coupling could be directly observed with a microscope when the modulation frequency was swept through resonant vibrations of the membrane which corresponded with peaks in the modulated transmission as a function of modulating frequency.

The lack of success by numerous efforts to control the field coupling effect delayed progress in the experiment for several years. Efforts involved various methods to reduce sample wrinkling at low temperature, to generate a homogeneous or a stabilizing electric field in the sample region, and to physically support the film to restrict the motion of the sample. Stabilized TlBr samples were finally developed using membranes supported by solid TlCl single crystal frames. The TlCl crystal has a very similar thermal expansion coefficient and is transparent in the spectral region of the TlBr exciton structure, hence providing an ideal support. Earlier efforts to evaporate TlBr on TlCl had proven unsuccessful due to diffusion[76] between the film and substrate, which was recognized later. The organic membrane between the TlCl crystal and the TlBr film prevents diffusion at the interface. In addition it provides a slip plane to reduce strain in the film. The slip plane function of the membrane was observed in the electromodulated spectra of a sample when the membrane only partially released. The spectra showed the usual structure but with a replica structure shifted by strain to higher energy.

In the final measurements CsI was substituted for TlCl because it is transparent for the exciton region of both TlBr and TlCl and has a very similar thermal expansion coefficient[77] to the thallium compounds.[63]

The sc sample preparation procedure, for the final measurements, was as follows. Substrates to support and stabilize the membrane were cut from single crystals of CsI from the Harshaw Chemical Company. The substrate blanks were cut in the form of rectangular solids 0.19 cm x 0.33 cm x 1.17 cm and dressed with 500 grade emery paper before being glued together for polishing. Six blanks were glued together to reduce the rounding of edges on the inner blanks during polishing (the outer blanks were discarded). Since CsI is hygroscopic, polishing was done under water-free ethyl alcohol using 1.0, 0.5, and 0.03 micron alumina (Linde, Union Carbide), in that sequence, on AB Microcloth (Buehler Ltd.). After polishing, the glue was dissolved, allowing the substrates to be separated. Each received a final etch-polish with 0.03 micron alumina under methyl alcohol, which contains some water, was flushed with ethyl alcohol, and blown dry with a dual jet of dry nitrogen which cleared both optical surfaces simultaneously. Residues were prevented, in this way, which interfere with film formation and scatter light. The final crystal dimensions were approximately 0.16 cm x 0.30 cm x 1.14 cm.

The membranes placed on the CsI crystals were prepared from Plexiglas (Rohm and Hass, v/811 UVT) dissolved in ethylene dichloride with a trace of Formvar (Monsanto, 15/95 E) added. The concentration was 8 gm of Plexiglas per liter of ethylene dichloride. The membrane was fabricated by allowing a 5-6 µl drop of the solution to drip from a micro syringe onto a surface of distilled water from a height of 1-2 cm. The Formvar promotes wetting of the drop by the water, resulting in a rapid spreading of the drop over the water surface,somewhat like an oil slick. The membrane, which had a diameter of approximately 6.4 cm, was lifted off the water by allowing an edge to drape over a 0.020 cm thick smooth metal plate (4.3 cm x 6.4 cm) with a centered 2.2 cm round hole. An extension of the plate on one side, parallel to the 4.3 cm dimension, served as a handle for raising the plate vertically when lifting the membrane off the water. The unsupported area of the membrane, over the hole, was to be used on the crystal and care was required to avoid breakage. It initially was necessary to lift the unsupported area very slowly until the film of water, which adhered to the membrane, released. The 0.02 cm plate thickness was useful in reducing the thickness of the water film and allowed membranes as thin as 200 Å to be successfully lifted. The membrane thickness was found to be approximately 250 Å, for the solution concentration and drop size specified, from measurements with an interferometer (Varian, model 980-4000).

After the membrane was free of the water, it was inspected for defects under a microscope before mounting on the CsI crystal. A jig was used to mount the membrane. It allowed the membrane and substrate to establish contact smoothly without causing wrinkles or rips. The mounting was completed by smoothing the membrane to the surface of the CsI crystal with a soft jet of dry nitrogen gas through a hypodermic needle before cutting away the unused membrane with a razor blade.

The substrates were secured between the plates (separation 1.8 mm) of the sample holder with teflon pads cut from teflon tape. The teflon served as insulation to block electron injection luminescence, when the electric field was applied between the plates, and padded the substrate during cool-down. A small glass plate was placed adjacent to the sample for interferometric film thickness determination. The sample holder appears in Figure 7, which shows the sample subsrate and glass plate without the thin teflon pads.

At this point the cryostat, with the sample holder and substrate attached, was placed in its position above the sample chamber with the cold finger extending into the sample chamber so that the substrate was positioned for the evaporation and light beams.

The quartz evaporation boat was charged with chips of single crystal TlCl or TlBr of nominal purity from the Harshaw Chemical Company. The chips were etched before loading with boiling distilled water, to remove any impurities which might have become imbedded during chipping, and dried under vacuum. The quartz boat was heated by a tantalum heater and the evaporation beam was emitted by a secondary sublimation from the thallium halide deposited on the wall of the boat opposite the beam opening by the initial crystal sublimation in the bottom of the boat.

When a vacuum in the high 10^{-7} to low 10^{-6} Torr range was obtained in the sample chamber, the evaporation boat was positioned directly in front of the thickness monitor head (Sloan, 103-758) as shown in Figure 8. An evaporation rate between 40 and 60 Å/min was established by varying the current through the tantalum heater by adjusting the resistance

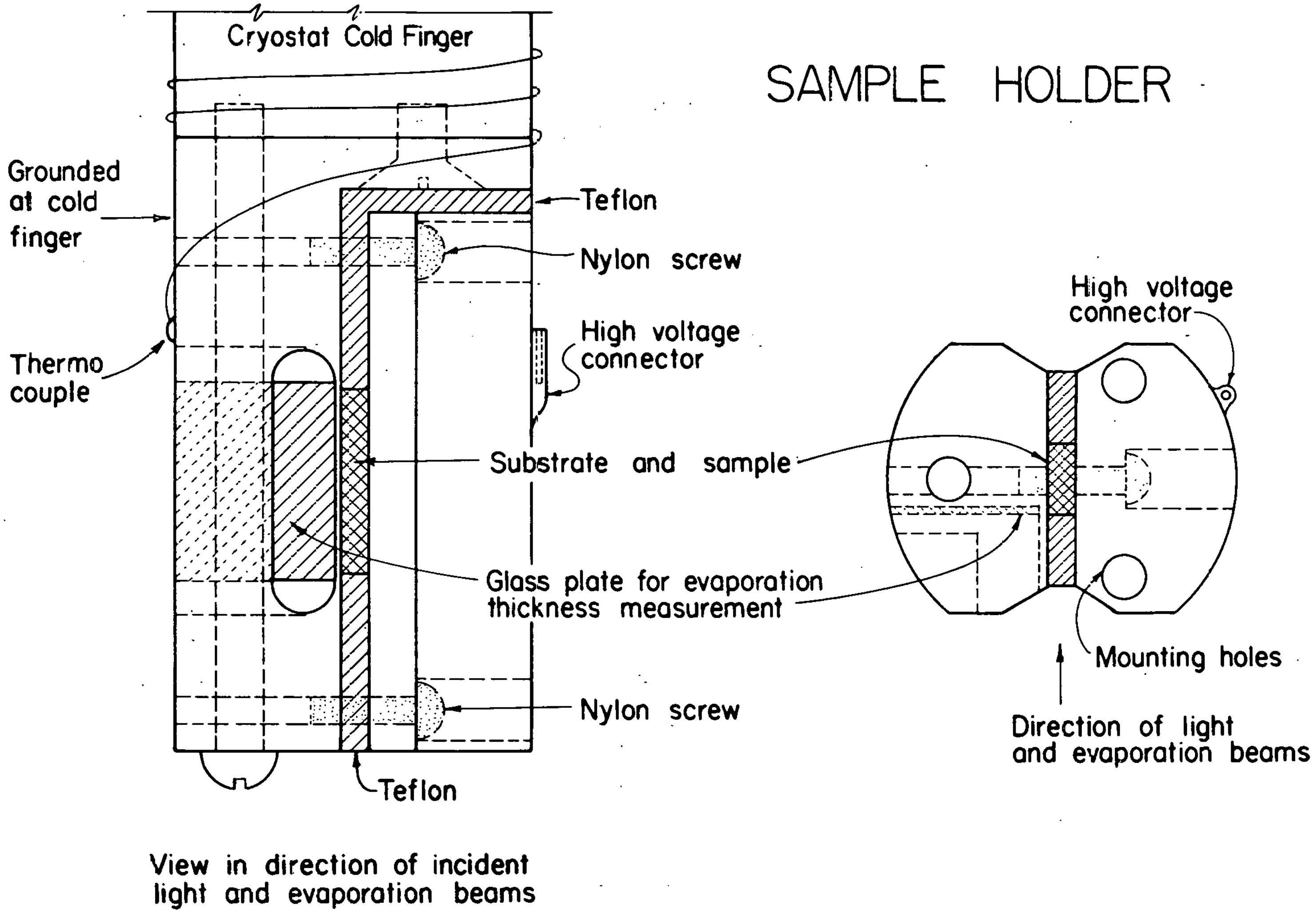

Figure 7. Two views of the capacitor sample holder

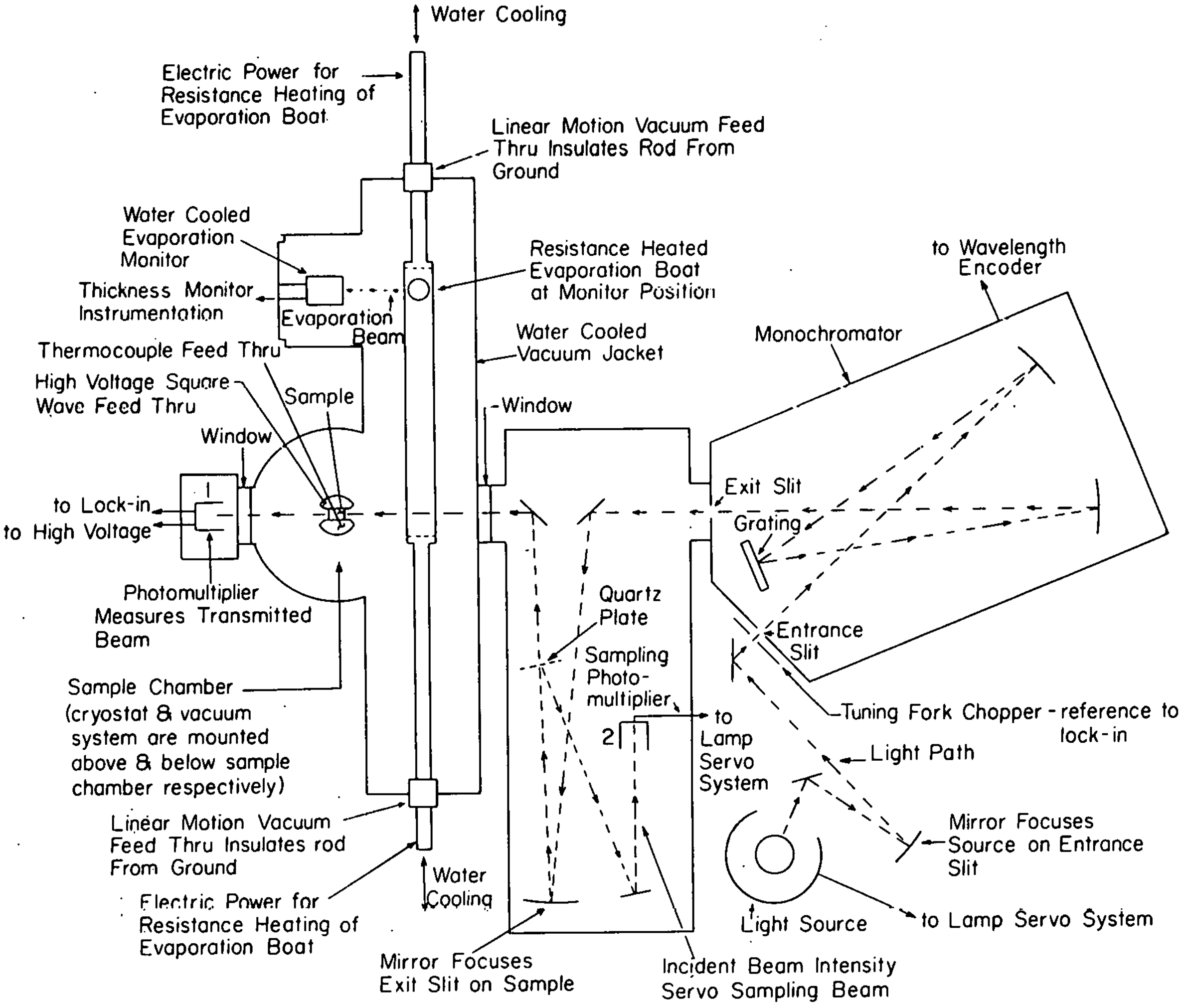

Figure 8. The experimental apparatus

evaporation power supply (Ultek, 60-300) output. The rate was determined by plotting the output signal of the thickness monitor (Sloan, DTM 3) as a function of time with the chart recorder (Hewlett-Packard, 7100B) and calculating the rate from the slope of this plot. The electric power was conducted, as shown in Figure 8, to the tantalum heater by its support frame and by the linear translation rods which allow the evaporation source to be positioned at the monitor or substrate locations. The linear translation vacuum seals were Cenco seals, modified to have two O-rings, and protected from heating by coaxial water cooling of the translation rods. Water cooling was also supplied to the thickness monitor head and vacuum jacket region adjacent to the evaporation source positions.

After a stable evaporation rate between 40 and 60 Å/min had been obtained, the source was translated to the position directly in front of the substrate and left there for the time period necessary to deposit the thickness desired in a range between 500-700 Å. A film was simultaneously deposited during this time on the glass plate which was positioned adjacent to the substrate for interferometric thickness determination. The low limit on film thickness was imposed by a problem of disorder often found in thallium halide films below 500 Å thickness. The upper limit was set by a need to control photocarrier effects in the electromodulation measurements rather than by the large optical density at the $n = 1$ exciton peak.

After evaporation the sample was left at room temperature for several hours before being slowly cooled to liquid nitrogen temperature to avoid thermal strain. It was then cooled more rapidly to the 5-6°K range where the spectra were measured as described in the next chapter.

Face Centered Cubic Samples

The abnormal fcc phase samples were evaporated in the system just described at very low rates of 1-5 Å/min, as indicated by the thickness monitor, and formed epitaxially on KBr substrates freshly cleaved from Harshaw single crystals. The evaporation rate was detected for sc phase formation on the film thickness monitor crystal. Films were evaporated to monitor thicknesses less than 100 Å because the fcc is stable only for thicknesses below 200 Å. The evaporation was done at a pressure in the 10^{-5} Torr range to promote epitaxial film growth. After evaporation the vacuum was quickly pumped to the low 10^{-6} Torr range and the sample was rapidly cooled to liquid nitrogen temperature where the fcc phase is more stable. Measurements were made often at both 77°K and in the 5-6°K range, although very little reduction in broadening occurs at the lower temperature due to the higher Debye temperature of the fcc phase relative to the sc phase. To obtain higher fields for the fcc samples the sample capacitor plate separation was reduced to 1.4 mm.

CHAPTER V. EXPERIMENTAL MEASUREMENT SYSTEM

The experimental measurement system enabled the determination of the transmission, T, and electromodulated transmission, ΔT/T, spectra of samples at low temperature. A schematic view, from above, of the measuring system appears in Figure 8. It includes the optical arrangement, sample chamber with holder, and the evaporation system. The vacuum pumping and cryogenic systems and electronics are not shown.

Transmission Measurements

The operation of the system in the transmission mode is shown in the block diagram of Figure 9. Starting in the upper right-hand corner at the light source (General Electric Quartzline 500 watt tungsten filament lamp) the optical path can be followed to the tuning fork chopper (Bulova-American Time Products L40 driven by oscillator AME-5A) which gives the beam an AC component for compatibility with the detection electronics. The beam reaches its first focus at the entrance slit of the monochromator (McPherson 218, 1200 grooves/mm 5000 Å blaze grating) and passes through the monochromator, refocusing at the exit slit in a wavelength band of 26.5 Å/mm of slit width. Slit widths ranged between 30 and 60 microns corresponding to band passes from 0.8 to 1.6 Å or approximately 0.7 to 1.4 meV. The beam is focused from the exit slit to the sample and the fraction that is transmitted falls on the photocathode of photomultiplier 1 (RCA 1P28), which is powered by a constant high voltage supply (Keithley 244). A small fraction of the beam is reflected, before the sample, from a quartz plate to photomultiplier

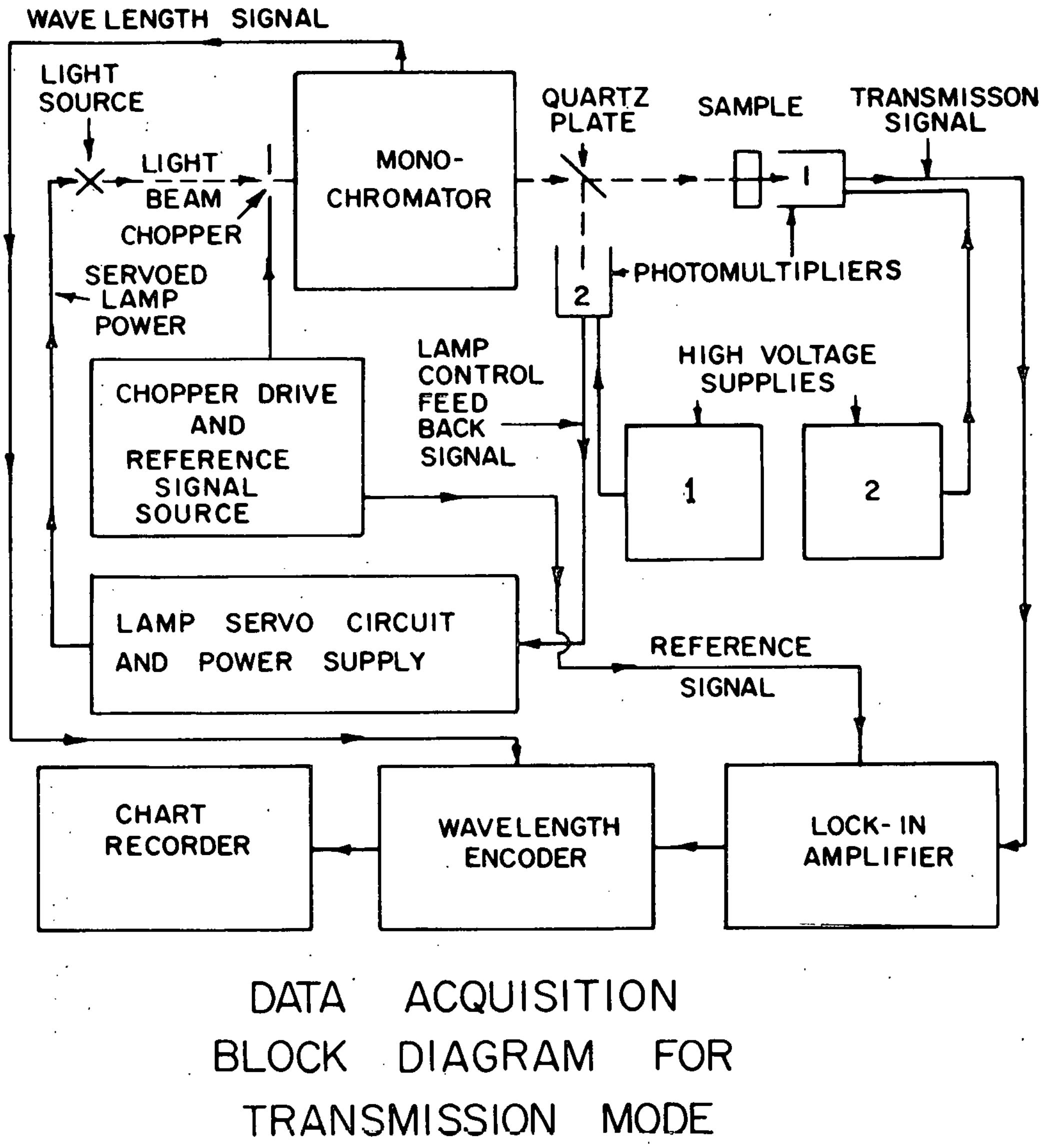

Figure 9. Block diagram of the system for transmission measurements

2 (RCA 1P28), which is part of a servo loop for maintaining a nearly constant incident beam intensity on the sample. The high voltage supply (Power Designs 2K-10) for photomultiplier 2 is also held at constant output. The servo loop can be traced in Figure 9 to the lamp servo circuit and power supply (Instrumentation Group, Ames Laboratory MF211) before returning to the lamp. The servo loop removes spurious spectra from the incident beam due to the lamp spectrum and optics by adjusting the power to the lamp after automatically comparing a feedback signal from photomultiplier 2 with a reference signal from a mercury battery. The servo system enables the absorption spectra to be directly observed without the superposition of the highly wavelength dependent unservoed incident beam variation which distorts the spectra. The AC signal from photomultiplier 1, which is proportional to the transmitted beam intensity, is measured by a lock-in amplifier (Ithaco 353) which receives a synchronizing reference signal from the chopper drive circuit. The synchronous lock-in detection allows the detector to have a narrow band width response, thus improving the signal-to-noise ratio. The DC lock-in output signal is recorded as a function of wavelength by the chart recorder (Hewlett-Packard 7100 B) after having wavelength reference pips added by the wavelength encoder which was calibrated with Osram spectral line source lamps. Finally, the sample and substrate transmission are obtained by taking a ratio of this plot to a similar plot taken with the sample and substrate removed from the beam.

Electromodulated Transmission, ΔT/T, Measurements

The ΔT/T measuring system mode is shown in Figure 10. Again the light path can be followed from the lamp through the monochromator to the sample, where the transmission is modulated by the applied electric field. In this mode the AC signal is developed at the sample rather than at the tuning fork chopper. The modulating field is applied between the plates of the sample mount capacitor (Figure 7) by means of a voltage applied across the capacitor plates from the high voltage square wave generator, which is discussed later in the chapter. The transmission modulation occurs at photon energies where field-sensitive absorption features exist, such as the n = 1 exciton line, which is broadened and shifted by the field. This causes the superposition of a small AC signal, which is proportional to ΔT/T, on the DC transmission signal. Both of these signals go to the constant DC signal servo system which is described below. The servo system maintains a constant DC transmission signal level by varying the photomultiplier high voltage and hence automatically causes the AC signal to be proportional to ΔT/T. It also separates the AC and DC signal components. The former is measured by the lock-in and the output, S_{AC}, is recorded with the DC signal, S_{DC}, on the chart recorder after the wavelength has been encoded. In terms of S_{AC} and S_{DC}, ΔT/T is obtained from $\Delta T/T = 2\, S_{AC}/(S_{DC} - S_{AC})$. The servo system feedback loop which holds S_{DC} constant is shown in Figure 11. The signal is generated when the modulated beam causes electrons to be emitted at the photomultiplier cathode. Secondary electron emission occurs at each of the 9 dynodes which electrostatically accelerate the electrons to the anode,

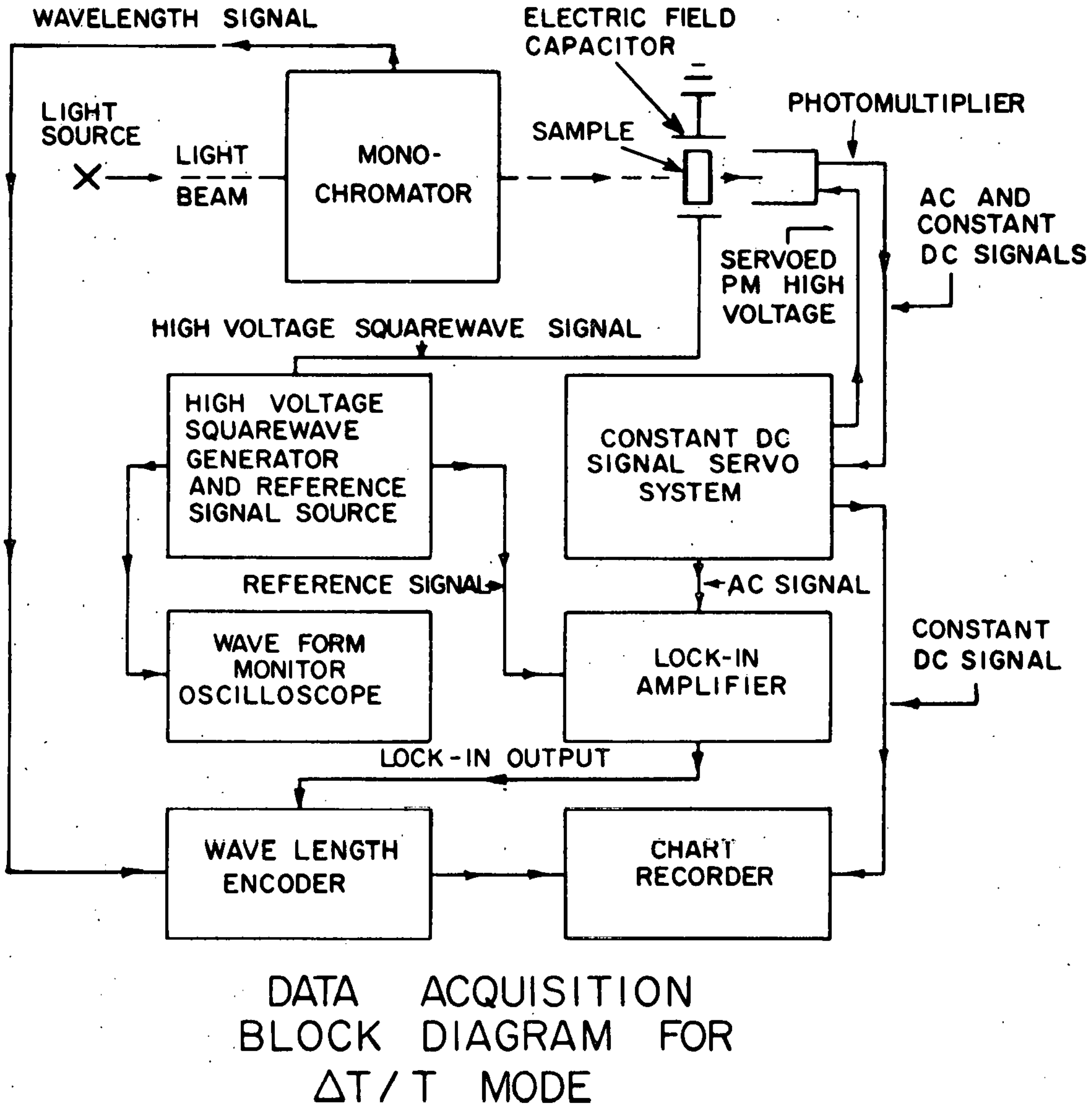

Figure 10. Block diagram of the system for electromodulated transmission measurements

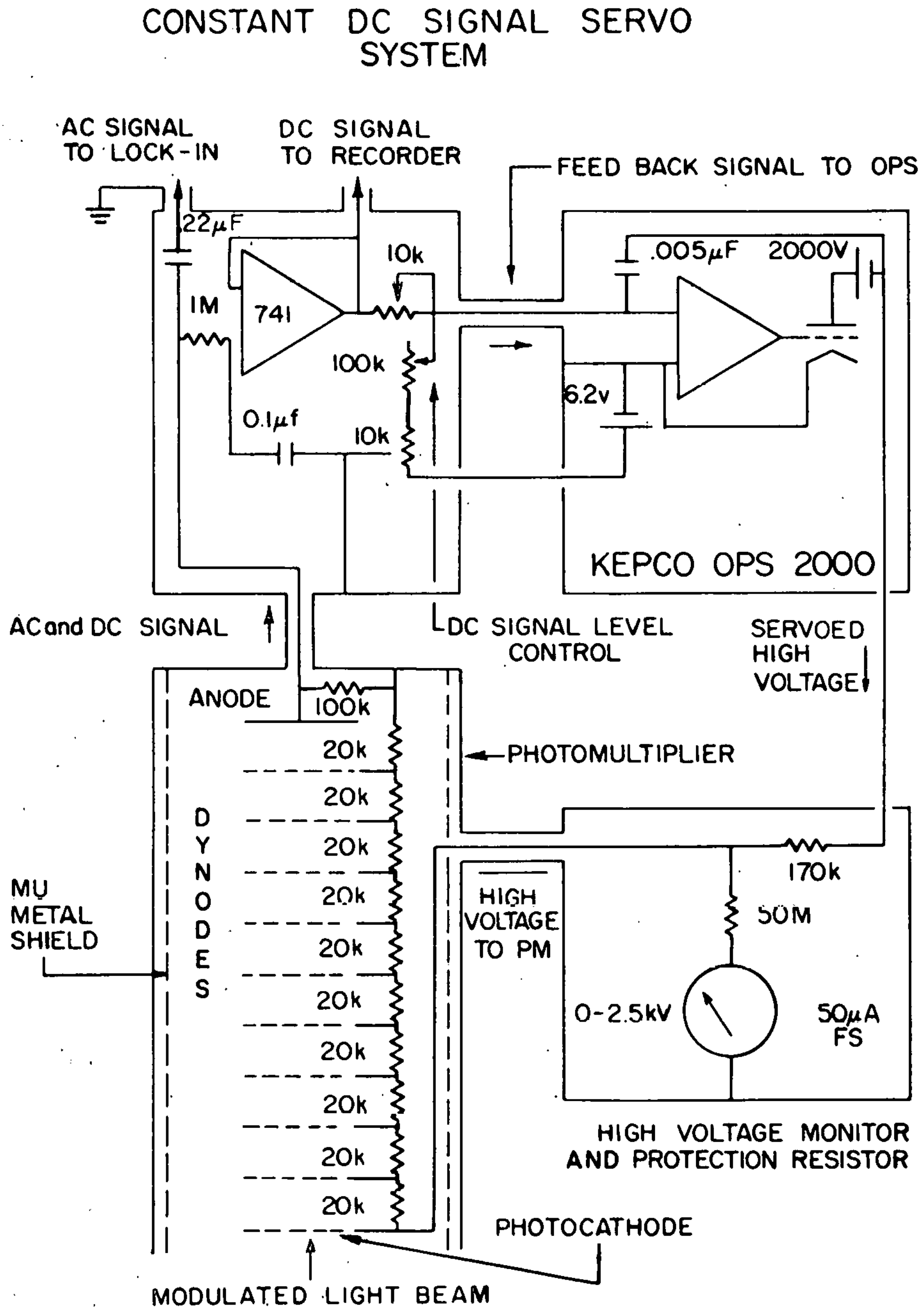

Figure 11. The servo system for ΔT/T measurements

producing a multiplying effect. Electrons are conducted from the anode to ground through the 100 K Ω resistor. The AC component of the voltage signal developed across the resistor is conducted through the 0.22 μF capacitor to the lock-in input. The DC signal appears at the input of the 741 operational amplifier after the AC has been filtered by the 0.1 μF capacitor. The 741 operational amplifier has unit gain and serves to match impedence between the photomultiplier and the Kepco operational power supply (Kepco OPS 2000) and to supply the DC signal level to the chart recorder. The imput of the Kepco OPS 2000 is the null point of the servo system. It receives a constant voltage from the 6.2 V supply which may be adjusted by the 10 and 100 K resistors. This constant voltage level determines the DC transmission signal level which will be maintained by the servo system. The null point also receives a voltage from the 741 operational amplifier. If this is greater (less) than the constant voltage from the 6.2 V source as the spectrum is scanned, the Kepco OPS 2000 automatically reduces (increases) the high voltage across the photomultiplier, thus reducing (increasing) the gain of the tube and reestablishing the null. The Kepco OPS 2000 also has a direct AC feedback through the 0.005 μF capacitor to reduce any AC noise that is picked by the control circuit. Before the high voltage reaches the photomultiplier it passes through a 170 KΩ protection resistor and is monitored by a 0 - 2.5 kV meter.

High Voltage Square Wave Generator[78]

The high voltage square wave generator is shown schematically in Figure 12. The low voltage square wave generator was constructed from

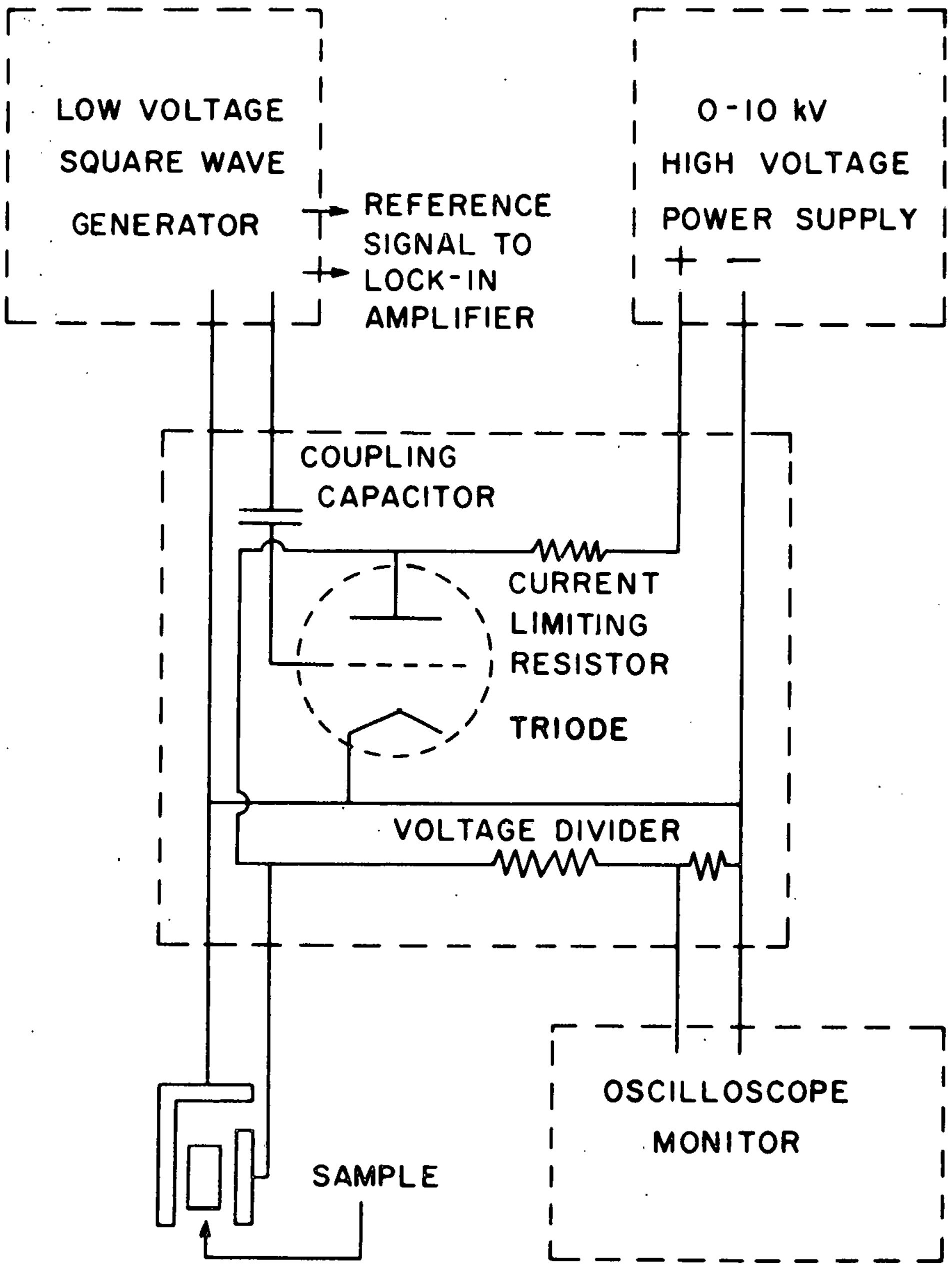

HIGH VOLTAGE SQUARE WAVE SYSTEM

Figure 12. Schematic of the high voltage square wave generator

a sinewave oscillator (Hewlett Packard Model 200 CD) which turned a transistor alternately on and off to generate a square wave with a duty cycle which could be adjusted by the sinewave amplitude to a value of 50%. The oscillator also provided a reference signal to the chopper. The square wave was coupled to the grid of a high voltage triode with a capacitor. The triode was turned on and off by the grid causing the 0 - 10 KV high voltage power supply (Sorensen 5010) connected across the sample capacitor to be shorted out periodically, generating a square wave electric field on the sample. The high voltage square wave was monitored by an oscilloscope (Textronix 531A) through a voltage divider. The high voltage supply had a current capability of 8 ma which was protected by a current limiting resistor. The current limitation provided the restraint on the frequency response of the generator. With a low capacitance cable to the sample capacitor, operation at 200 Hz was possible with very little distortion of the square wave. A 50 percent duty cycle square wave modulation was required by both the lock-in amplifier and the model used in the calculation. The lock-in output is sensitive to the input duty cycle, while the theory involves taking the difference between spectra calculated for two fields ($\mathcal{E} = 0$ and $\mathcal{E} \neq 0$), thus requiring square wave modulation.

Vacuum System

The vacuum system provided a low pressure atmosphere in the sample chamber which was necessary to enable the sample to be isolated from thermal contact for cooling to low temperature without condensation and the in situ evaporation of thin film samples. The light beam incident on the samples after evaporation entered and exited the evacuated chamber through Suprasil quartz windows sealed with 0-rings.

The vacuum pumping system consisted of a liquid nitrogen cold trapped diffusion pump (T-M Vacuum Products TM 241 AC) mounted directly below the sample chamber and roughed by a mechanical rotary pump (Welch 1405). A combination poppet/butterfly type valve between the cold trap and sample chamber allowed rapid cycling of the system when it was necessary to open the sample chamber. Cold cathode vacuum gauge instrumentation (Instrumentation Group, Ames Laboratory MF-14-A) measured the pressure in the sample chamber. The pressure could be adjusted between 10^{-5} and $5{:}10^{-7}$ Torr by throttling the diffusion pump with the poppet/butterfly valve.

Cryogenic System

The cryogenic system was necessary to reduce the thermal broadening of the spectra. The system consisted of a liquid nitrogen shielded liquid helium cryostat which was mounted directly above the sample. The cryostat had been used in the group previous to this investigation. The sample holder (Figure 7) was bolted to the copper cold finger which was in contact with the liquid helium reservior. The 0.8 liter reservior capacity allowed approximately 3 hours between fills. The cold finger and sample holder were shielded by a concentric copper tube which was in contact with the liquid nitrogen container. The tube had holes cut in its sides to allow the passage of the evaporation and light beams. An Au + 0.03 at % Fe vs. Cu thermocouple was attached to the sample holder with General Electric 7031 varnish. Thermocouple emfs were measured with a digital microvoltmeter (Newport 2400) relative to ice. Temperatures between 5 and 6 K were measured when liquid helium was in the cryostat. Unfortunately it was not possible to control the temperature between this value and nitrogen temperature.

CHAPTER VI. DATA REDUCTION AND INTERPRETATION METHODS

The reduction and interpretation methods used for the data fit into two categories. In the first, the ΔT/T and T data obtained for the normal (sc) phase samples were reduced, using the standard thin film formulas[79] derived from Maxwell's equations, to provide values of the complex index of refraction (N = n + ik) and dielectric constant ($\varepsilon = \varepsilon_1 + i\varepsilon_2$) and the electric field-induced changes in these quantities. The reflectivity and electromodulated reflectivity were calculated from the above results. The TlBr abnormal (fcc) phase ΔT/T data were interpreted in the second method using Wannier exciton theory with no central cell correction to obtain the exciton binding energy and Bohr radius, bandgap, and static dielectric constant. A lack of well-resolved structure prevented the normal (sc) phase data and the abnormal (fcc) TlCl data from being interpreted by the second method and the lack of sufficient data to yield values of the complex index of refraction restricted the first method from use with the abnormal (fcc) phase data.[80]

Normal Phase Data

In the first method, values of n and k were obtained as a function of photon energy from data in the literature[81] and the experimentally measured transmission. The literature values had to be adjusted to fit the higher broadening associated with the spectra of this investigation. This was accomplished by programming the computer to search over ranges, defined by the literature values, of n and k to locate values which produced a calculated transmission within a specified tolerance of the experimental measurement. This procedure resulted in multiple solutions and the final values of n and k were determined by starting at low photon energy where k = 0 and n is known, and working graphically to higher energy, using requirements of continuity of n and k pairs, the known general functional form for n and k in this region, and numerous check plots to compare the calculated and measured transmission. The values of n and k finally obtained for both TlCl and TlBr gave calculated transmission spectra which were coincident with the experimental spectra within the resolution of the incremental plotter.

The transmission was calculated from the two-layer normal incidence thin film formula[79] with boundary media of vacuum on the incident side and CsI on the transmission side. The first layer was the evaporated thallium halide film and the second, the plexiglas membrane. The neglected reflection at the CsI-vacuum interface was corrected for by a factor calculated from the CsI index of refraction, which was nearly constant in the range of interest. The indices of refraction at liquid nitrogen temperature for the CsI crystal and the plexiglas membrane were obtained in the former case from the literature[82] and in the latter from a transmission measurement on a spectrophotometer (Cary 14). The transmission data were reduced using the single-layer thin film formula.[78] Since in this photon energy region no sharp structure exists (k = 0) the values of n are expected to be valid also in the 5-6 K region for both materials.

The program outlined above to obtain the complex index of refraction of TlCl and TlBr was used because the limited spectral range of the data prevented a Kramers-Kronig analysis, which would have provided two equations for the determination of n and k. In effect, this program obtained two unknowns (n,k) from one equation (the sample transmission) and additional information not in the form of an equation. For this reason the accuracy of n and k is subject to some question. In view of the uncertain reliability of some Kramers-Kronig analyses, which require additional approximated data for execution, the program does not seem unreasonable.

Kramers-Kronig analysis was used on the $\Delta T/T(h\nu,\mathcal{E})$ data to obtain the electric field-induced change in the transmission phase shift, $\Delta\Theta(h\nu,\mathcal{E})$, of the electromagnetic wave associated with light transmitted through the sample. The equations for $\Delta T/T$ and $\Delta\Theta$ provided the two equations necessary to obtain the field induced changes in the complex index of refraction, Δn and Δk. The Kramers-Kronig integral could be evaluated, in this case, in the region of measurement because other regions make a small contribution to the integral, since $\Delta T/T$ in those regions has a low amplitude which is not enhanced by the functional form of the integrand when $\Delta\Theta$ is calculated for photon frequencies in the region of interest. This can be seen from the expression for $\Delta\Theta$ given by

$$\Delta\Theta(\omega,\mathcal{E}) = \frac{\nu}{\pi} P \int_{\nu_\ell}^{\nu_h} \frac{\ln[1 + \Delta T/T(\nu_o,\mathcal{E})]\, d\nu_o}{\nu_o^2 - \nu^2} \qquad (18)$$

where ν and $\mathcal{E}$ denote the photon energy and electric field. The symbols ν_ℓ and ν_h define the limits of the measured region. Equation 18 was obtained from the Kramers-Kronig phase shift formula[83] due to transmission by substituting the expressions: $T(\nu_o, \mathcal{E} = 0)$ and $T(\nu_o, \mathcal{E} \neq 0) = T(\nu_o, \mathcal{E} = 0) + \Delta T(\nu_o, \mathcal{E} \neq 0)$ into the formula and subtracting the two resulting equations. The integration to obtain $\Delta\Theta(h\nu, \mathcal{E})$ was done by computer.

The values of Δn and Δk were derived from the following equations

$$\Delta T/T = \frac{1}{T}\frac{\partial T}{\partial n} \Delta n + \frac{1}{T}\frac{\partial T}{\partial k} \Delta k \qquad (19)$$

$$\Delta\Theta = \frac{\partial \Theta}{\partial n} \Delta n + \frac{\partial \Theta}{\partial k} \Delta k \qquad (20$$

with the partial derivative quantities obtained from the two layer thin film formula[78] and the complex index of refraction results discussed earlier. All of the above results were then used to calculate the complex dielectric constant and the electric field induced changes in that quantity using the following expressions,

$$\varepsilon_1 = n^2 - k^2 \qquad (21)$$

$$\Delta\varepsilon_1 = 2n\Delta n - 2k\Delta k \qquad (22)$$

$$\varepsilon_2 = 2nk \qquad (23)$$

$$\Delta\varepsilon_2 = 2k\Delta n + 2n\Delta k \quad . \qquad (24)$$

In addition, R and $\Delta R/R$ were calculated from

$$R = \frac{(n - 1)^2 + k^2}{(n + 1)^2 + k^2} \tag{25}$$

$$\frac{\Delta R}{R} = \frac{\partial R}{\partial n} \quad \Delta n + \frac{\partial R}{\partial k} \quad \Delta k \tag{26}$$

where

$$\frac{\partial R}{\partial \begin{smallmatrix}(n)\\(k)\end{smallmatrix}} = \frac{2\begin{smallmatrix}(n-1)\\(k)\end{smallmatrix}[(n+1)^2 + k^2] - 2\begin{smallmatrix}(n+1)\\(k)\end{smallmatrix}[(n-1)^2 + k^2]}{[(n+1)^2 + k^2]^2} \tag{27}$$

Abnormal Phase Data

The abnormal phase data were interpreted by using the Wannier exciton model, with no central cell correction, to calculate the band gap energy, Eg, and the exciton binding energy, R. Equations (6), (9), and (10) give the energy difference, E, between the valence band and the nth exciton state for $\vec{k} = 0$ as

$$E = Eg - R/n^2. \tag{28}$$

From Equation (28) spectral structure associated with the nth exciton state is expected at photon energies, $h\nu$, given by

$$(h\nu)_n = Eg - R/n^2 \tag{29}$$

The exciton transition energies, $h\nu$, are expected to closely coincide with the negative EA peaks, since field broadening and splitting are dominant in defining EA structures for excitons. The n=1 and 2 features are usually most clearly resolved. Eg and R can be determined from the two equations obtained for $(h\nu)_1$, and $(h\nu)_2$ from Equation (29).

$$Eg = 1/3\ [4(h\nu)_2 - (h\nu)_1] \tag{30}$$

$$R = 4/3\ [(h\nu)_2 - (h\nu)_1] \ . \tag{31}$$

The static dielectric constant, ε_o, and the Bohr radius, a_o, can be calculated from Equations (11) and (12) using the electron and hole effective masses from the band structure calculations. Equation (13) then allows the ionization field, $\mathcal{E}'_I$, to be calculated.

CHAPTER VII. RESULTS

Normal (sc) Phase Results for TlCl and TlBr

Normal phase results for both compounds are given in the form of the electromodulation spectra, $\Delta T/T$, $\Delta\varepsilon_1$, $\Delta\varepsilon_2$ and $\frac{\Delta R}{R}$ at two of the applied voltages used in the measurements. The unmodulated spectra are included in each plot for comparison. Additional figures show $\Delta T/T$ and $\Delta\varepsilon_2$ on the same plot to contrast the input and output of the data reduction program. Absorption and EA spectra for TlCl and TlBr are shown from runs which were not reduced by the data program. Finally, an interesting example of the effect of photoconductivity is shown in the electromodulation spectra of TlBr measured over a range of sample temperatures.

$\Delta T/T$ spectra

Figures 13 and 14 show the spectra for TlCl and TlBr, respectively. In the TlCl transmission spectrum the shoulder marked 1' is due to the splitting of the n=1, peak marked 1. Strain broadening prevents the observation of the actual doublet in Figure 13. The shoulder is not observed in the TlBr spectrum in Figure 14 due to a smaller splitting and more thermal broadening caused by the lower Debye temperature for this compound. At higher photon energies, in both spectra, the higher split and unsplit exciton states and phonon features are marked at locations designated by the spectra, when possible, or at locations calculated from the exciton binding energies and LO phonon energies.[10] The exciton-phonon quasibound state is designated by α and the free phonon sideband by β for the normal phase.

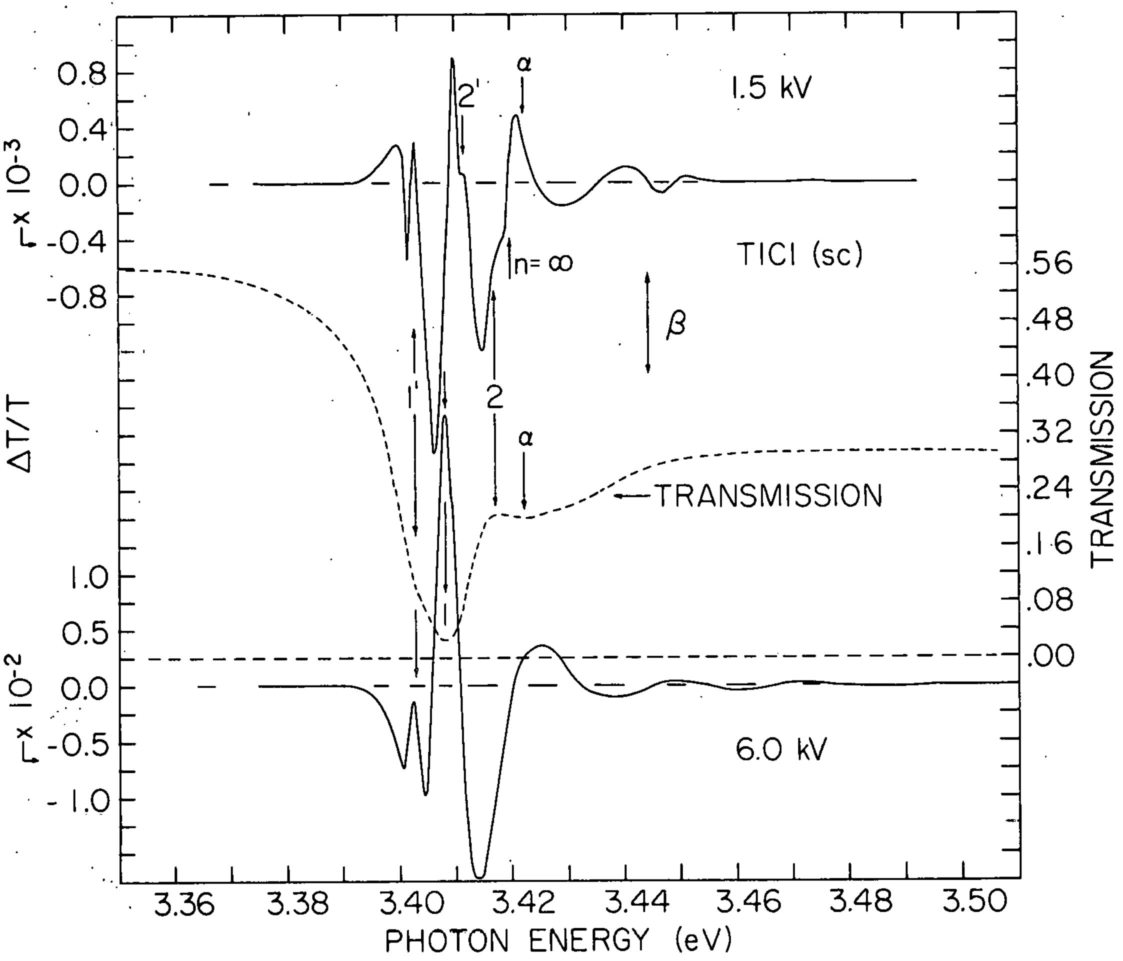

Figure 13. Transmission (dotted line) and ΔT/T spectra of TlCl (sc)

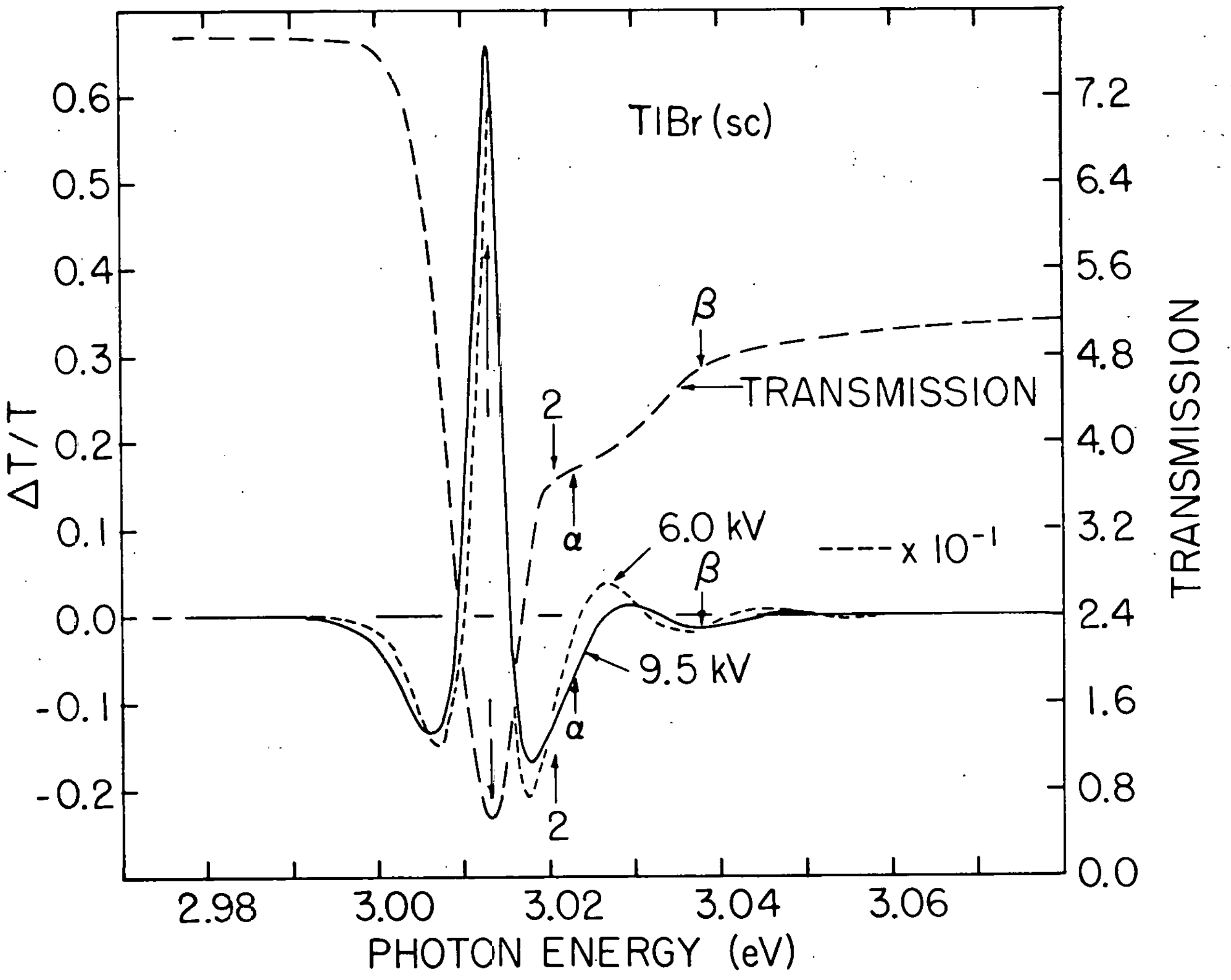

Figure 14. Transmission (dashed line) and ΔT/T (dotted and solid lines) spectra of TlBr (sc)

The ΔT/T spectra show more structure than the T spectra, especially in the case of TlCl, because of the higher exciton binding energy, larger splitting, and lower thermal broadening, relative to TlBr. In the TlCl ΔT/T spectra for 1.5 kV, the 1' feature is positive, due to the shifting and broadening of the state by the electric field, which causes enhanced transmission at the photon energy region corresponding to 1'. The positive feature on the low energy side of 1' is thought to be due to luminescence caused by photocarriers accelerated by the applied electric field, and not to exciton states. The positive ΔT/T feature on the high energy side of 1', in the absence of the n=1 splitting, would be expected at the location designated by 1. It is at higher energy due to superposition of the n=1' structure in this region. Other features in the 1.5 kV spectra are thought to correspond to the n=2' and 2 exciton states. At photon energies above $n = \infty$ the oscillations in the modulated transmission are seen which are similar to the structure seen in Blossey's calculated $\Delta\varepsilon_2$ spectra in Figure 2. The TlCl ΔT/T spectra for 6.0 kV show features at 1' and 1 with the oscillatory structure above $n = \infty$. The 1' and 1 ΔT/T peaks coincide closely with the corresponding transmission peaks, indicating that the superposition shifting effect is less active at higher fields. The n=2' and 2 features have disappeared due to ionization.

The spectra for TlBr in Figure 14 show the sensitivity of the spectra to the lower binding energy and larger thermal broadening of TlBr. The detailed structure observed in the TlCl spectra is absent at the fields shown and also at lower and intermediate fields.

$\Delta\varepsilon_1$ spectra

In Figures 15 and 16 the calculated ε_1 and $\Delta\varepsilon_1$ spectra appear for TlCl and TlBr, respectively. The main effect of the electric field is to broaden and attenuate the positive and negative ε_1 peak heights. This is most clearly seen in the TlBr and high field TlCl $\Delta\varepsilon_1$ spectra.

$\Delta\varepsilon_2$ spectra

Figures 17 and 18 show the ε_2 and $\Delta\varepsilon_2$ spectra calculated for TlCl and TlBr, respectively. The TlCl n=1 ε_2 peak is narrower than the transmission feature with the shoulder (peak) corresponding to the 1' (1) transmission feature shifted 1 meV to higher (lower) photon energy. The electromodulated $\Delta\varepsilon_2$ structure shows that the ε_2 peak is broadened and reduced in height by the field. The TlBr ε_2 spectra also exhibit a narrowing of ε_2 relative to T with a 1 meV shift in the ε_2 peak to lower photon energy. The $\Delta\varepsilon_2$ spectra are similar to the TlCl spectra but less resolved, as were the TlBr $\Delta T/T$ spectra.

$\Delta R/R$ spectra

Figures 19 and 20 show the calculated R and $\Delta R/R$ spectra, which were calculated for TlCl and TlBr to compare with recently reported measurements[46] discussed in the next chapter.

$\Delta T/T$ and $\Delta\varepsilon_2$ spectra

In Figures 21 and 22 the $\Delta T/T$ and $\Delta\varepsilon_2$ spectra are plotted in the same figure for TlCl and TlBr to allow comparison of the input and output of the data reduction program. The spectra show some shifting of

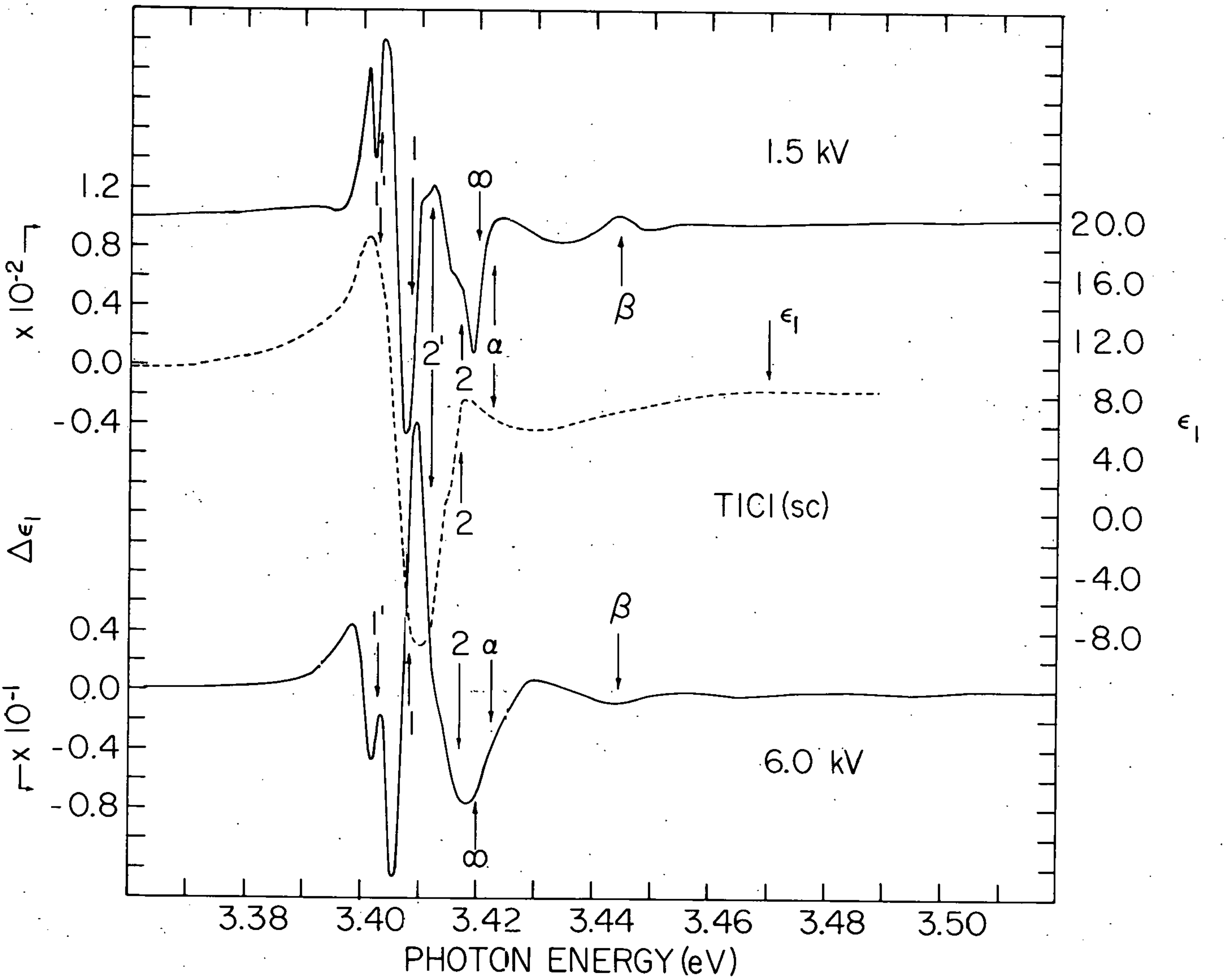

Figure 15. $\Delta\varepsilon_1$ spectra (solid lines) and ε_1 spectrum (dotted line) of TlCl (sc)

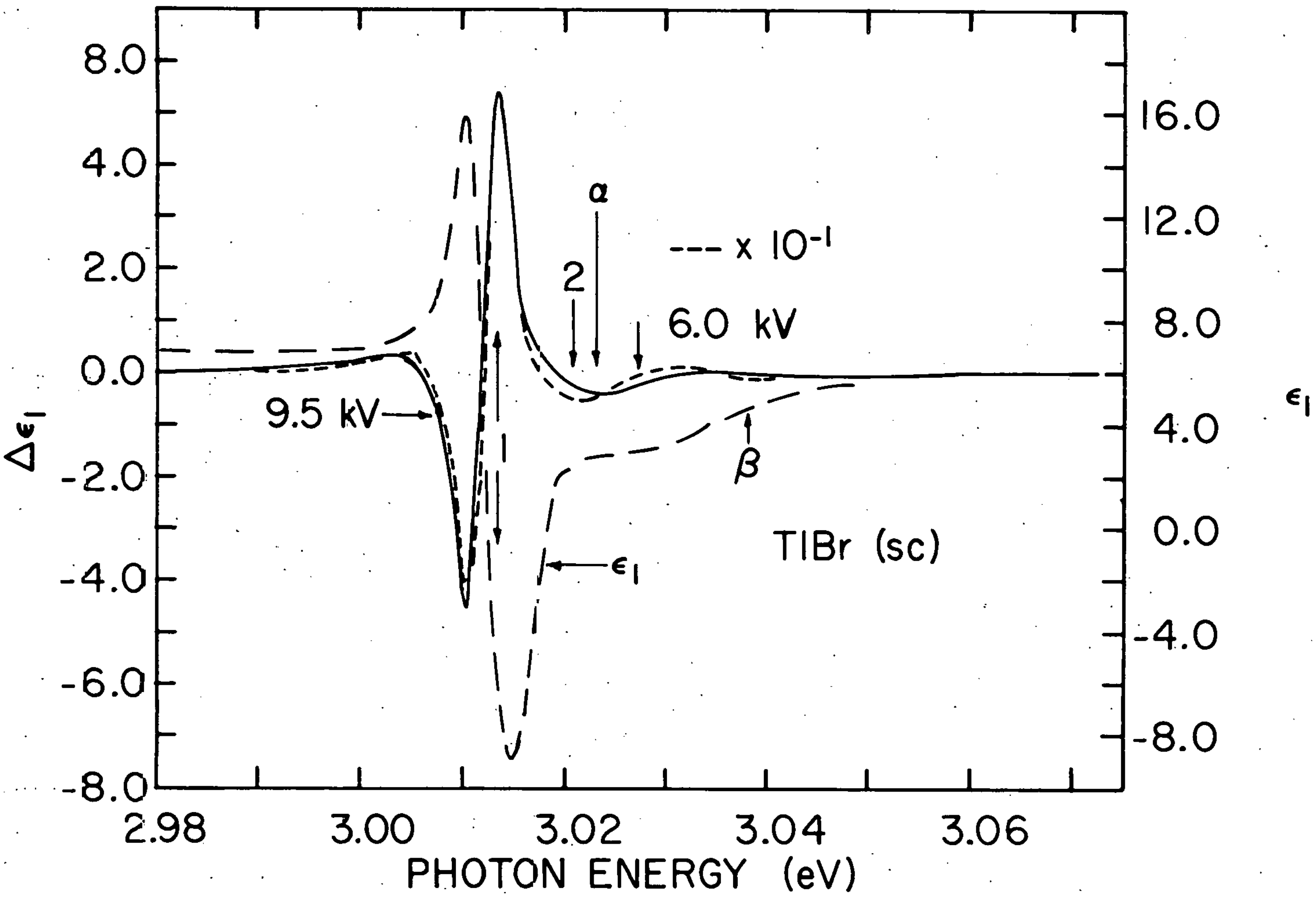

Figure 16. $\Delta\varepsilon_1$ spectra (solid and dotted lines) and ε_1 spectrum (dashed line) of TlBr (sc)

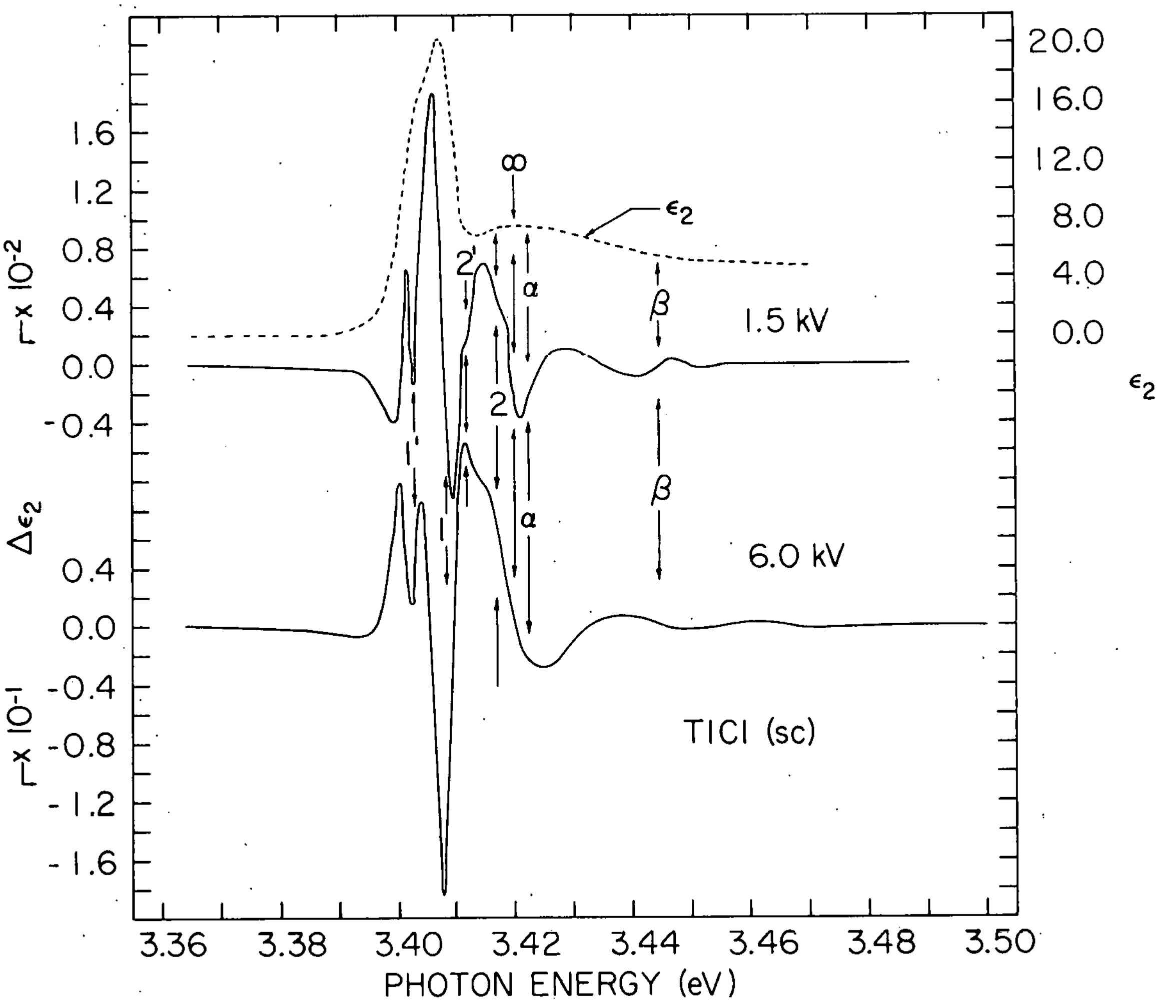

Figure 17. $\Delta\varepsilon_2$ (solid lines) and ε_2 (dotted line) spectra calculated for TlCl (sc)

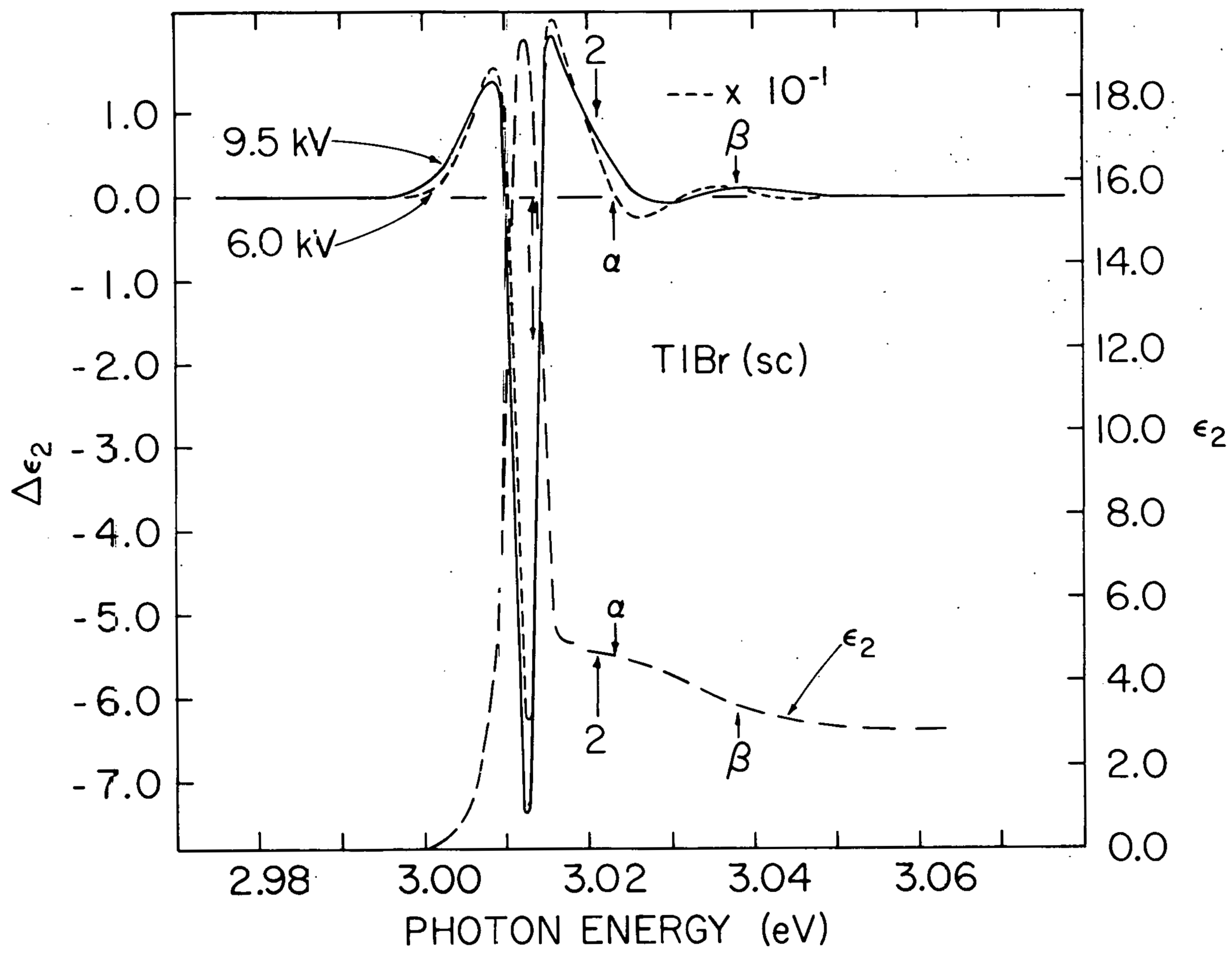

Figure 18. $\Delta\varepsilon_2$ (solid and dotted lines) and ε_2 (dashed line) spectra calculated for TlBr (sc)

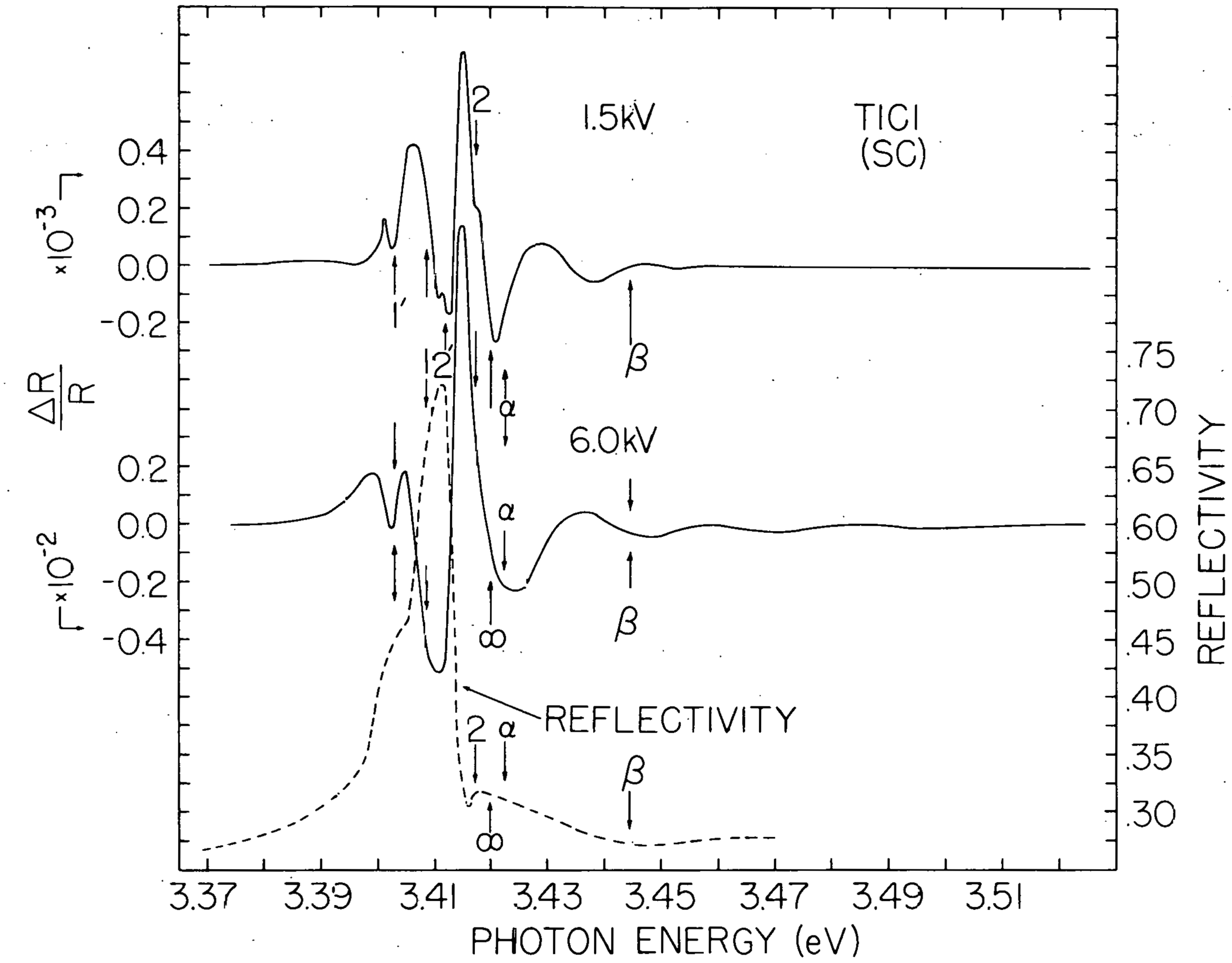

Figure 19. Calculated reflectivity (dotted line) and ΔR/R (solid lines) spectra of TlCl (sc)

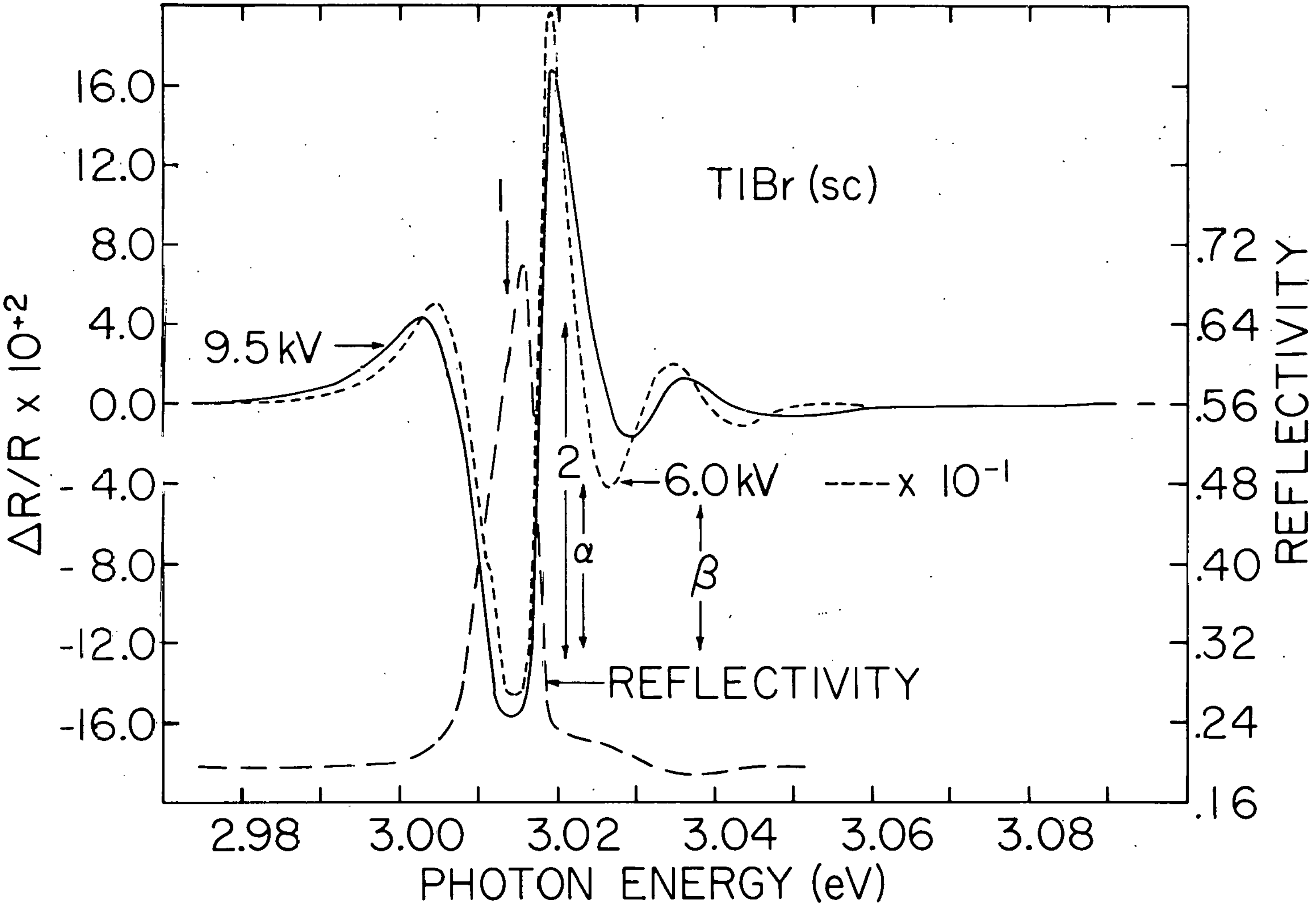

Figure 20. Calculated reflectivity (dashed line) and ΔR/R (dotted and solid lines) spectra of TlBr (sc)

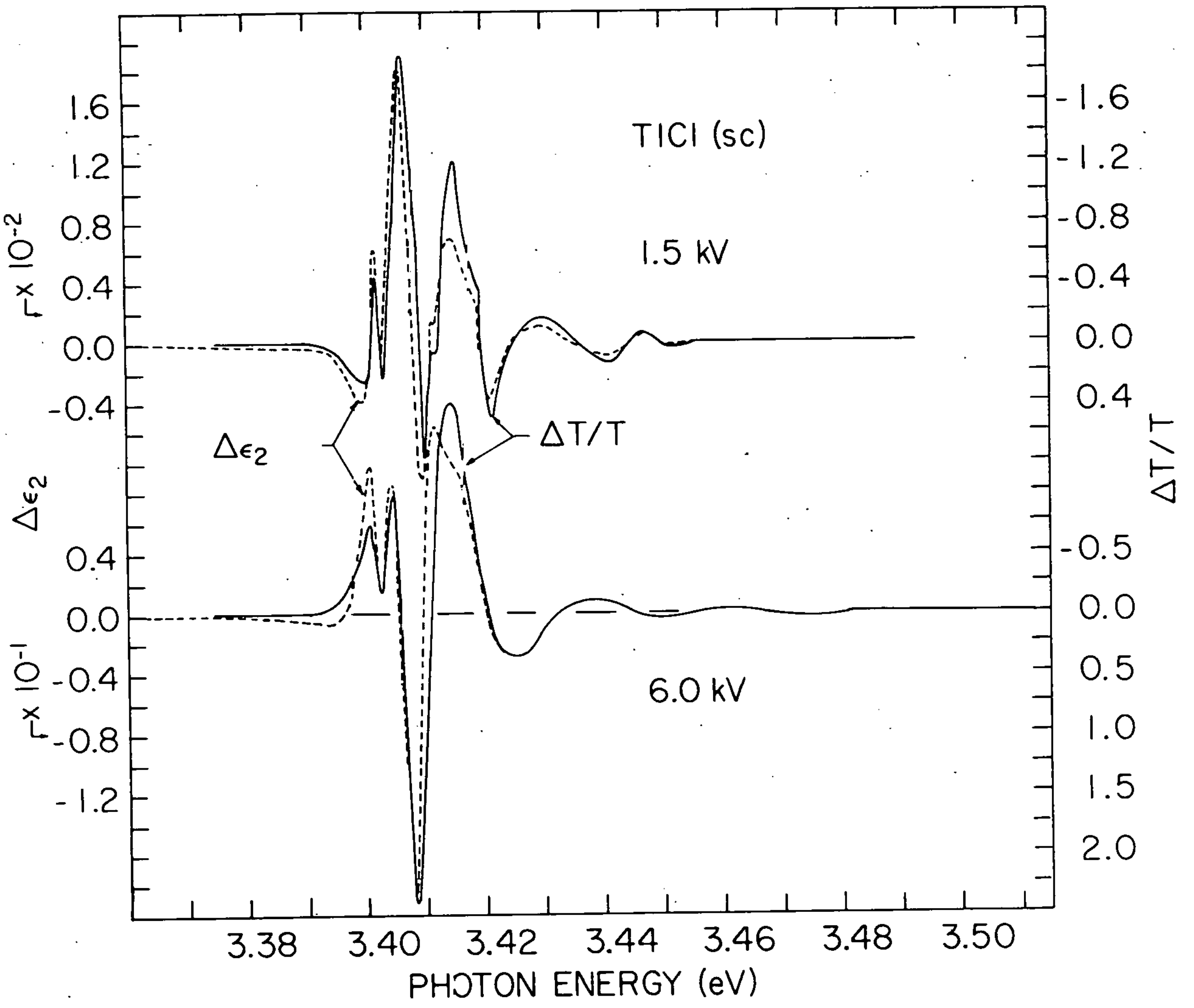

Figure 21. Measured ΔT/T spectra (solid lines) and calculated $\Delta\varepsilon_2$ spectra (dotted lines) of TlCl (sc)

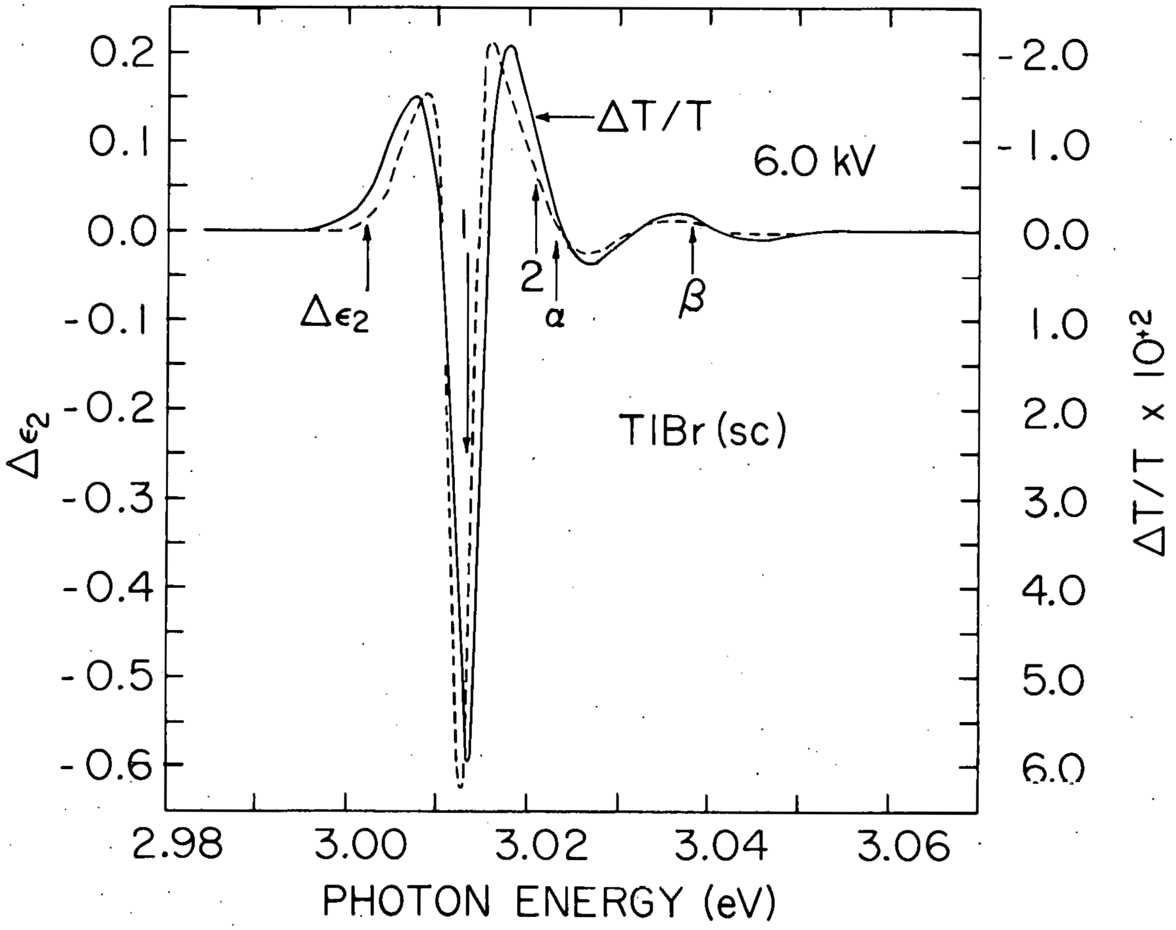

Figure 22. Measured ΔT/T spectrum (solid line) and calculated $\Delta\varepsilon_2$ spectrum (dotted line) of TlBr (sc)

peak positions and zero crossing points similar to the unmodulated spectra, but the relative peak heights are quite similar especially in the TlBr spectra.

Electroabsorption (EA) spectra

In Figures 23 and 24 the absorption and EA spectra are plotted for TlCl and TlBr for runs which were not reduced with the data reduction program. In the TlCl EA spectra of Figure 23, the 1', 1, 2', and 2 features are resolved, as they were in the earlier ΔT/T spectra at 1.5 kV. The 1' and 1 EA features are shifted noticeably to lower energy from the estimated energy of the 1' and 1 absorption peaks. This spectrum is not as broad as the earlier TlCl spectra and the 1' and 1 EA features may be more sensitive to shifting due to photocarrier effects and to superposition when the peaks are broadened by the electric field. The TlBr spectra in Figure 24 are similar to the earlier spectra but less highly broadened and shifted by strain. A higher level of photoconductivity is thought to be present in this sample because of the negative luminiscence peak at 3.0 eV. The 1.5 kV spectrum shows a structure between the α and β positions which is not predicted by the theory discussed in Chapter II. Figure 25 shows the behavior of the feature, labeled α_2, as a function of applied field from another TlBr run. The field dependence of the luminescence and the 1' feature are also shown in this figure.

Electromodulation signal as a function of temperature

Figure 26 shows the electromodulation signal as the sample temperature drifted from 5-6 K to above liquid nitrogen temperature. The

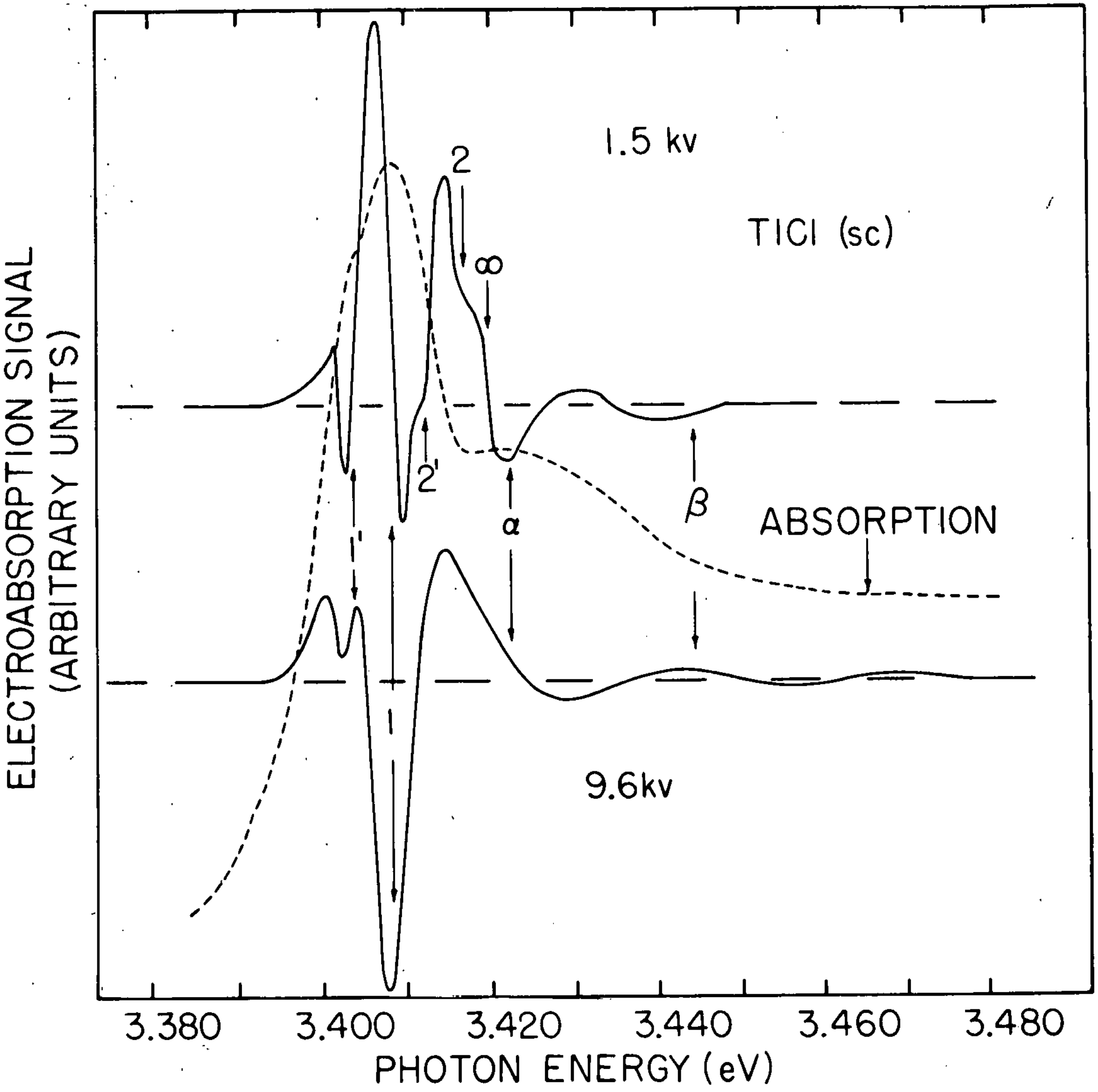

Figure 23. Absorption (dotted line) and EA (solid lines) spectra of TlCl (sc)

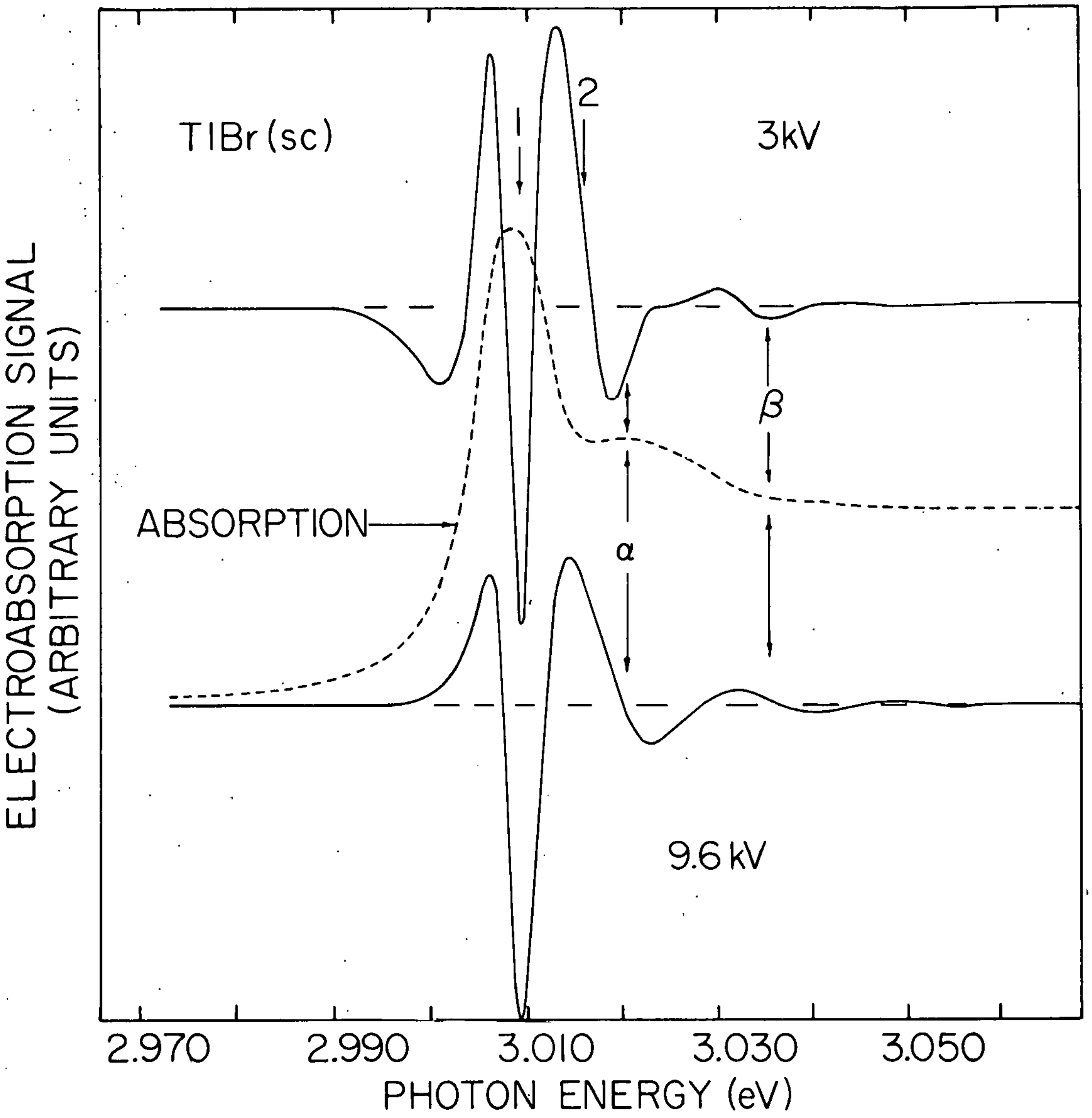

Figure 24. Absorption (dotted line) and EA (solid lines) spectra of TlBr (sc)

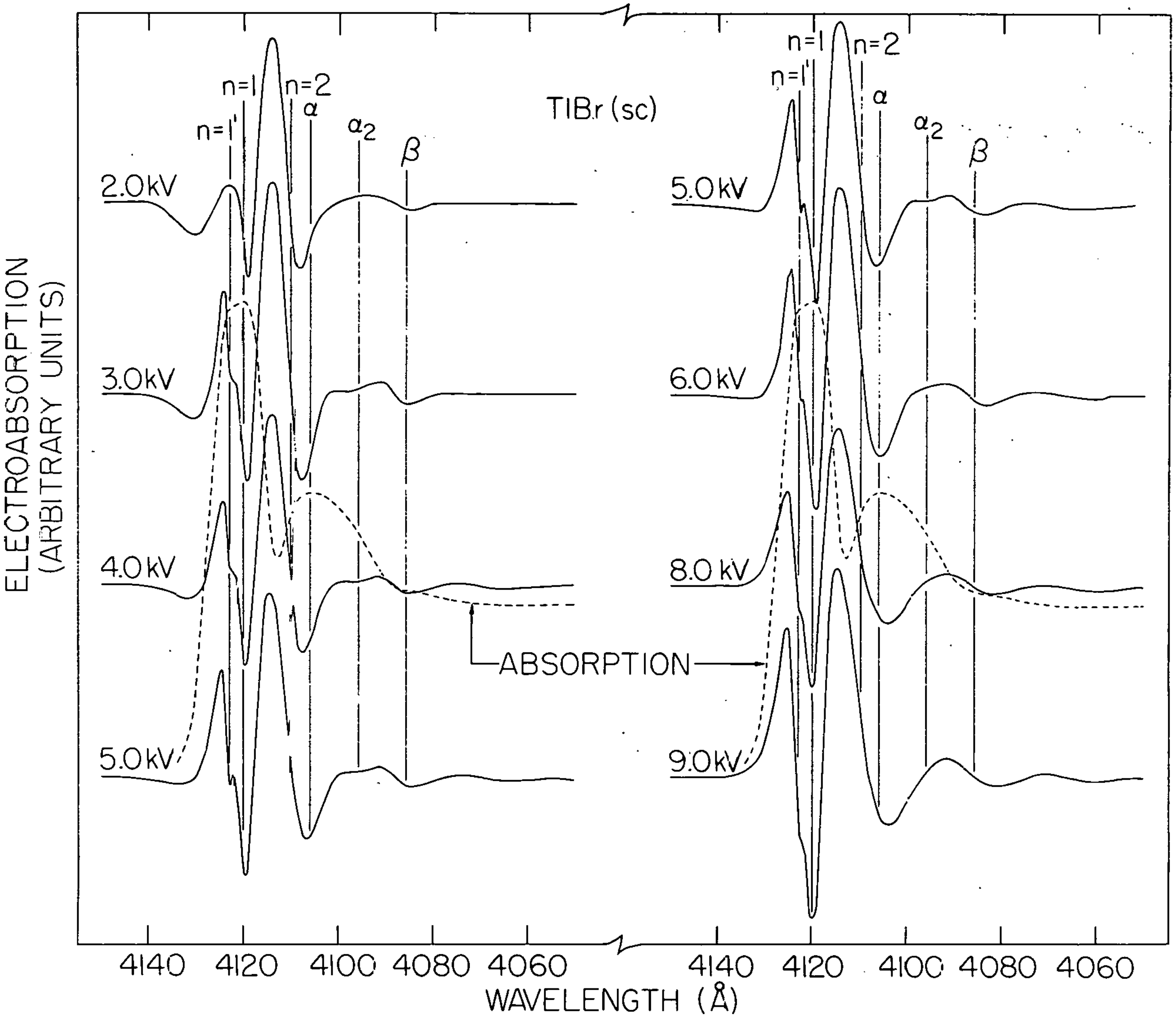

Figure 25. Absorption (dotted line) and EA (solid lines) for voltages from 2.0 to 9.0 kV

Figure 26. Eight scans of the electromodulation signal (arbitrary units) vs. photon energy as the sample temperature drifted from near liquid helium temperature in the upper left hand corner to above liquid nitrogen temperature in the lower right hand corner

THIS PAGE

WAS INTENTIONALLY

LEFT BLANK

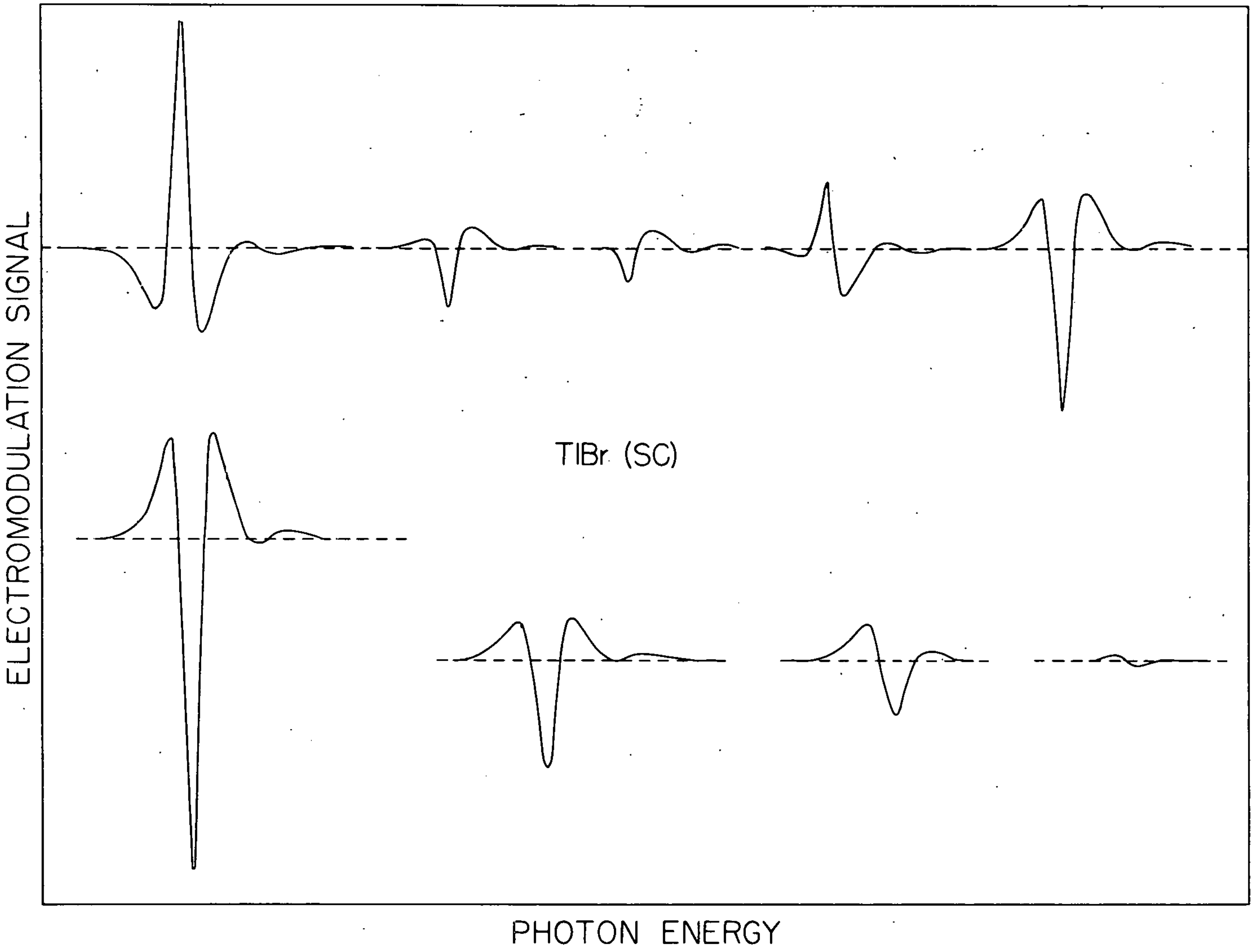
ELECTROMODULATION SIGNAL
TlBr (SC)
PHOTON ENERGY

spectrum in the upper left-hand corner was measured at 5-6 K before the liquid helium in the cryostat had evaporated. The spectrum was rescanned as the sample warmed and the resulting spectra are shown with sample temperature increasing for the spectra shown across the top of the figure from left to right and continuing in the same direction across the bottom. The two spectra (top and bottom) shown on the left side of the figure have an opposite polarity, which indicates a 180° phase shift in the signal. An explanation of this effect will be given in the next chapter in terms of photocarriers.

Abnormal (fcc) Phase Results for TlCl and TlBr

The abnormal (fcc) phase results consist of absorption and EA spectra for both compounds and calculated quantities obtained from the TlBr data, using the Wannier exciton model, as discussed in Chapter VI. The spectra of a TlBr doublet (sc and fcc) phase sample are included in this section.

Figures 27 and 28 show the absorption and EA spectra of TlCl and TlBr, respectively. The solid vertical lines designate the positions of structure identified in the absorption measurements of reference 27. The dotted vertical lines mark the locations of structure obtained from this investigation. The n=1 positions of reference 27 are not shown, due to the near-coincidence with the locations determined by this study for both TlCl and TlBr. The n=1 TlCl absorption peak is seen in Figure 27 to be narrower than the TlBr peak, which has a more prominent wing on the high energy side due to the higher exciton states. Above the n=1 peaks the α and β (not to be confused with the α and β phonon features in sc

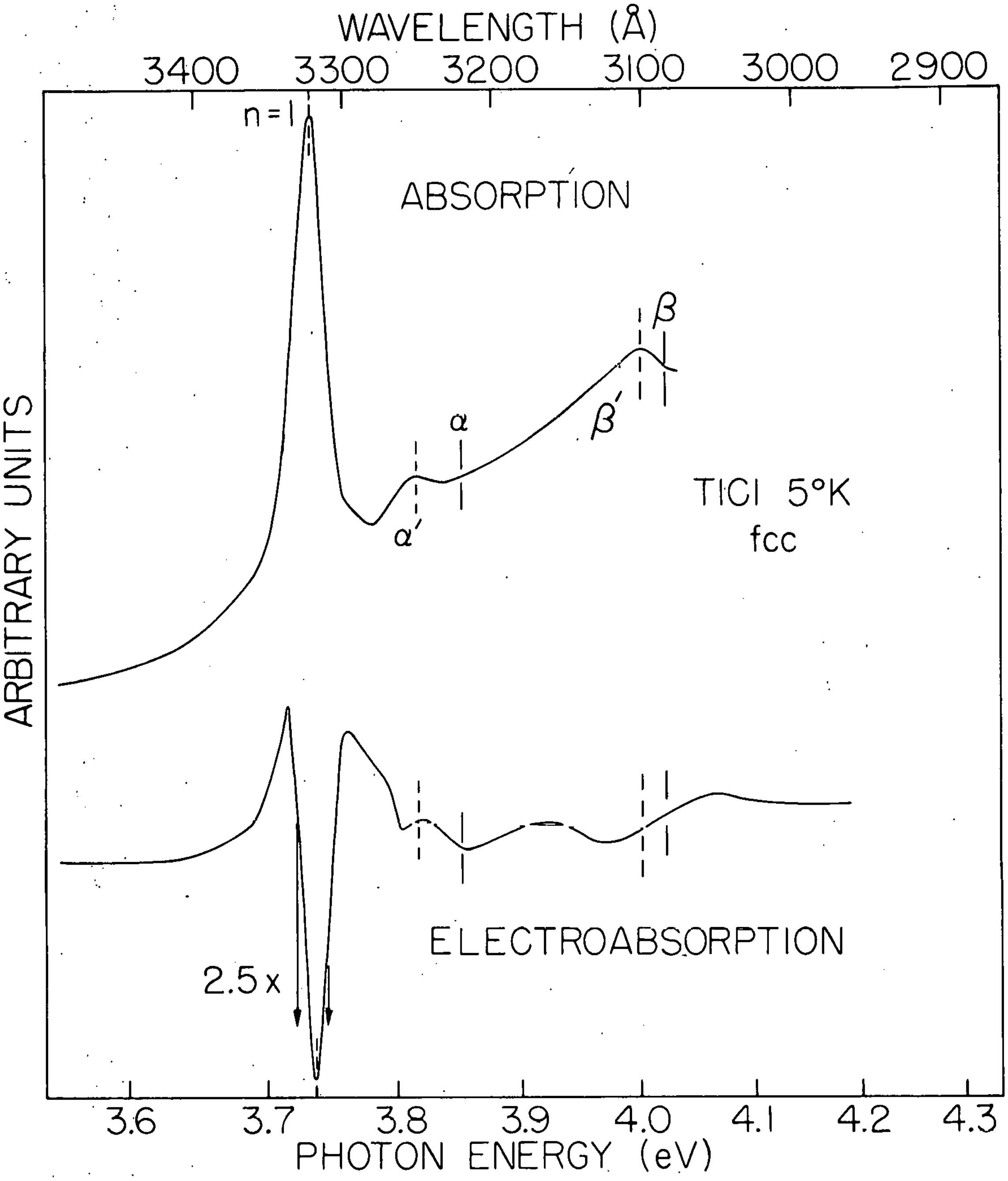

Figure 27. Absorption and EA spectra of TlCl (fcc)

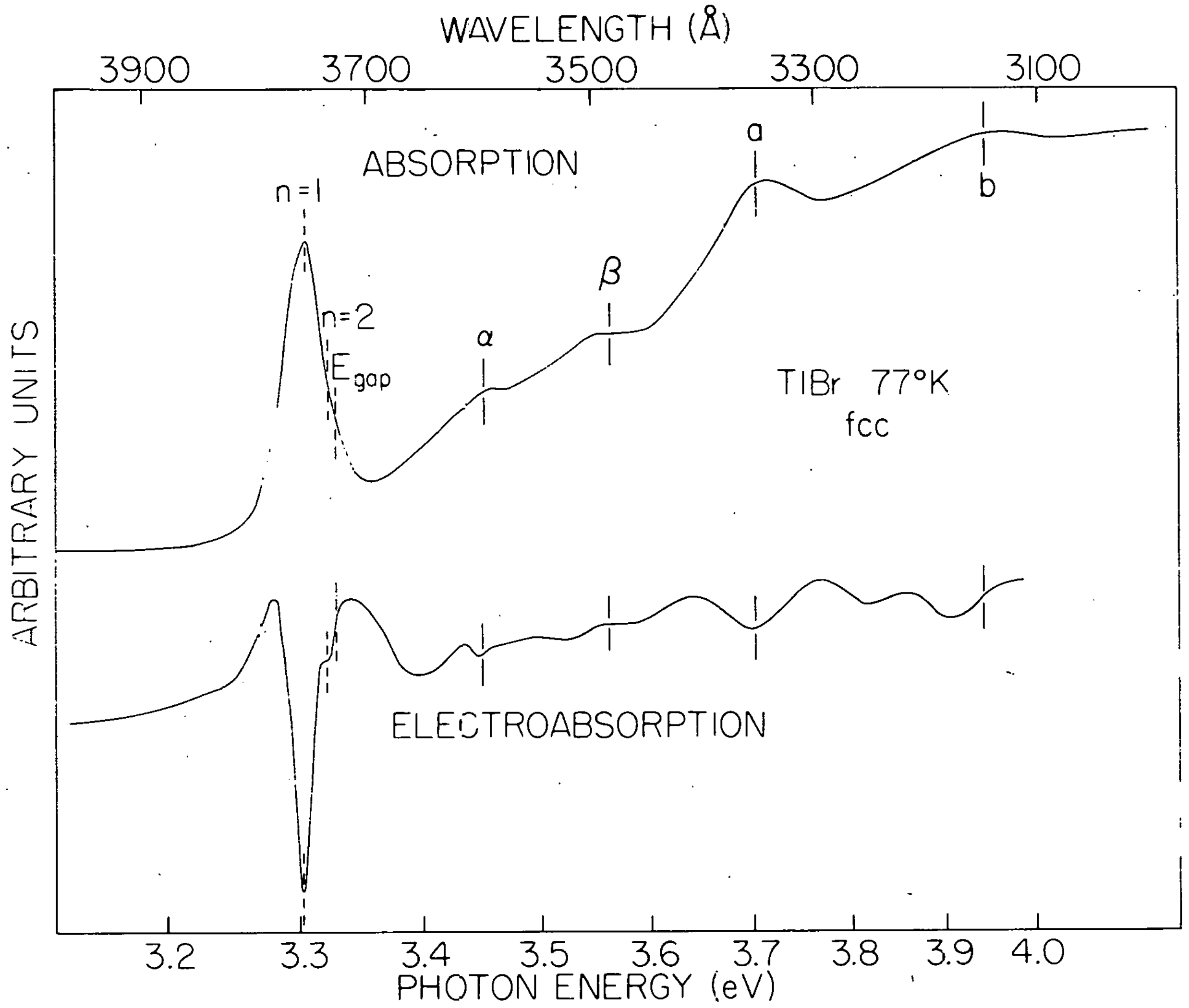

Figure 28. Absorption and EA spectra of TlBr (fcc)

spectra) locations of reference 27 are shown. The corresponding features in this study are marked α' and β' for TlCl and are shifted to lower energy. In TlBr they are in close agreement with the earlier measurement, as are the a and b features, which were out of the range of measurement for TlCl. Structure which may be analogous to the α and β features was observed in the spectra of the TlBr sample after its thickness had been increased to 700 Å. This caused a phase transition to the normal phase and broad, overlapping absorption peaks were observed above the n=1 exciton peak (3.02 eV) and the band gap (3.03 eV) at 3.04 and 3.06 eV.

The n=1 EA features in Figures 27 and 28 coincide with the energy positions of the absorption peaks, as expected for bound exciton states. In the TlBr spectra the feature at 3.321 eV has been assigned to the n=2 exciton state. It was not possible to resolve a similar feature in the TlCl spectra due probably to the signal-to-noise ratio. At higher energy the negative EA features corresponding to the α and β absorption peaks are shifted to lower energy and have an unusual line shape. In the TlCl spectra the absorption peaks are at 3.812 and 4.000 eV with the EA features at 3.803 and 3.975 eV. Similarly, in the TlBr spectra the absorption peaks are at 3.458 and 3.550 eV and the EA at 3.447 and 3.525 eV. The TlBr EA feature corresponding to a has the expected lineshape and position while the b feature is similar to the α and β structures.

Table 2 contains the quantities calculated from the n=1 and 2 photon energies obtained from the EA spectra and the band masses of reference 27, using the Wannier model with an uncorrected Coulomb potential as discussed in Chapter VI.

Table 2. Properties of fcc TlBr

	fcc TlBr
E_g(eV)	3.327
R(meV)	24.2
a_o(Å)	25.2
ε_o	11.8
$\mathcal{E}_I$(V/cm)	9.7×10^4

Figure 29 shows the absorption and EA spectra of a double-layer sc and fcc sample at 77 and 5 K. The spectra are broadened more than the single-layer spectra due to a higher level of strain but several interesting observations can still be made. The opposite sign for the temperature shift of the sc and fcc n=1 peak can be seen. The sc peak shifts approximately 12 meV to higher energy while the fcc peak shifts approximately 6 meV to lower energy when the sample temperature is raised from 5 to 77 K. The most significant aspect of the spectra, in terms of exciton effects, is the switch in the relative n=1 peak strengths of the two phases between the absorption and EA spectra. In absorption the fcc n=1 absorption is stronger but in EA the sc n=1 feature has the

Figure 29. Absorption and EA of a two layer sc and fcc TlBr sample

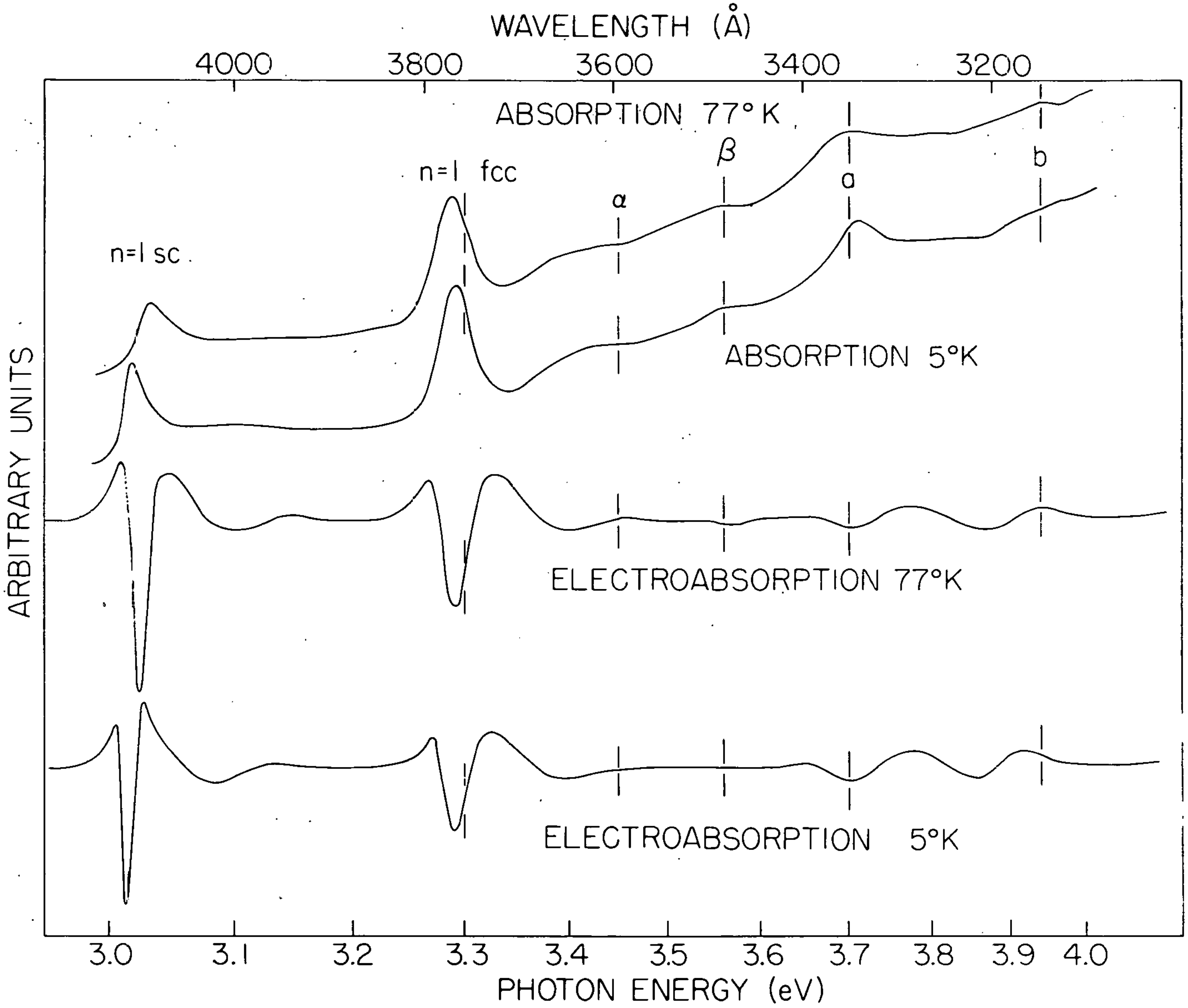
WAVELENGTH (Å)
4000
3800
3600
3400
3200
ABSORPTION 77° K
n=1 fcc
α
β
a
b
n=1 sc
ABSORPTION 5°K
ELECTROABSORPTION 77°K
ELECTROABSORPTION 5°K
ARBITRARY UNITS
3.0
3.1
3.2
3.3
3.4
3.5
3.6
3.7
3.8
3.9
4.0
PHOTON ENERGY (eV)

higher amplitude. This will be explained, in terms of the exciton parameters involved, in the next chapter.

CHAPTER VIII. DISCUSSION

Normal (SC) Phase Data

One of the primary objectives of this investigation was to compare measured electric field-induced changes in the complex dielectric function with the detailed predictions of Blossey's calculations.[11a,b] This has not been possible in the most ideal sense but some progress has been made in this direction. An ideal comparison has been hindered by aspects of the thallium halides which do not fit the Wannier exciton model used in Blossey's calculations (n=1 doublet structure and phonon sidebands), by photocarrier effects which prevent a well-defined electric field modulation, and by strain and thermal effect sensitivity which distort measurements due to unwanted perturbations on the exciton states. In addition, the reduction of the $\Delta T/T$ data to obtain $\Delta\varepsilon_1$ and $\Delta\varepsilon_2$ may have been influenced by the suspected inaccuracy of the values of ε_1 and ε_2 determined from the transmission measurements. The ε_1 and ε_2 values obtained from this study are not in close agreement with an earlier determination, since the earlier ε_2 values[81] for the n=1 peak are approximately half the values shown in Figures 12 and 13. However, it is not clear that the values of this study are in error to this extent since recent measurements[39] indicate that the earlier values are too low for TlCl. Obvious structure artifacts due to this inaccuracy appear to be minor in the derivative spectra, as in the case of the small shoulder seen in the 6.0 kV $\Delta\varepsilon_2$ TlCl spectra in Figure 17 between the positions marked 2' and 2.

Figure 30 shows the field-induced changes in ε_1 and ε_2 as a function of photon energy for the Wannier exciton model with peak heights and zero-crossing widths designated. Blossey calculated the dependence of these quantities on the applied field and these predictions will be compared with the measured field dependence. Before the comparisons could be made, an estimate of the level of spectral broadening involved was needed. The kT factor for the experimental spectra is approximately equal to 0.05 R, which is lower than the broadening of $\Gamma = kT = 0.2R$ used in Blossey's calculations, which gives an ε_2 lineshape and n=1 half width in best agreement with the experimental lineshape and ε_2 half width value of approximately 0.5 R for both compounds. A larger broadening in the experimental spectra, than would be expected from the thermal mechanism, is not unexpected, since a certain amount of inhomogeneous strain broadening was an unavoidable side effect of stabilizing the sample so that it would not be driven by the electric field, as discussed earlier. Table 3 gives a perspective on the compromise that had to be made to stabilize the sample in terms of the n=1 strain shift. The membrane/thallium halide frame sample yields a nearly-intrinsic spectrum and is a good reference for both the shifting due to strain and the half width. An increase in the half width of the n=1 peak strongly degrades the resolution of higher states, since the exciton binding energy is only approximately 10 meV. The shifting due to the membrane/CsI substrate is substantially less than for the KBr and quartz substrates. Half widths for the latter substrates are not useful for comparison due to the large distortion in the spectra.

Figure 30. Designations for peak heights and zero crossing separations of the electromodulated complex dielectric function, $\Delta\varepsilon_1 + i\Delta\varepsilon_2$, as a function of photon energy

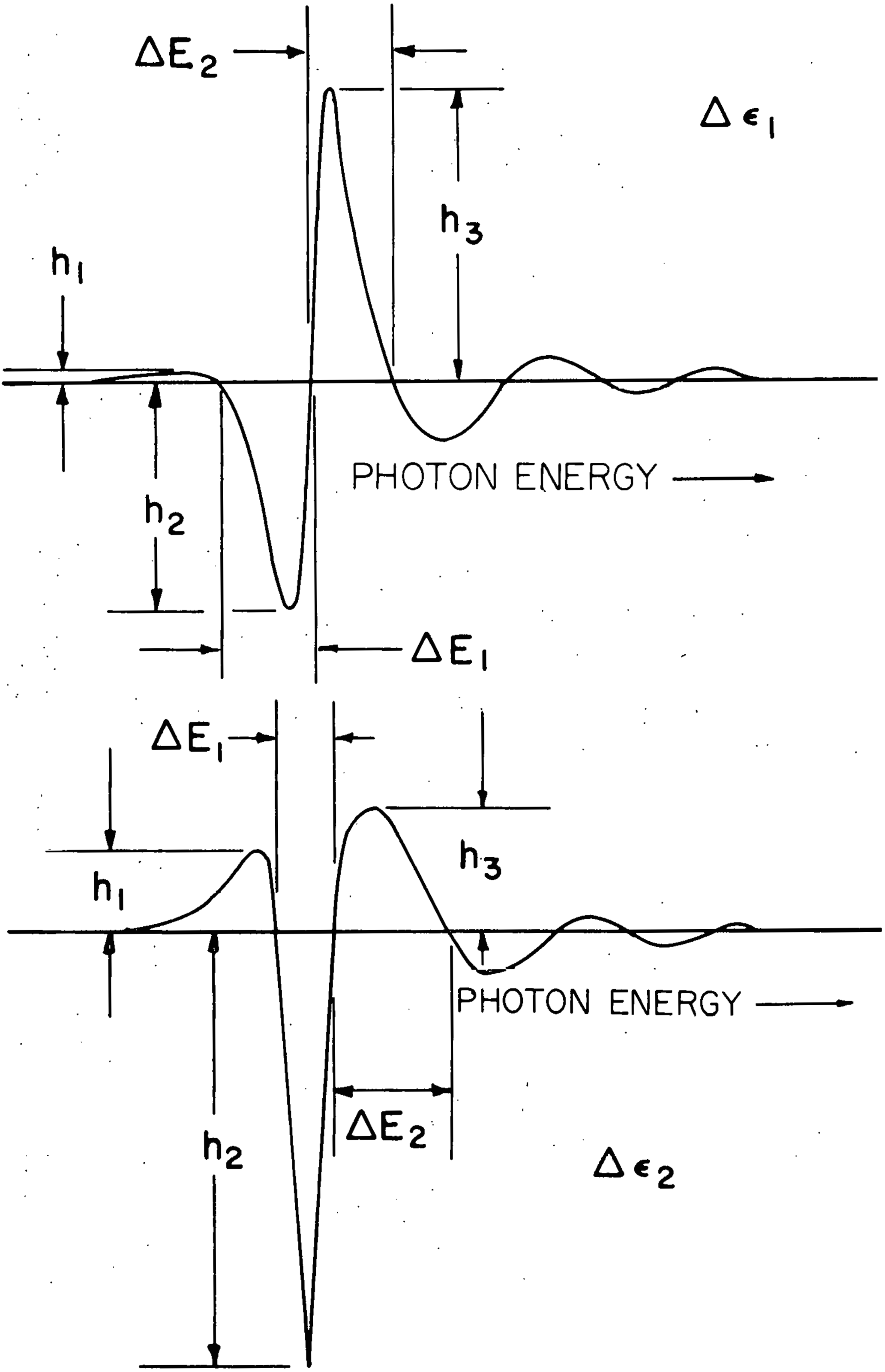
ΔE_2
$\Delta \epsilon_1$
h_3
h_1
h_2
PHOTON ENERGY
ΔE_1
ΔE_1
h_3
h_1
PHOTON ENERGY
ΔE_2
h_2
$\Delta \epsilon_2$

Table 3. Strain shifts near liquid helium temperature in the n=1 peak position for TlCl and TlBr evaporated on various substrates relative to the peak position for a membrane/thallium halide frame substrate. The n=1 transmission half widths are given for the membrane substrates. Units are meV

Substrate	TlCl Shift	TlCl Half Width	TlBr Shift	TlBr Half Width
membrane/frame[a]	0	8	0	5
membrane/CsI[b]	5	13	3	8
KBr[c]	20		8	
Quartz[c]	31		18	

[a] Reference 10.

[b] This study.

[c] Reference 81.

It was decided to use the results of Blossey for the $\Delta\varepsilon_1$ and $\Delta\varepsilon_2$ spectra, calculated with the $\Gamma = 0.2$ R broadening value, for comparison with the measurements even though the experimental broadening is mainly due to strain rather than thermal mechanisms. The first comparison is of ΔE_2 for $\Delta\varepsilon_2$, identified in Figure 30, as a function of applied field, $\mathcal{E}$.

The dependence is shown in Figure 31, plotted as $\Delta E_2/R$ vs $\mathcal{E}/\mathcal{E}_I$ for TlCl and TlBr, with the electric field determined from the voltage across the plates and their separations, without a local field correction for polarization, since the Bohr radius of the exciton is a factor of ten larger than the lattice constant. Above 6.0 kV the experimental lines (solid lines) have slopes close to the calculated line (dashed line). At voltages below 6.0 kV the slope of the experimental lines is approximately half of what is expected from theory. This plot indicates from the viewpoint of the theory that either (1) the field seen by the exciton is considerably less than that calculated from the voltage and that the field increases too slowly with applied voltage below 6.0 kV or (2) the $\Delta\varepsilon_2$ values are distorted.

The disagreement between the calculation and the measurements seen in Figure 31 is thought to be primarily due to photocarrier effects. Several other observations suggest that the field seen by the exciton is due to the superposition of the applied field and the field of the photocarrier charge distribution. Hence argument (1) is favored. Since the electromodulation measurements of this study were not designed to measure the very sample-dependent photocarrier and trapping effects in the thin film samples, some aspects, such as the origin of the photocarriers, can only be tentatively suggested. The photocarriers in the exciton region are thought to be generated both by indirect band to band transitions and by trapping of either the electrons or holes of excitons, thus freeing the opposite charges for conduction. Carrier multiplication may occur due to impact ionization by field-accelerated photocarriers.

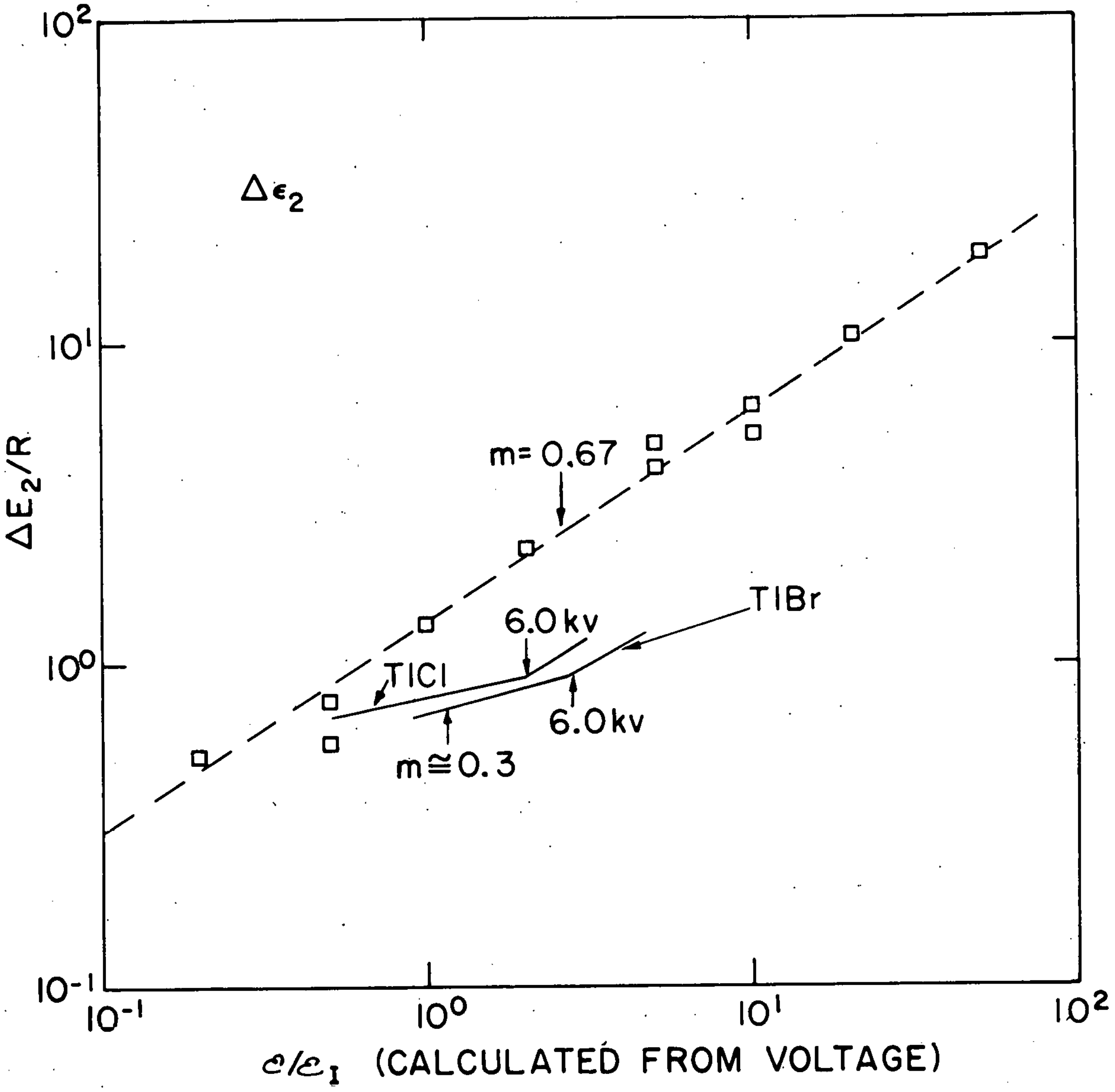

Figure 31. Plot of $\Delta E_2/R$ vs. $\mathcal{E}/\mathcal{E}_I$ with the dashed line fit to theory (□) and the solid lines to experiment with the applied field calculated from the plate gap and voltage

The first evidence of photocarriers to be discussed supports the suggestion that they are mobile and hence could distribute to form a field opposing the applied field. The positive (negative) peak on the low energy side of the $\Delta T/T$ (EA) spectra is thought to be due to impact luminescence caused by radiative de-excitation of electrons or holes excited by collisions with field accelerated photocarriers and not by electromodulation of the luminescence from the de-excitation of states excited by photon absorption due to the sign of the peak.[75] Hence this feature is not due to modulation of the beam transmission but to light generation within the sample, which is in phase with the modulation field and detected by the photomultiplier. The impact luminescence appears in the $\Delta T/T$ (EA) spectra as a spurious, enhanced transmission (attenuated absorption) as indicated by the positive (negative) peak. The transmission (absorption) is known to be attenuated (enhanced) in this region by the applied field because the field broadening of the n=1 peak has the result of increasing the absorption. The impact luminescence peak is sample- and field-dependent and can be seen clearly at low fields in Figures 13, 24 and 25 with the latter showing the field dependence of the feature (the negative peak at 4130 Å). The disappearance of the feature at high fields may indicate that the impact luminescence is not excited as efficiently by more highly accelerated carriers or that the luminescence signal does not grow with field as fast as the EA signal. In Figure 25, the 9.0 kV spectrum amplitude is attenuated by approximately a factor of 30 relative to the 2.0 kV spectrum in Figure 25 and the intermediate spectra amplitudes are reduced by smaller amounts to fit into the figure.

If the negative n=1 peak of the 9.0 kV EA spectrum of Figure 25 is compared with the corresponding feature in the 9.6 kV spectrum of Figure 24 the former peak appears strongly attenuated relative to the latter. This is thought to be due to a large reduction in the field due to a very high photoconductivity for the n=1 photon energy region in the former sample. In thicker samples, the n=1 peak actually was cut off completely, although the sample transmission had not cut off and modulation could occur if a sufficiently strong field was present. The better-ordered crystalline structure of the thicker films may allow substantial carrier multiplication by impact ionization of the large density of n=1 excitons being created in this photon region, thus supplying sufficient carriers for a dynamic screening effect. Samples used in the measurements were made with thicknesses below approximately 700 Å to reduce the distortion of the applied field by photocarriers.

A similar strong photocarrier effect has been identified, but perhaps not fully recognized, by other workers in electroreflectance measurements[46] on TlCl and TlBr single crystals. These workers have discussed a severe photocarrier effect which, at very low temperatures (1.8 K), has prevented detection of any signal throughout the exciton region in TlCl. By increasing the temperature (20 K) and reducing the incident beam intensity, they have obtained a spectrum above the n=1 region, but do not observe the expected strong negative peak in the n=1 region. Examination of my calculated electroreflectance, ΔR/R, for TlCl explains the probable cause of the missing structure. In Figure 19, at a low field (1.5 kV spectrum), the negative peak near the position marked 1 is just beginning to form. At 6.0 kV in Figure 19 and 6.0 and 9.5 kV in Figure 20, the peak is seen easily. On this basis it seems very likely that the absence of the expected n=1 structure in the electroreflectance measurements is due to a strong reduction by photocarriers in the field seen by the excitons in this photon energy region and to the larger field required to modulate the n=1 state relative to the less closely bound higher energy states. Before leaving the spectra of Figures 19 and 20 it should be pointed out that while the calculated reflectivities have an unusual structure in comparison with experimental measurements,[46] they are qualitatively similar to reflectivity calculated from transmission data on TlBr by other workers.[81] The general form of the ΔR/R spectra is similar to data on ZnO[84] which has an absorption spectrum[85] like those of the thallium halides. For this reason it is not unreasonable to assume that the spectra are qualitatively valid even with some distortion introduced by the reflectivity.

The behavior of photocarriers in modifying the applied field in the single crystal and thick film samples is thought to be different from the thinner films of this study. In the more disordered thin films the photocarrier response is influenced by the lower carrier mobility and a higher density of traps, allowing less carrier multiplication by impact ionization. These properties, and the limitation on photocarrier generation due to the incident beam intensity, indicate that photocarriers may contribute an essentially static field which is superimposed on the applied field. Evidence of such a static field, which is also not strongly photon energy dependent, is given in Figure 26. The figure consists of eight scans of the exciton region as the sample warmed from 5-6 K to above liquid nitrogen temperature with the spectra undergoing a 180° phase shift before being washed out by thermal broadening in the lower right-hand corner. The upper and lower spectra on the left side of the figure show little distortion but are shifted in phase by 180 degrees and the shift can be explained in terms of the photocarrier field which is larger for the lower spectrum due to an increase in the photocarrier response with temperature in this region.[86] The phase shift is explained by the waveforms in Figure 32 which are for three levels of photocarrier response. The response is dependent on various factors, including sample temperature, sample depth, incident photon energy, and film structure which, are important in terms of trapping centers that may themselves be modulated by the high electric fields applied. The applied field waveform is shown at the top of the figure with the photocarrier field waveform below which is caused by photocarriers generated in the illuminated region of the sample being swept by the applied field into the dark region where they are trapped. The distribution of positive (holes) and negative (electrons) charges that results provides a field that opposes the applied field. It is thought to be primarily a static field with a small AC component due to new charges being swept up by the field and the decay of the field by recombination and the collapsing separation of the positive and negative charges when the applied field is off. It is interesting to note that, in terms of this picture of the field, the photocarrier field would appear to have saturated in

Figure 32. Schematic of waveforms which contribute to the electromodulation of excitons in the presence of photocarriers in thin film samples. The exciton is not sensitive to the direction of the field and hence senses the absolute value of the total field waveform function

THIS PAGE

WAS INTENTIONALLY

LEFT BLANK

TIME DEVELOPMENT OF THE ELECTRIC FIELD

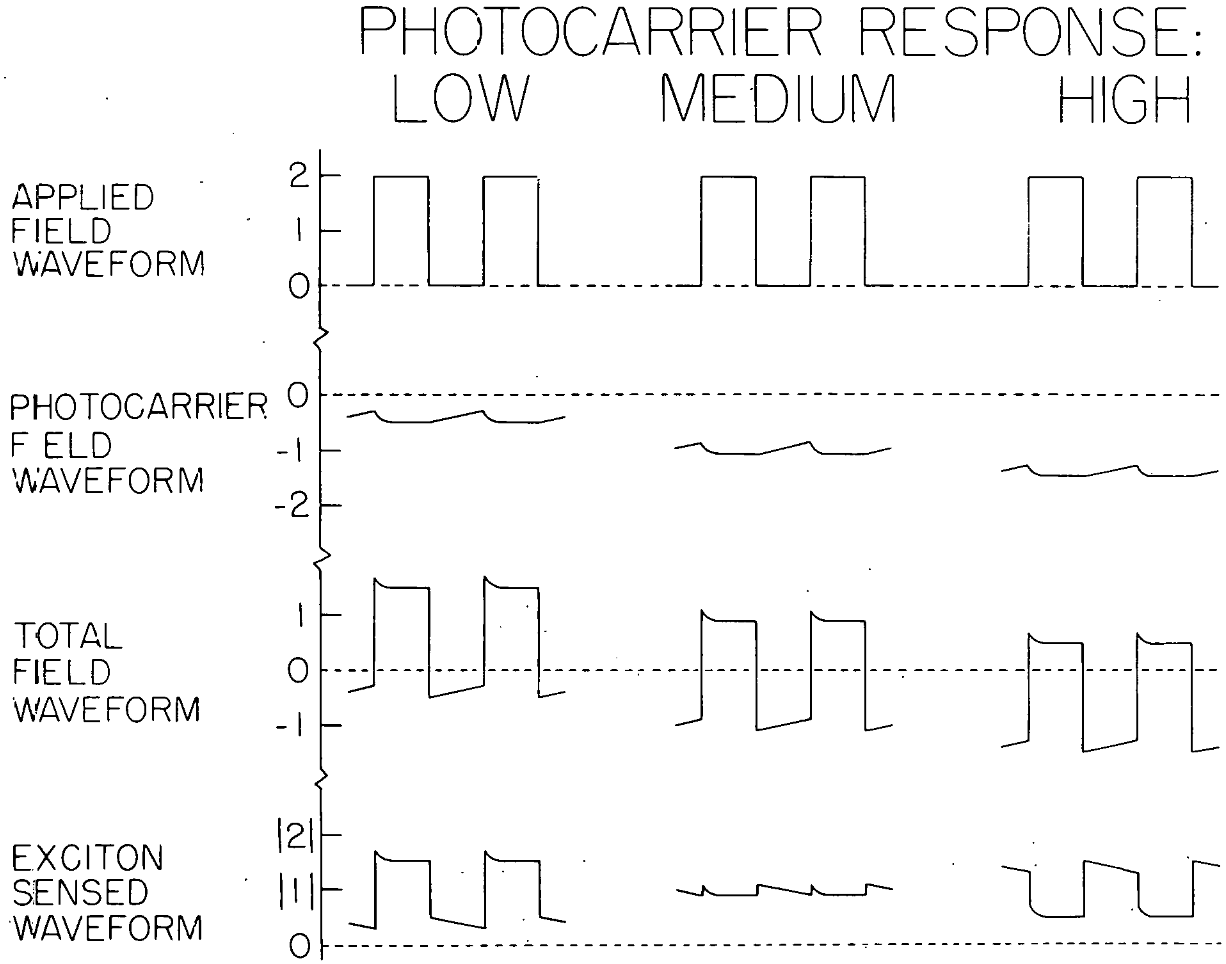

Figure 31 at the positions marked by 6.0 kV for both TlCl and TlBr at the temperature of 5-6 K.

The total field waveforms shown in Figure 32 are the sum of the two waveforms above and differ only in DC components for different responses. The exciton-sensed waveform functions are the absolute value of the total waveform functions because the exciton is not sensitive to the direction of the field. The low response exciton waveform amplitude is attenuated relative to the applied field and shifted in phase (less than 90°) when detected by the lock-in due to the square wave distortion, and both of these aspects have been observed in the measurements. The waveform indicates that the light transmission is being modulated between two nonzero values of applied field. This explains why some of the electromodulation spectra have slight shifts in their peak positions relative to transmission and $\Delta T/T$ spectra at different fields as for example in Figure 23 for the n=1' and 1 peaks.

The medium response waveform shows how the AC modulation field can be nearly cancelled by photocarriers, even though the carriers do not screen in a dynamic sense. This condition is approximately shown by the highly attenuated spectrum in the middle of the upper part of Figure 26.

The high photocarrier response exciton waveform, shown in Figure 32, has a 180° phase shift relative to the applied waveform and is proposed as the mechanism to explain the 180 degree shift in the electromodulation signal shown in Figure 26. When photocarrier fields of this magnitude exist, some field inhomogeneity is expected across the illuminated region of the sample due to the approximate line charge distribution of photocarriers. If the line charges form in the dark region, well separated from the illuminated region, the inhomogeneity will not be as serious in modulating the transmission and this may be the case in the lower spectra on the left-hand side of Figure 26 which shows little distortion.

In view of the difficulty in determining the field on the exciton from the voltage and plate separation, it was decided to calibrate the field for each spectrum from the theoretical curve of $\Delta E_2/R$ for $\Delta\varepsilon_2$ shown in Figure 33 thus allowing a test of the internal consistency of the calculation. This curve was chosen, because it is independent of broadening and the ΔE_2 separation is less sensitive to aspects of the thallium halides not consistent with the model used in the calculation. The method of calibration has the added benefit of giving the field in terms of $\mathcal{E}_I$ which is needed to compare the other peak heights and zero-crossing separations to the calculation. Had it been necessary to calculate $\mathcal{E}_I$ from Equation 13, another source of error would have been introduced because accurate values of a_o do not exist.

The experimental zero-crossing separations for $\Delta\varepsilon_2$ and $\Delta\varepsilon_1$ are shown in Figures 34, 35 and 36 for TlCl and TlBr with the solid lines calculated by Blossey. Unfortunately, the calculations did not go to as low fields as the measurements, but could be extended with some confidence to lower fields, since they appear to be nearly linear in this range, although the lines have not been extended in the figures. Figure 34 shows that the $\Delta\varepsilon_2$ high field TlBr experimental values for ΔE_1 are in good agreement with theory while the TlCl values are somewhat low, possibly due to a decrease in the $\Delta\varepsilon_1$ separation by the larger splitting

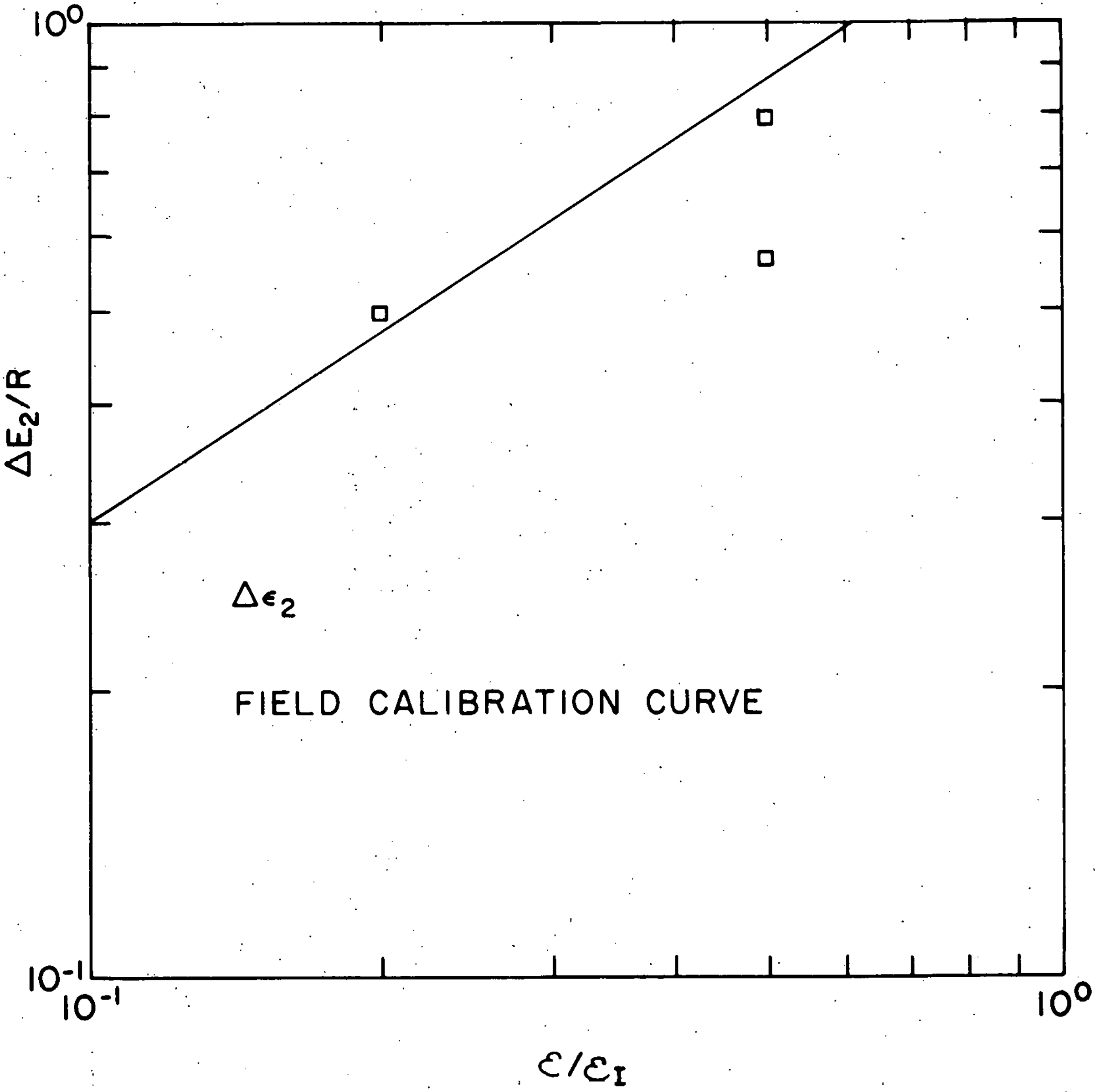

Figure 33. Theoretical $\Delta E_2/R$ versus $\mathcal{E}/\mathcal{E}_I$ plot used to calibrate the modulation field from the TlCl and TlBr experimental ΔE_2 values for various voltages applied to sample capacitor. The theoretical line and points shown are from Figure 31

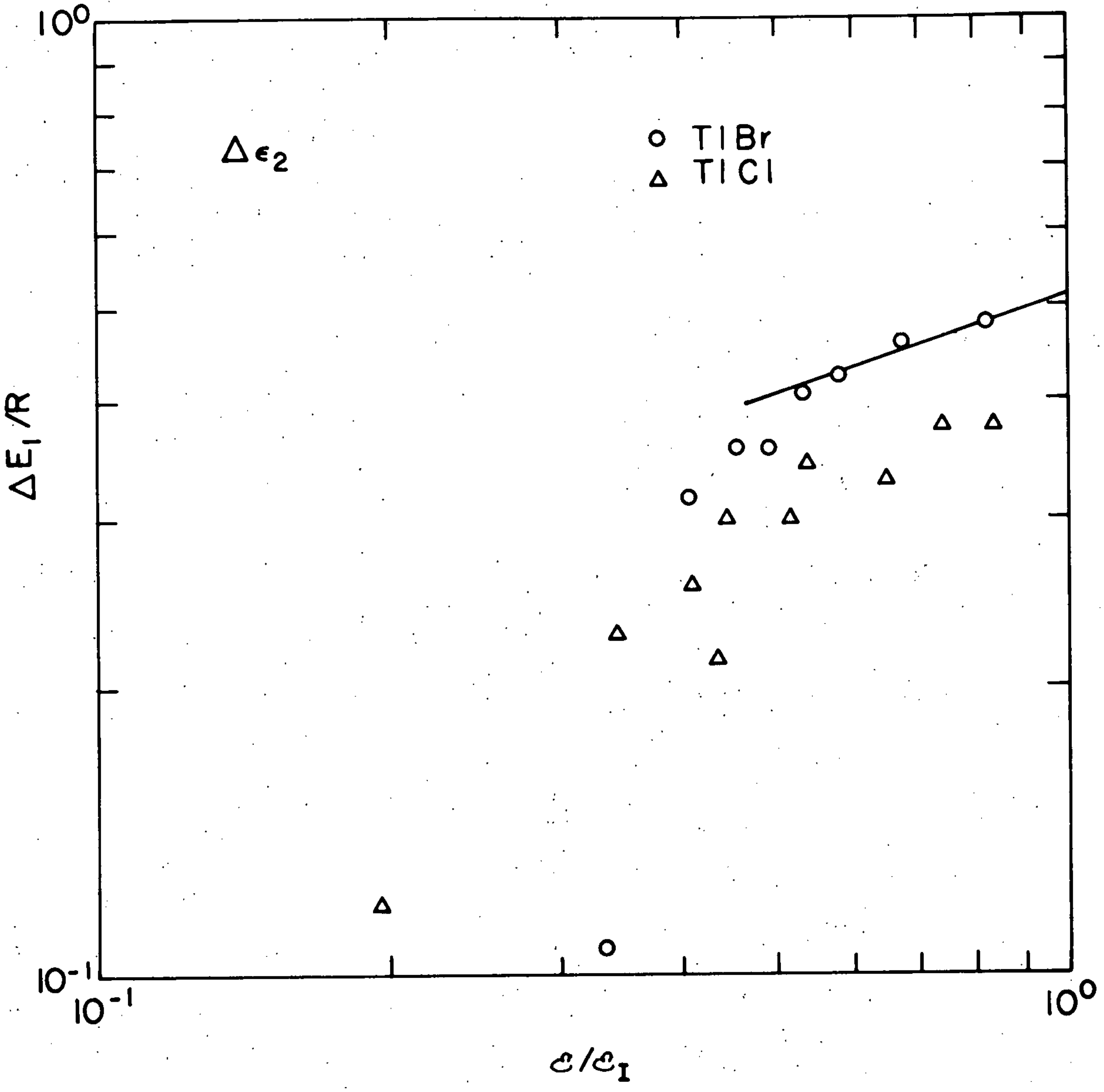

Figure 34. Experimental values of ΔE_1 compared to theory (solid line) for $\Delta\epsilon_2$ after field calibration for TlCl and TlBr

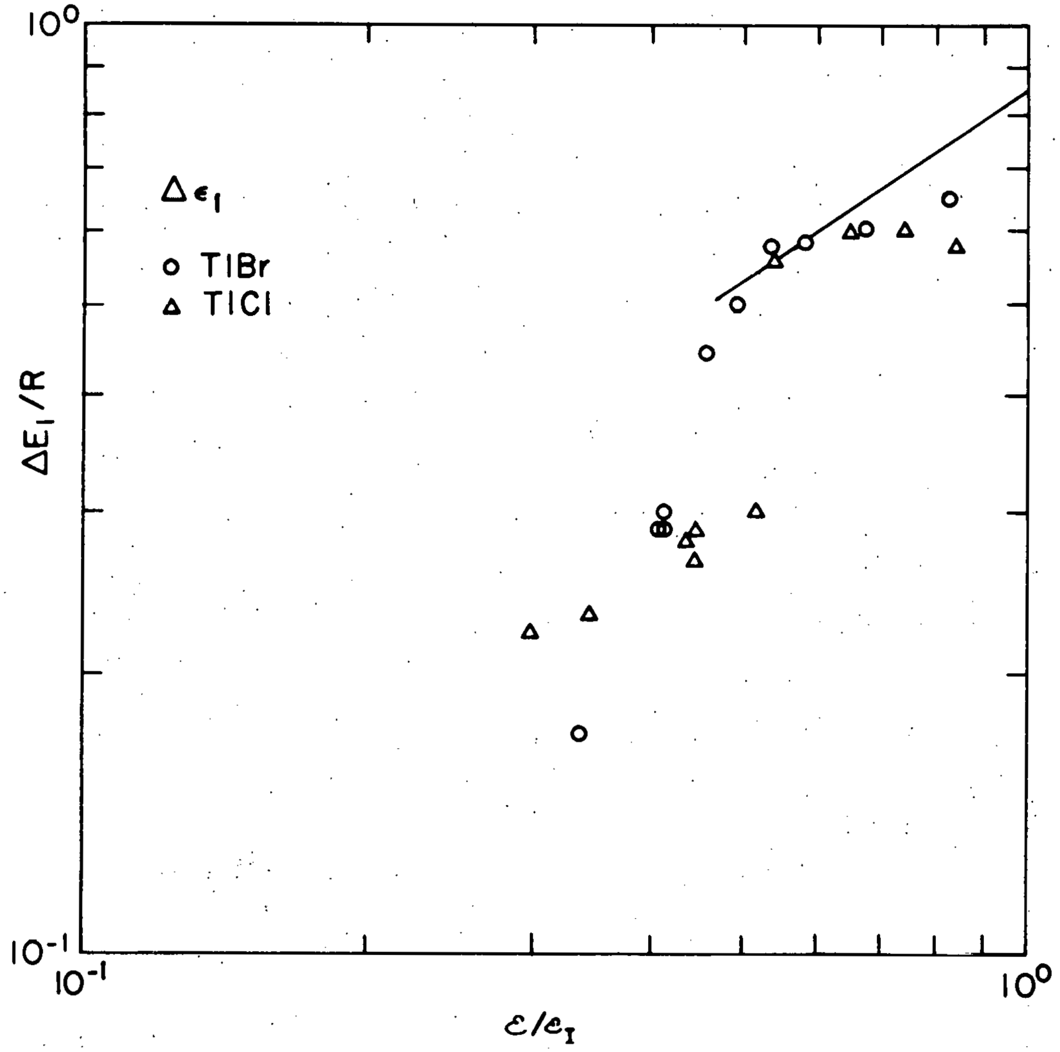

Figure 35. Experimental values of ΔE_1 compared to theory (solid line) for $\Delta\varepsilon_1$ after field calibration for TlCl and TlBr

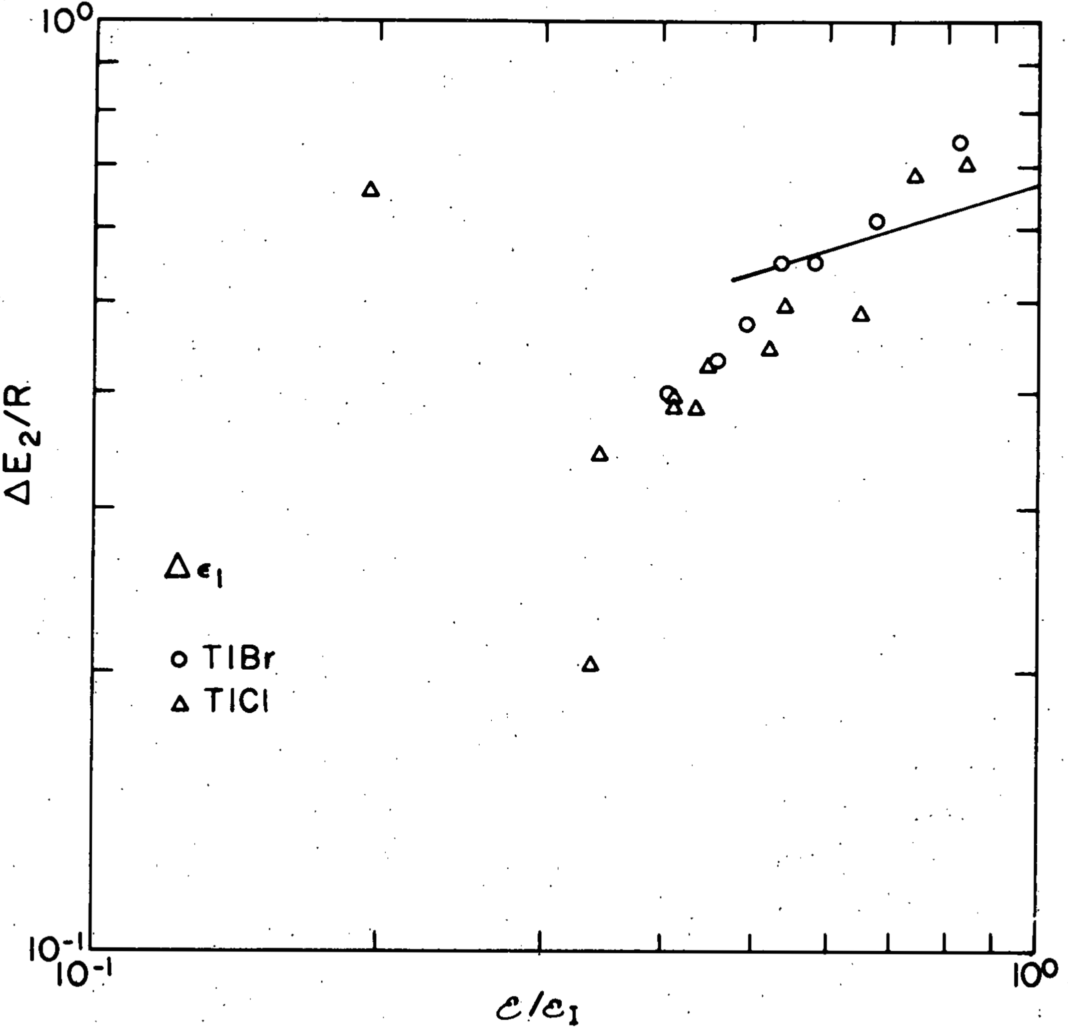

Figure 36. Experimental values of ΔE_2 compared to theory (solid line) for $\Delta\varepsilon_1$ after field calibration for TlCl and TlBr

of the exciton as seen in the 1' and 2' features of Figures 13 and 17. As the field decreases, the $\Delta E_1/R$, values are increasingly low and this may be due to a growing sensitivity of the ΔE_1 separation to the splitting, which is apparent in the low field spectra of Figure 17 when compared to the higher field structure. The ΔE_1 and ΔE_2 values of $\Delta\varepsilon_1$, shown in Figures 35 and 36, show a similar trend when compared to theory, in that agreement is rather good at high fields but deteriorates at lower fields. The scatter of the high field experimental zero crossing values for both $\Delta\varepsilon_1$ and $\Delta\varepsilon_2$ can be compared to the scatter of the $\Delta E_2/R$ of $\Delta\varepsilon_2$ theoretical values shown in Figures 31 and 33 and appears to be fairly similar.

Before comparing the experimental peak heights to theory it was necessary to scale the experimental values. The calculated h_3 of $\Delta\varepsilon_2$ peak heights were used, since they are most closely associated with the ΔE_2 of $\Delta\varepsilon_2$ separation which was used for the field calibration. Figure 37 shows the calibration curve which was extended from $\mathcal{E} = 0.5\mathcal{E}_I$ to lower fields using a drafting curve so that the lower field peak heights could be scaled. Figures 38 and 39 show the h_1 and h_2 of $\Delta\varepsilon_2$ peak heights compared to theory. The experimental points are high for h_1 possibly due to a lower photocarrier response in this region where the absorption is low. It is interesting to note that the expected reductions in the h_1 height due to the n=1 splitting and to luminescence are not dominant in determining the peak height. The h_2 experimental points are in good agreement at high fields but only fair at lower fields due probably to both photon energy dependent photoconductivity and to static strain broadening which is of less significance at higher fields.

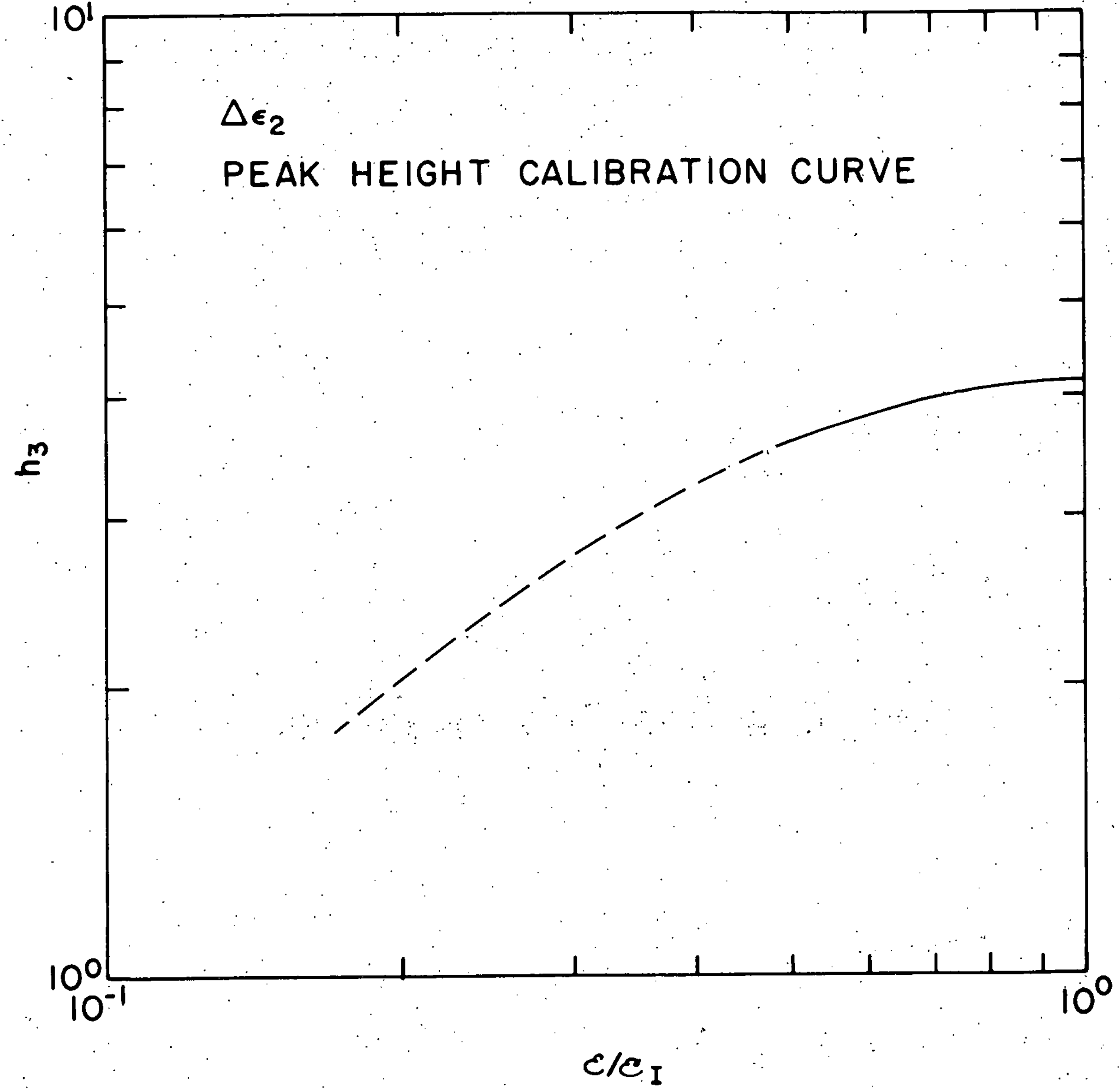

Figure 37. Theoretical curve used for scaling the peak heights for $\Delta\varepsilon_2$ and $\Delta\varepsilon_1$ from the TlCl and TlBr h_3 experimental $\Delta\varepsilon_2$ peak heights

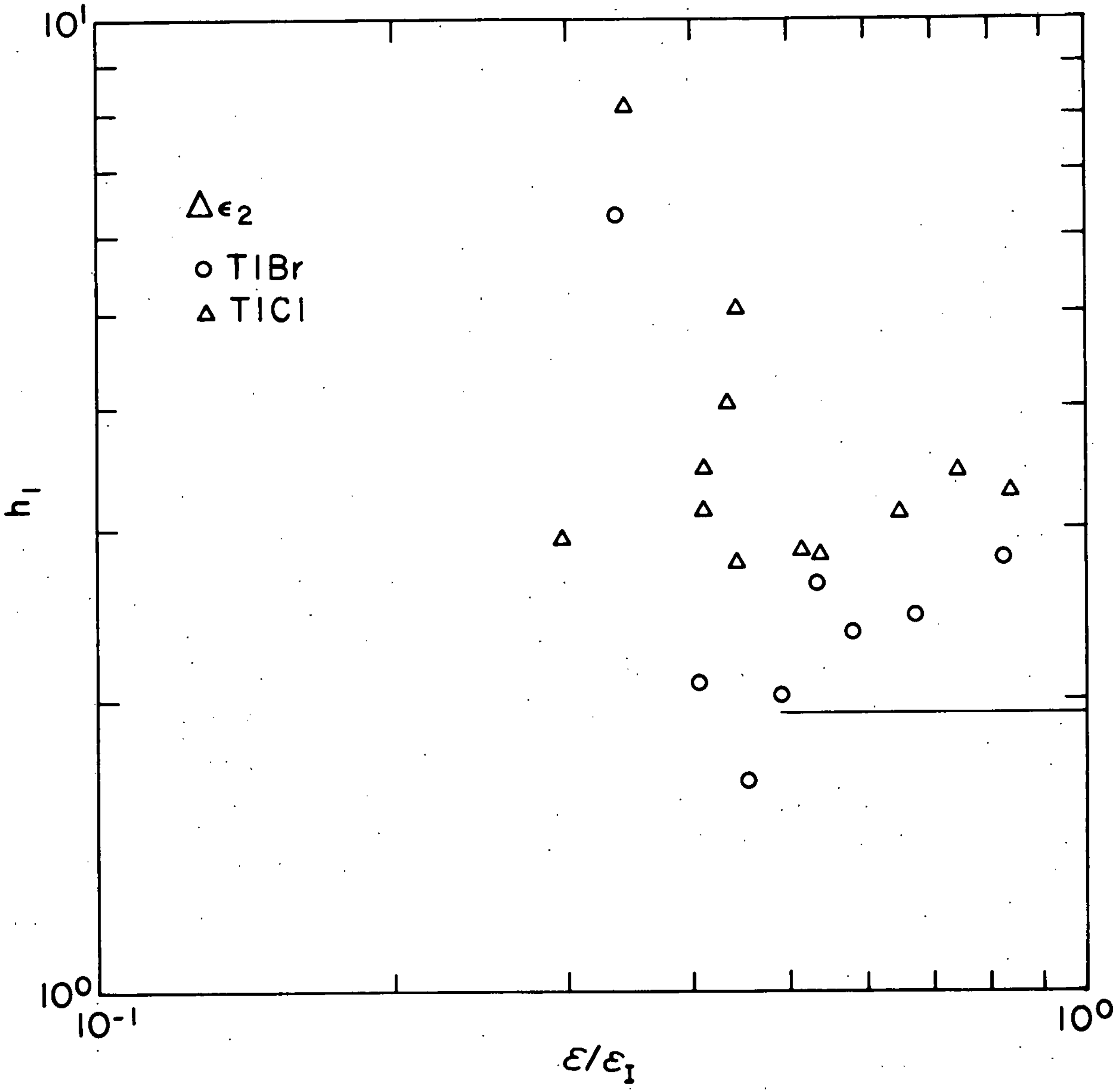

Figure 38. Experimental values of h_1 compared to theory (solid line) for $\Delta\varepsilon_2$ after field calibration and peak height scaling for TlCl and TlBr

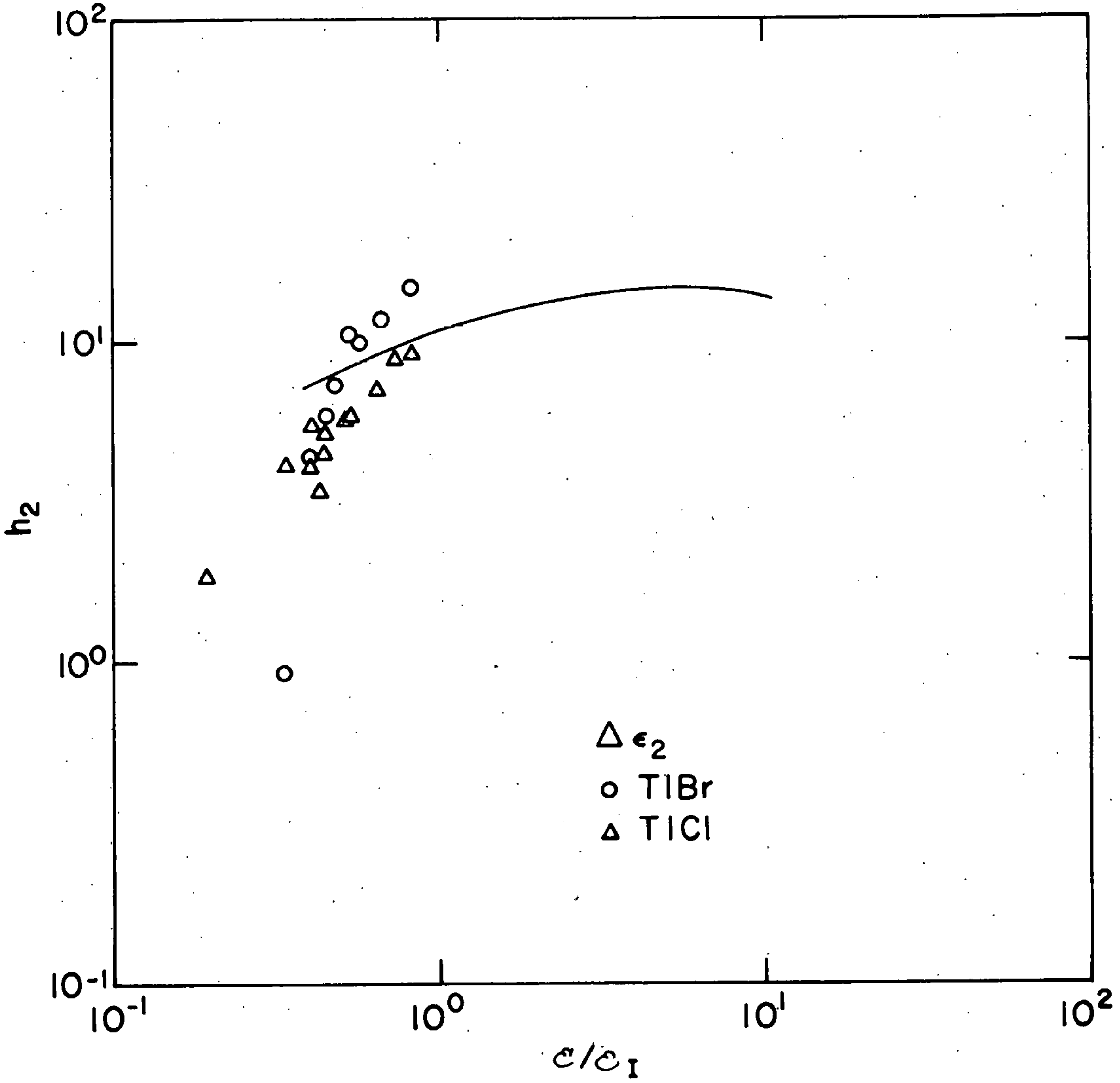

Figure 39. Experimental values of h_2 compared to theory (solid line) for $\Delta\varepsilon_2$ after field calibration and peak height scaling for TlCl and TlBr

Figures 40-42 show the experimental values h_1, h_2, and h_3 of $\Delta\varepsilon_1$, compared to the calculations for these quantities. Figure 40 shows that the h_1 values are too high as was the case for the $\Delta\varepsilon_2$ h_1 values. The experimental points for h_2 and h_3 are scattered more about the theoretical lines than the $\Delta\varepsilon_2$ values of h_2 but do not show the trend to diverge from theory at low fields.

The deviation from theory of the field-induced changes in the dielectric function is not indicative of defects in Blossey's calculation, which assumes no modification of the applied field by photocarriers or spectral distortion due to static strain. It appears that photocarrier effects and static strain, especially at low fields, are the principal causes for the deviation. Static strain is thought to play a more important role at low fields through inhomogeneous strain broadening because the electric field broadening is not as dominant as at high fields. Only a small part of the deviation is believed to be due to distortion of the spectra by the intrinsic exciton splitting and phonon sideband effects, and to inaccuracy in the dielectric function values used in the data reduction.

The electromodulation spectra show two interesting features which are not in the scope of Blossey's calculation. The assignments for these features are tentative, since they have not been investigated in detail. Figures 13 and 23 show a feature marked 2' in the 1.5 kV spectra of TlCl, which is thought to be possibly due to the splitting of the n=2 exciton state. Both the n=1 and n=2 states appear in the spectra to be split by approximately 5 meV. If the splitting is primarily due to the

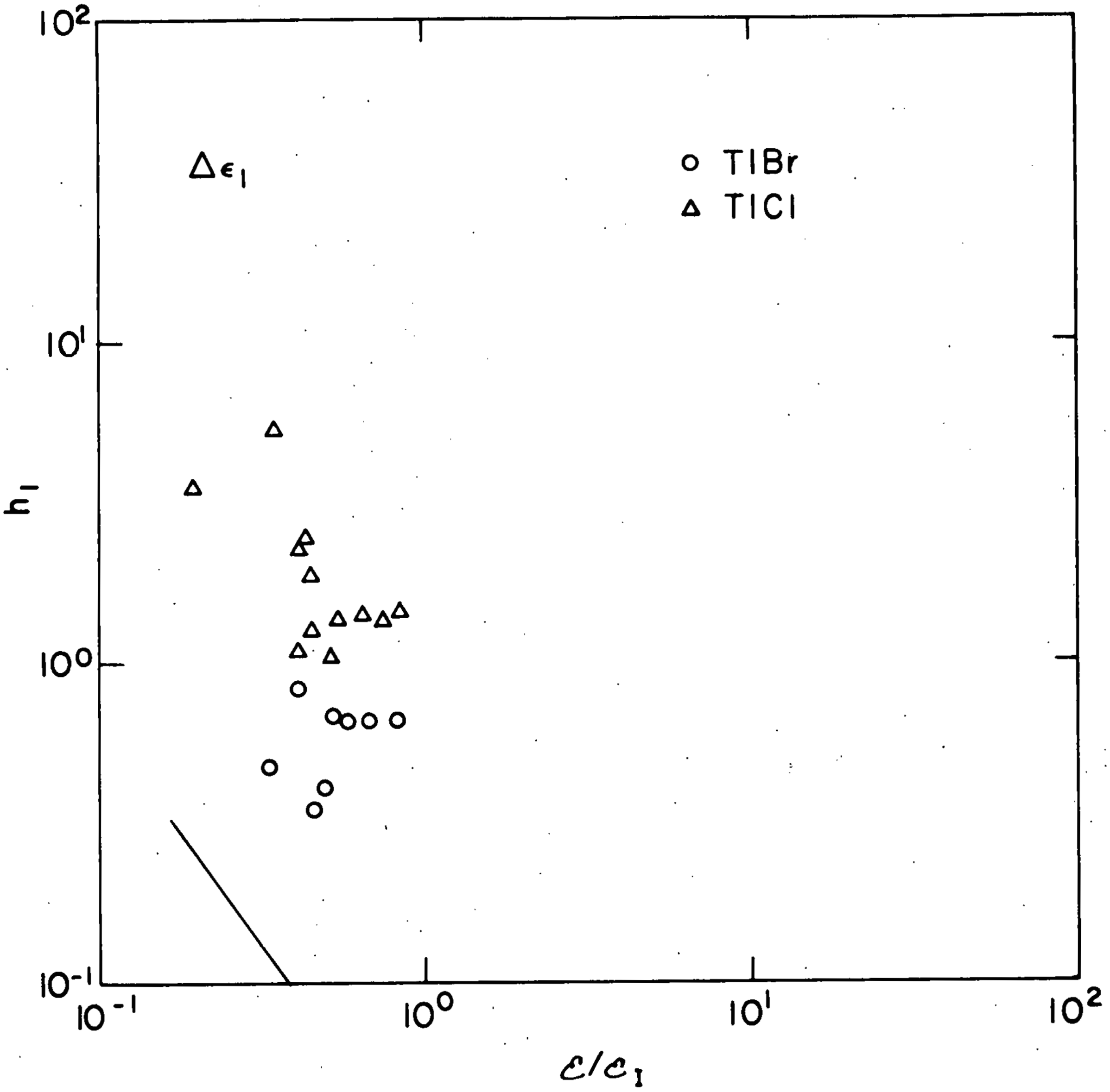

Figure 40. Experimental values of h_1 compared to theory (solid line) for $\Delta\varepsilon_1$ after field calibration and peak height scaling for TlCl and TlBr

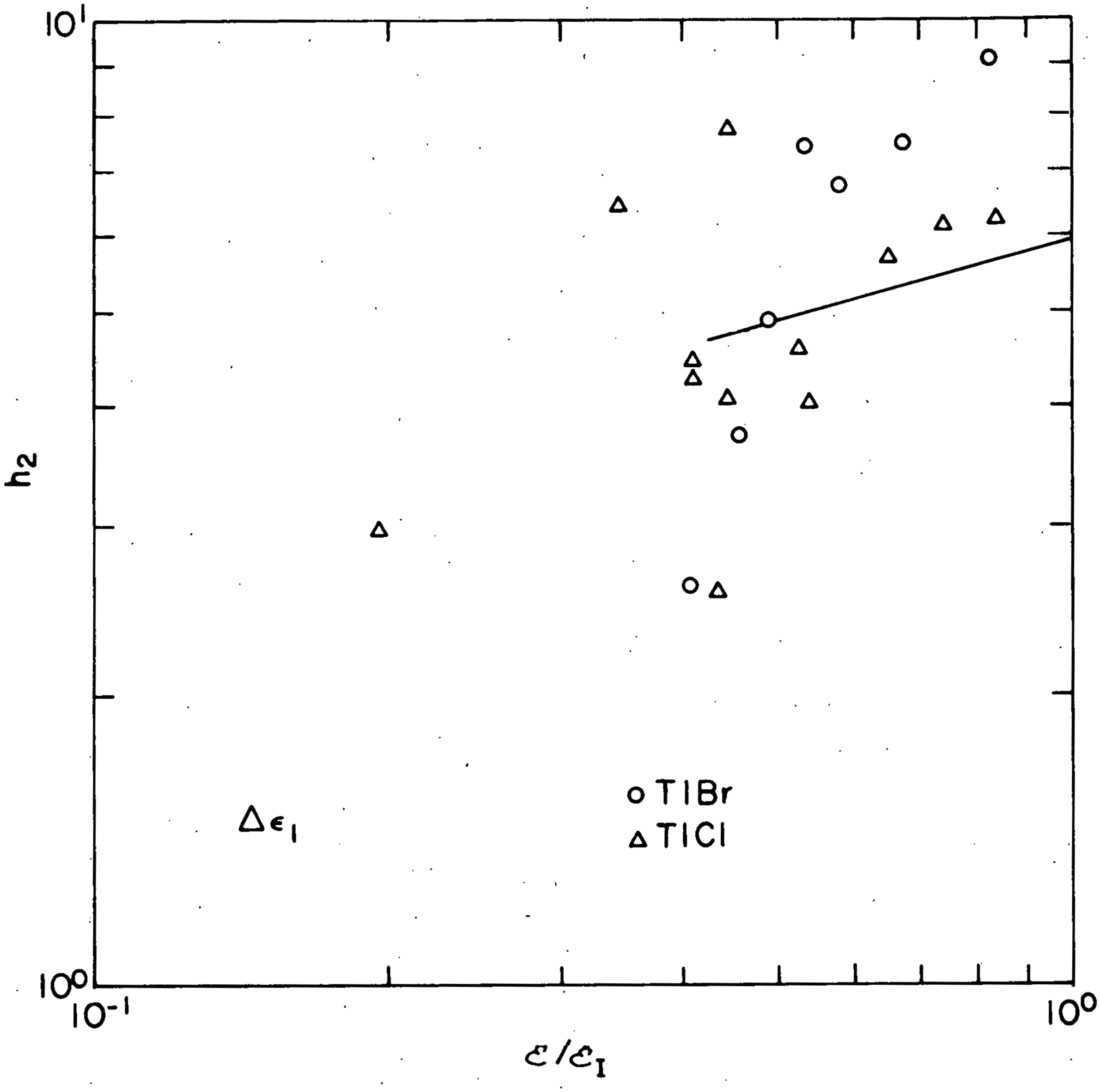

Figure 41. Experimental values of h_2 compared to theory (solid line) for $\Delta\varepsilon_1$ after field calibration and peak height scaling for TlCl and TlBr

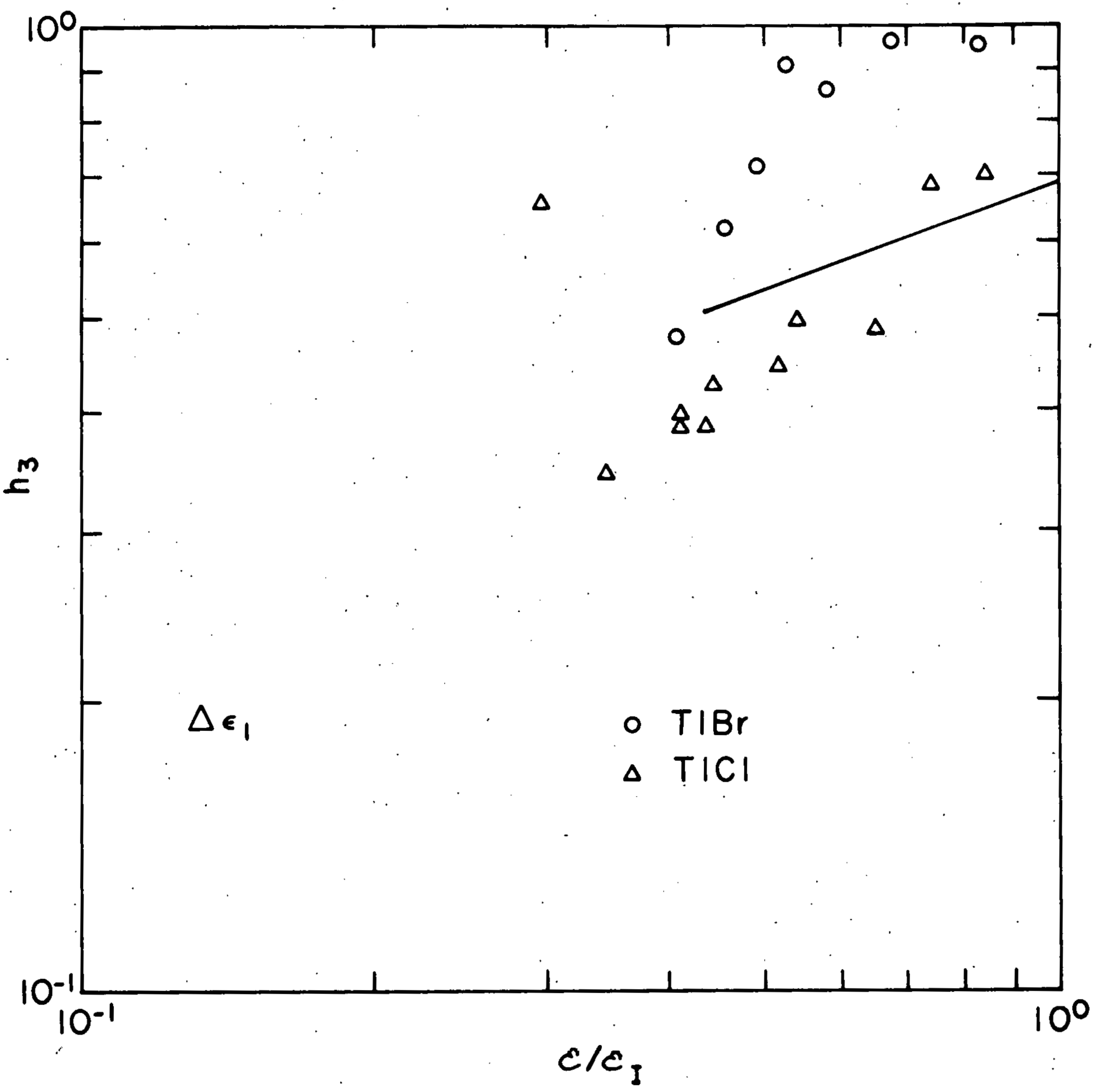

Figure 42. Experimental values of h_3 compared to theory (solid line) for $\Delta\varepsilon_1$ after field calibration and peak height scaling for TlCl and TlBr

exchange interaction, the equal splitting would not be expected because the n=2 exciton radius is a factor of 4 larger than the n=1 radius. The equal splitting would also not be expected for the Coulomb interaction, hence the assignment of this feature should be subjected to further investigation.

The second feature is marked α_2 in Figure 25 and coincides with the expected energy position for the n=2 exciton-phonon quasibound state in TlBr. Again the assignment of this feature is not well established, but it is interesting to note the difference in the field-sensitivity of this feature relative to that of the exciton. The n=2 exciton feature, if it were resolved, would be expected to wash out due to ionization at approximately 2.0 kV, but the α_2 feature is seen to persist until 8.0 kV.

Abnormal (fcc) Phase Data

The fcc TlBr band gap energy, E_g, and exciton binding energy, R, in Table 2 were calculated from the n=1 and n=2 exciton EA peak energies using the Wannier model, with no correction to the Coulomb potential, as discussed in Chapter VI. The value obtained for R and the calculated band masses[27] were then used to obtain a_o, ε_o, and $\mathcal{E}_I$. The fcc phase exciton is expected to be less Wannier like than the sc phase exciton due to a smaller predicted Bohr radius and larger lattice constant.[27] The sc phase is useful for comparison with the fcc phase, since energies have been determined for the sc n=1, 2, and 3 levels[10] and an approximate onset of Wannier behavior (energy levels fit a hydrogenic series) happens to occur with the n=2 energy in the normal phase. Such an onset of

Wannier behavior is expected with increasing n, since the orbit of the nth state is proportional to n^2 and the Wannier model becomes valid when the inequality, exciton radius >> lattice constant, is satisfied. Often this occurs at a value of n where states cannot be resolved but in sc TlBr it was possible to resolve n=1, 2, and 3 quite accurately with a magnetic field perturbation.[10] Hence the normal phase supplies states which can be used to calculate quantities similar to the fcc results that will have errors due to deviation from the Wannier model (using n=1 and 2 energies) and quantities that will be closer to what would be expected with a better fit of the model to reality which the Wannier model does in this case for n=2 and 3.

Table 4 is useful for discussing the fcc TlBr results. The first two columns contain quantities calculated from the n=1 and n=2 energies for both phases using band masses from Reference 27. The fcc results are from Table 2. The third column contains the Wannier limit values for the sc quantities and the fourth and fifth columns are calculated estimates using a corrected potential.[27,50]

The fcc E_g value determined with the n=1 and 2 energies is an upper bound for the actual band gap due to deviation from the Wannier model. Values of E_g calculated from simultaneous equations generated from Equation (29) will approach the actual value in the limit of the ideal Wannier model. The upper bound aspect can be demonstrated with the n=1, 2, and 3 energies of the normal phase data which give band gaps of 3.0203 eV and 3.0198 eV using the n=1 and 2, and n=2 and 3 energies, respectively, in Equation (29). The 3.0198 eV value is usually taken as

Table 4. Properties of TlBr obtained by various methods. The first two columns are calculated from the n=1 and n=2 energies and the band masses with no correction to the Coulomb potential. The third column is calculated in the Wannier limit and the fourth and fifth are estimates made using a corrected potential. The band masses are from Reference 27

	TlBr		Wannier	Estimates	
	fcc	sc	Limit sc	fcc	sc
E_g(eV)	3.327	3.0203[a]	3.0198[a]	--	--
R(meV)	24.2	10.3[a]	9.8[a]	60-100[b]	4.9[c]
ε_o	11.8	13.3	16.1	10-15	--
a_o(Å)	25.2	52.8	63.9	12-16	∼ 40
$\mathcal{E}_I$(v/cm)	9.7×10^4	2.0×10^4	1.5×10^4	--	--

[a] Reference 10.

[b] Reference 27.

[c] Reference 50.

the actual band gap energy for sc TlBr since the n=2 state marks the approximate onset of Wannier behavior.

The TlBr fcc exciton binding energy in Table 4 obtained from the n=1 and n=2 energies is also an upper bound with the actual value given by the difference between the n=1 energy and the Wannier limit band gap energy. Again the normal phase TlBr values are illustrative. The sc binding energies are 10.3 and 9.8 in meV when calculated from the band gap obtained with the n=1 and 2, and n=2 and 3 energies, respectively, with the latter value usually considered the actual binding energy.

Since Wannier behavior essentially begins for sc TlBr with the n=2 state, the simultaneous equations generated from Equation (29) with the n=2 and n=3 energies provide a binding energy R' = 6.5 meV which is valid for calculating the binding energy of higher-hydrogenic states with $n \geq 2$, their radii, and the effective static dielectric constant, ε_o^*, for the exciton. In the sc phase case, a value of $\varepsilon_o^* = 16.1$ is calculated from Equation (11) which can be compared with values obtained from the n=1 and n=2 energies, $\varepsilon_o = 13.3$, and from the literature, $\varepsilon_o = 35.1$,[64] where the band masses for the reduced mass were taken from Reference 27. Hence the fcc ε_o value obtained from the n=1 and n=2 energies and band masses also from Reference 27 can be expected to be low with respect to both the exciton effective and actual static dielectric constants.

The Bohr radius in Table 4 for the fcc phase can be expected to be low relative to its Wannier limit from the sc values given. Since the Wannier limit value for the actual n=1 radius is usually considered to be high, the ionization fields in Table 4 calculated with the fcc value may be quite good for field ionization of the n=1 exciton state as defined by Equation 11.

The fcc estimates[27] of Table 4 can be compared with fcc experimental values in view of the trends indicated by sc values since the Wannier limit and the central cell corrected estimates should bring the quantities of both methods to the same place, namely the real crystal properties. On this basis the fcc estimated static dielectric constant and radius appear to be somewhat low and the binding energy high. The table also indicates that the onset of fcc Wannier behavior should be expected after the n=2 exciton state in contrast to the sc case.

Figure 29 provides additional evidence of the larger ionization field for the fcc phase relative to the sc phase due to the greater field sensitivity of the sc n=1 feature which has a smaller absorption peak height but a larger EA negative peak at n=1.

The assignment of the α and β features which do not have a place in the band structures has not been established, although Heidrich _et al_.[27] suggested that they might be due to either the n=2 exciton state or intervalley scattering of n=1 excitons. The n=2 assignment would not be consistent with the n=2 location from the TlBr EA measurement of this study. The electromodulation structure associated with the 1' split peak in the normal phase, if applicable to the abnormal phase, would not support the intervalley scattering origin for α and β since the unusual lineshape associated with α and β is not observed. Two characteristics of α and β have been observed which bring into question the intrinsic nature of these features including their sensitivity to sample preparation and the occurrence of the two nonintrinsic peaks above the n=1 energy in the normal phase when the fcc sample thickness was increased to 700 Å. In view of these facts, more investigation is needed of α and β and an explanation of the unusual EA lineshape may help to clarify the origin of these features.

CHAPTER IX. CONCLUSION

The electromodulation spectra of the normal (sc) phase TlCl and TlBr samples have been reduced to values of electric field induced changes in the dielectric function that are in reasonably good agreement with the calculations of Blossey[11a] considering the experimental problems involved with the measurement and the scope of the calculation which did not include photoconductivity effects. A sample preparation technique was developed which allowed the measurements to be made near liquid helium temperature with a low level of static strain in the sample and with no observed dynamic strain due to the electric field modulation. Photoconductivity effects were controlled to the extent that the electromodulation spectrum could be measured over the exciton and interband region with substantially lower distortion than has been reported in electroreflective measurements[46] where structure is nearly absent for the n=1 exciton state. Electromodulation features were observed which are tentatively assigned to intrinsic exciton state splitting and to an exciton-phonon quasibound state. These features should be studied in more detail with efforts directed at improving reproducibility and resolution.

The results indicate the importance of photocarrier effects in both theory and experiment in the electromodulation of exciton states. In the future, calculations should include the effect of photocarriers on the field seen by the exciton and experimentally samples should be developed with known and reproducible photocarrier properties with temperature control between liquid helium and nitrogen temperatures and bipolar modulation fields.

The abnormal (fcc) phase EA measurements have demonstrated the usefulness of the modulation method in resolving exciton states by determining the n=2 energy in TlBr. This has enabled a number of quantities to be calculated from the Wannier exciton model. The resolution of the n=2 energy in TlCl is probably also possible with an EA measurement and patience with the signal to noise problem. The α and β features are still unassigned but the unusual EA lineshape and sample preparation sensitivity found in this investigation may prove useful in making definitive assignments in conjunction with future work.

APPENDIX: ELECTROMODULATION MEASUREMENT

The electromodulation method used in this investigation involves modulating the light transmission through the sample by applying a square wave electric field to the sample perpendicular to the light path. The AC field is used rather than a DC field to avoid problems inherent in low level DC measurements such as time stability.

The square wave electric field causes the transmitted light intensity to have an AC component which depends on the incident photon energy. If the photon energy corresponds to the maxima of an absorption peak, which is broadened, shifted and possibly split by the field, the transmission will be enhanced at this energy and will have an AC component which is in phase with the applied field. A photomultiplier converts the modulated light intensity into a voltage signal, across a resistor to ground, which is amplified by a phase sensitive (lock-in) amplifier. Since the signal is in phase with the applied field, which provides a frequency and phase reference to the lock-in, the lock-in output is positive indicating that the field has caused an increase in the transmission of the sample. A field-induced decrease in the transmission occurs when the incident photon energy corresponds to a location in a spectrum where the absorption is increased by the field, as occurs in the wing of the absorption peak discussed above. The decreased transmission when the field is on causes an AC signal component which is out of phase 180° with the applied field, resulting in a negative amplifier output which corresponds with the reduced transmission. The broadening of bound exciton state absorption peaks is due to a reduction in the lifetime of the state by the electric field and the shifting and splitting of peaks is due to mixing of states by the field perturbation.[11a,b]

Above the band gap, where the continuum states exist, rounded oscillatory structure is seen in electromodulation spectra as is shown in Figure 2. This structure does not have a simple physical explanation similar to the bound state case but each peak has been recognized from the calculation as due to a term in a series which is summed.[11a,b]

REFERENCES

1. J. Frenkel, Phys. Rev. 37, 17 (1931); 37, 1276 (1931).

2. G. H. Wannier, Phys. Rev. 52, 191 (1937).

3. R. J. Elliott, Phys. Rev. 106, 1384 (1957).

4. R. S. Knox, Theory of Excitons (Academic Press, New York, 1963).

5. D. Dexter and R. S. Knox, Excitons (Wiley, New York, 1965).

6. M. Cardona, Modulation Spectroscopy (Academic Press, New York, 1969).

7. R. K. Willardson and A. C. Beer, editors, Semiconductors and Semimetals (Academic Press, New York, 1972), Vol. 9.

8. H. Overhof and J. Treusch, Solid State Commun. 9, 53 (1971).

9. M. Inoue and M. Okazaki, J. Phys. Soc. Japan 31, 1315 (1971).

10. S. Kurita and K. Kobayashi, J. Phys. Soc. Japan 30, 1645 (1971).

11a. D. F. Blossey, Ph.D. Thesis, Univ. of Illinois, 1969; Phys. Rev. B2, 3976 (1970); Phys. Rev. B3, 1382 (1971).

11b. D. F. Blossey and P. Handler, in Semiconductors and Semimetals, edited by R. K. Willardson and A. C. Beer (Academic Press, New York, 1970), Vol. 9.

12. H. Haken, Z. Phys. 146, 527 (1956).

13. J. Callaway, Energy Band Theory (Academic Press, New York, 1964).

14. W. Franz, Z. Naturforsch. 13, 484 (1958).

15. L. V. Keldysh, Zh. Eksperim. i Teor. Fiz. 34, 1138 (1958); [Soviet Phys. JETP 7, 788 (1958)].

16. K. Tharmalingam, Phys. Rev. 130, 2204 (1963).

17. J. Callaway, Phys. Rev. 130; 549 (1963); 134 A998 (1964).

18. J. O. Dimmock, in Semiconductors and Semimetals, edited by R. K. Willardson and A. C. Beer (Academic Press, New York, 1966), Vol. 3.

19. G. Dresselhaus, Phy. Chem. Solids 1, 14 (1956).

20. R. J. Elliott, Phys. Rev. 108, 1384 (1957).

21. L. Van Hove, Phys. Rev. 89, 1189 (1953).

22. J. C. Phillips, Phys. Rev. 104, 1263 (1956).

23. R. Kronig, J. Opt. Soc. Am. 12, 547 (1926).

24. L. G. Schultz, Acta Crystallogr. 4, 487 (1951).

25. T. Ichikawa, Phys. Stat. Sol. (b) 65, 411 (1974).

26. K. Heidrich and B. Kramer, Phys. Stat. Sol. (b) 72, 547 (1975.).

27. K. Heidrich, W. Staude, and J. Treusch, Phys. Rev. Lett. 33, 1220 (1974).

28. J. Overton and J. P. Hernandez, Phys. Rev. B7, 778 (1973).

29. J. P. Van Dyke and G. A. Samara, Phys. Rev. B11, 4935 (1975).

30. J. Treusch, Phys. Rev. Lett. 34, 1343 (1975).

31. S. Tutihasi, Phys. Chem. of Solids 12, 344 (1959).

32. H. Zinngrebe, Z. Phys. 154, 495 (1959).

33. R. Z. Bachrach and F. C. Brown, Phys. Rev. Lett. 21, 684 (1968); Bull. Am. Phys. Soc. 14, 558 (1969); Phys. Rev. B1, 818 (1970).

34. S. Kurita and K. Kobayashi, J. Phys. Soc. Japan 26, 1557 (1969); 28, 1096 (1970); 28, 1097 (1970).

35. D. C. Hinson and J. R. Stevenson, Phys. Rev. 159, 711 (1967).

36. A. Feldman, Bull. Amer. Phys. Soc. 14, 428 (1969).

37. E. Mohler, G. Schögl, and J. Treusch, Phys. Rev. Lett. 27, 424 (1971).

38. Ch. Uihlein and J. Treusch, Solid State Commun. 17, 685 (1975).

39. S. Kurita, K. Kobayashi and Y. Onodera, Prog. Theor. Phys. Suppl. No. 57, 10 (1975).

40. S. Kondo, K. Nakamura, M. Fujita and Y. Nakai, J. Phys. Soc. Japan 37, 573 (1974); 38, 1400 (1975).

41. S. Kurita, K. Kobayashi, and M. Matsushita, J. Phys. Soc. Japan 33, 270 (1972).

42. Y. Toyozawa and J. Hermanson, Phys. Rev. Lett. 21, 1637 (1968).

43. J. C. Hermanson, Phys. Rev. B2, 5043 (1970).

44. Y. Toyozawa, in Proceedings of the 3rd International Conference on Photoconductivity, edited by E. M. Pell (Pergamon, New York, 1971).

45. J. Bordas and E. A. Davis, Surface Science 37, 828 (1973).

46. R. Shimizu and T. Koda, J. Phys. Soc. Japan 38, 1550 (1975).

47. In absorption spectra this effect is observed as a quenching of higher energy exciton state absorption strengths as these states are shifted by a magnetic field through the energy equal to a lower state energy plus the energy of an LO phonon.

48. H. Tamura, T. Masumi and K. Kobayashi, J. Phys. Soc. Japan 23, 1173 (1967).

49. K. Hattori, J. Phys. Soc. Japan 38, 351 (1975).

50. J. Pollmann, Phys. Status Solidi (b) 63, 548 (1974).

51. J. Pollmann and H. Buttner, Solid State Commun. 17, 1171 (1975).

52. K. K. Bajaj, Solid State Commun. 15, 1221 (1974).

53. J. Heinricks and N. Kumar, Solid State Commun. 16, 1035 (1975).

54. K. K. Bajaj and C. A. Aldrich, Solid State Commun. 18, 641 (1976).

55. J. W. Hodby, J. A. Borders, F. C. Brown and S. Foner, Phys. Rev. Lett. 19, 952 (1967).

56. H. Tamura, T. Masumi and K. Kobayashi, in Proceedings of the 3rd International Conference on Photoconductivity, edited by E. M. Pell (Pergamon Press, New York, 1971).

57. J. W. Hodby, G. T. Jenkin, K. Kobayashi and H. Tamura, Solid State Commun. 10, 1017 (1972).

58. D. Fröhlich, B. Staginnus and S. Thurm, Phys. Status Solidi 40, 287 (1970).

59. Y. Onodera, Optics Commun. 3, 113 (1971).

60. D. Fröhlich, J. Treusch and W. Kottler, Phys. Rev. Lett. 29, 1603 (1972).

61. A. D. Brothers and D. W. Lynch, Phys. Rev. 180, 911 (1969).

62. A. J. Grant, W. Y. Liang and A. D. Yoffe, Phil. Mag. 22, 1129 (1970).

63. A. D. Redmond and B. Yates, J. Phys. 5, 1589 (1972).

64. R. P. Lowndes, Phys. Lett. 21, 15 (1966).

65. K. Hojendähl, Kgl. Danske Videnskab. Selskab. Mat.-Fys. Medd. 16, No. 2 (1938).

66. E. R. Cowley and A. Okazaki, Proc. Roy. Soc. (London) A300, 45 (1967).

67. R. Shimizu, T. Murakashi and T. Kōda, J. Phys. Soc. Japan 33, 866 1972).

68. R. Shimizu, T. Kōda and T. Murahashi, J. Phys. Soc. Japan 36, 161 (1974).

69. R. Shimizu and T. Kōda, J. Phys. Soc. Japan 37, 1468 (1974).

70. J. Nakarhara and K. Kobayashi, J. Phys. Soc. Japan 40, 180 (1976); 40, 189 (1976).

71a. J. Nakahara, K. Kobayashi and M. Seki, Solid State Commun. 18, 245 (1976).

71b. J. Nakahara, K. Kobayashi and A. Fujii, J. Phys. Soc. Japan 37, 1312 (1974); 37, 1319 (1974).

72. T. Kawai, K. Kobayashi and H. Fujita, J. Phys. Soc. Japan 21, 453 (1966).

73. Y. Makita, K. Kobayashi and M. Kanada, J. Phys. Soc. Japan 25, 816 (1968).

74. Y. Makita and K. Kobayashi, J. Phys. Soc. Japan 32, 1262 (1972); 38 435 (1975).

75. R. Shimizu and T. Koda, to be published in *Proceedings of the 1975 International Conference on Luminescence* at Tokyo, 1975.

76. S. Kurihara, K. Fueki and Takashi Muraibo, J. of Solid State Chem. 8, 229 (1973).

77. A. C. Bailey and B. Yates, Phil. Mag. 16, 1241 (1967).

78. Dr. C. H. Culp provided much appreciated assistance in designing the high voltage square wave generator.